PNC TN9600 97-002



# 海外出張報告書

# 第18回線形加速器国際会議(LINAC96)出張報告

１９９７年１月

動力炉・核燃料開発事業団
大洗工学センター

Ⓢ

公　開　資　料
PNC TN9600 97-002
1 9 9 7 年 1 月

# 海外出張報告書
# 第18回線形加速器国際会議 (LINAC96) 出張報告

武井 早憲*

## 要 旨

第18回線形加速器国際会議 The Eighteenth International Linac Conference (LINAC96) が1996年8月スイス・ジュネーブで開催され、ポスター発表を行った。本報告書は、LINAC96の概要とその後訪問したパウル・シェラー研究所 (Paul Scherrer Institute, PSI) における液体金属ターゲットに関する検討をまとめた。

LINAC96では、大電流線形加速器の主要要素である加速管及びビームダンプに関する設計資料の発表を行い、質問者との討論から電子軌道の解析方法などに関して新たな知見が得られた。

また、PSIで液体金属ターゲットに関する技術討論では、液体金属ターゲットを用いたシステムは、固体ターゲットより熱応力の点で設計が容易になるため、ターゲットを含む全体のシステム設計が重要になることがわかった。この討論から、消滅処理技術の確立に不可欠なターゲット系の開発に関して指針が得られた。

*基盤技術開発部 先進技術開発室

# 目　次

# 図リスト

# 第1章

# 第18回線形加速器国際会議参加報告

## 1.1 会議名称

The Eighteenth International Linac Conference (LINAC96)

## 1.2 開催日時

1996年8月26～30日

## 1.3 開催場所

Penta Hotel, Geneva, Switzerland

## 1.4 主催

European Organization for Nulear Research (CERN)

## 1.5 LINAC96の概要

本会議は2年毎に開催される線形加速器に関する唯一の国際会議である。参加者は、欧州はもとより米国、日本など16ヶ国から線形加速器の開発に関する幅広い分野の専門家が320名程度参加した。主な国別の参加者数は、アメリカ92名、ドイツ55名、日本38名、ロシア33名、スイス31名であった。

会議では36件の口頭発表及び約250件のポスター発表があり、大強度陽子加速器、イオン加速器及び衝突型電子・陽電子線形加速器などに関する開発状況や理論についての発表が行われた。会議のプログラムを付録-1に示す。

LINAC96の特徴として、陽子加速器などに用いられる超電導電磁石や超電導加速空洞に関する報告が多かったこと、長さが数キロメーターに及ぶ衝突型(高輝度)電子・陽電子線

形加速器の設計に関する報告があったこと、及びレプトンの一種類であるミューオンを用いた衝突型線形加速器についての発表があったことなどが挙げられる。特に、長さ数キロメーターの線形加速器では超精密なアライメントが要求されるため、加速器が設置される地盤の振動スペクトル($10^{-3}$Hz～100Hz程度)を観測しなければならないと講演があった。また、大電力線形加速器の利用に関する講演は付録-2に示したM. Promé氏(CEA/DSM)の口頭発表しかなかった。その中で、加速器の利用について中性子源、核融合材料研究、トリチウム生成計画を報告していたが、核変換技術に関しては概要程度しか報告されなかった。

尚、第19回線形加速器国際会議は、平成10年8月24～28日の予定でアメリカ・アルゴンヌで開催される予定である。

## 1.6 参加報告

本会議で事業団における大電流電子線形加速器の主要要素である加速管及びビームダンプの開発成果についてポスター発表を行った。特に、大電流を加速する加速管の性能評価手法に関しては、今後開発される衝突型電子・陽電子線形加速器の設計に大変参考になるため、専門家から詳細な点について多くの質問を受けた。またビームダンプに関しては、世界的に大強度化を目指す加速器にとって必要不可欠な要素として幅広い専門家から注目を集め、設計手法の正当性について高い評価が得られた。さらに現在性能試験を行っている事業団の加速器の最新情報について質問を受けたが、外部発表許可の範囲で回答した。以下、具体的に報告する。

(1) Analysis of Wake Fields on TWRR Accelerator Structure in PNC

本発表は、新しく事業団で開発された加速管を用いて、電子ビームを加速するときに発生する摂動電磁場(Wake Field)を評価したものである。発生する摂動電磁場は、電子ビームを不安定にする要因の一つである。評価においては、摂動電磁場の基本的な振る舞いから検討を行い、計算コードMAFIA及びABCIを用いて安定に加速を行うことが出来る最大電流値を求めている。数値解析の結果、事業団の加速管は最大5Aまで電子ビームを安定に加速することがわかった。(付録-3参照)

この解析方法は今後開発される衝突型電子・陽電子線形加速器の設計に応用できるため、解析方法の基本的な考え方から計算コードABCIの詳細な使用方法に関して多くの質問を受けた。

(2) Conceptual Design of Beam Dump for High Power Electron Beam

本発表は、大電流電子線を安全に吸収するビームダンプに関して、事業団とPSIと共同で開発された中空状金属円板を多数用いるRing & Disk方式の利点に関するものである。(付録-4参照)

現在加速器は、陽子及び電子に限らず世界的にビーム電力が数千キロワット級の大強度化を目指す傾向にある。しかし、大強度化を目指す加速器の開発は段階的に行う必要があり、まず設計電力の1～10%程度、すなわち数百キロワットのビーム電

力で試験を行っている。このため、簡単な構造で数百キロワットのビームを吸収するビームダンプが必要となる。

このような背景から、事業団で開発されたビームダンプは大強度化を目指す加速器にとって必要不可欠な要素機器として幅広い専門家から注目を集めた。特に、次項で説明するAPT計画で設計されている加速器試験用ビームダンプの構造が事業団のものとほぼ同じであったため、LANLのSchneider氏らから製作上の問題点などについて質問があった。また、発表に対する聴衆者の関心は高く、詳細な論文発表を期待する声が聞かれた。この発表と質疑応答により、ビームダンプの設計手法の正当性について十分な評価が得られた。

さらに、質問者との質疑応答の中で性能試験を行っている事業団の加速器について多くの質問を受けた。質問内容としては、電子銃及びRF系の要素設備や性能試験の結果であった。しかし、平成8年8月22日現在の最新試験結果については外部発表許可を受けていないため発表を控え、許可を受けている平成8年3月末の結果について口頭で回答した。平成8年9月上旬に終了した性能試験の結果について早急に論文発表する必要性を感じた。

## 1.7 聴講

聴講したなかで興味を引いた発表を下記に示す。

(1) ATP Accelerator Technology, *J.David Schneider (LANL)*

LANLではエネルギー1.3GeV、電流100mAのCW陽子加速器を用いてトリチウムを1年間に2～3kg生成するAPT計画(Accelerator Production of Tritium)を進めている。CWで100mAの陽子加速器は加速系やRF系の開発課題も多く、発表の中では主に要素開発に重点が置かれていた。その中で発表者は、トリチウムは1年間で5.5%の割合で$^3He$に崩壊していくのでトリチウムの生成効率をあげるようなターゲット系の開発を行わなければならないと説明していた。APTでは陽子を鉛標的に照射し、発生した中性子を$Li-A\ell$のロッドに照射させ、$^6Li(n,\alpha)T$反応によってトリチウムを生成させる予定である。

この生成過程においてメンテナンスや故障などで加速器が運転出来ないことを考えると、2台の加速器と複数のターゲット系を効率良く組み合わせるような体系にする必要があると説明していた。この考え方は日本・アメリカ・ヨーロッパ・ロシアで進めている核融合材料開発のための中性子照射施設(IFMIF)におけるターゲット系の考え方と同様である。このように加速器の運転体系まで考えに入れてトリチウムの生成効率を最大にしようという試みは、今後事業団で行う消滅処理用ターゲットの開発に参考になると思われる。

(2) Design of the NLC Positron Source, *H.Tang (SLAC)*

次世代の衝突型線形加速器では、毎秒$10^{10}$個以上の陽電子を必要とするため、陽電子生成効率を減少させないように陽電子生成標的の発熱を効率良く除去することが

重要になる。本発表では従来考えられていた標的構造、すなわち円筒形標的を外側から冷却する構造と異なり、外径25cm(内径23.6cm)のリング状の標的(材質$W_{75}Re_{25}$)を内側から冷却する構造を採用している。この構造を採用することにより、従来の構造では困難であった熱応力の緩和を容易に解決した点である。さらにリング標的を毎秒2回転で回転させ、除熱効率を向上させている。尚、回転軸のシール部分からのリークによる真空度の悪化を防ぐため、差動排気系を採用している。(付録-5参照)

本発表は事業団が開発したビームダンプで問題になった熱応力の緩和する方法に関して参考になり、今後開発するターゲット系の設計にも有効と思われる。

(3) Temperature stabilisation of the accelerating stracture, *Frank-R. Ullrich (DESY)*

大電流の荷電粒子ビームを加速することは、荷電粒子ビームの安定性が重要になる。このため、ミクロ的に考えればビーム不安定性を解決しなければならないが、加速系全体で考えた場合には加速管の温度を一定に保つことも重要な要因となる。

本発表は長さ数キロメートルにおよぶ線形電子加速器の加速管の温度を摂氏40度に保つ冷却設備のテストシステムについて報告したものである。テストシステムはクライストロンによって摂氏70度に暖められた温水と摂氏30度の冷水を混合させて加速管数本を冷却する構造になっている。加速管の温度は温水と冷水を混合させる三方弁の開閉により制御され、その開閉度はRF窓の出入口温度差でフィードバック制御をしている。この制御によりビーム繰り返しを変化させたときの温度変化は最大0.75度であった。(付録-6参照)

この結果から、直ちに長さ数キロメートルの加速系の温度制御が可能であると結論付けられないため、発表者のUllrich氏に確認したところ、摂氏70度前後に暖められた空気を系全体に配管で流し、温水と熱交換を行うことを考えていると回答があった。本発表は加速器の冷却設備としての構造を論文としてまとめている点で十分評価できる。尚、事業団が開発している冷却設備の温度制御は、この論文と同程度であるが、制御方法が異なるため、加速器制御技術の発展に寄与できるものと思われる。

(4) First experimental results of the BNL inverse free electron laser accelerator, *A. van Steenbergen (BNL)*

FEL(自由電子レーザー)は交互に向きの変わる磁場(ウイグラー)の中に電子ビームを入射させることによりレーザー光を発振させる。本発表は、FELと異なるInverse FEL(IFEL)に関する初めての実験結果を報告したものである。(付録-7参照)

IFELは電子ビームとレーザー光をウイグラーの中に通過させ、電子ビームを加速させる方法であり、1970年代から1980年代にかけて理論研究が行われた。IFELは高周波を用いる従来の加速方法と異なり低エネルギーの電子ビームを高加速勾配で加速することが可能である。BNLでは40MeVの電子ビームを1GWの炭酸ガスレーザーと最高磁場10kGのウイグラーを用いて42MeVまで加速を行い、加速勾配は4.9MV/mであった。発表の中で現在開発している1TW級の炭酸ガスレーザーを用いれば加速勾配100MV/mの加速も可能であると予想していた。本発表は高周波

を用いた加速に捕われない新しい加速方法として多くの専門家の注目を集めていた。

## 1.8 研究用線形加速器の概要

LINAC96を開催するにあたり、世界各地の研究施設に設置された線形加速器の技術的な諸元をL.Rinolfi 氏(CERN)ら11名がまとめた。平成8年8月現在、研究用線形加速器は、地域毎にアメリカ61台、アジア37台、ヨーロッパ78台、合計176台設置されている。また、176台の加速器を加速粒子の種類毎に分類すると、電子加速器111台、陽電子加速器12台、陽子加速器23台、イオン30台となる。付録-8に176台の線形加速器の概要を表わす。事業団の加速器も研究用加速器として概要の中にまとめられている。尚、詳細なリストはWorld-Wide Webによって出版されているので参考にされたい。

(address : http://www.cern.ch/Linac96/Linacs.html)

## 1.9 CERN見学

LINAC96のオプショナルツアーとしてCERNを見学した。CERNは、Geneva市の西、フランスとスイスの国境に位置する研究所であり、1954年に創設された。この研究所は、衝突型電子・陽電子加速器を始めとし、陽子加速器・イオン加速器を有し、多くの素粒子実験が行われている。多くの素粒子実験は共同利用実験として行われ、その利用者数は80ヶ国以上にわたる約6000名(500を越える大学、研究所)である。

見学コースは、重心系エネルギー161GeV、直径26.6kmのリングを有する衝突型円形加速器(LEP2)の測定器の一つであるOPAL、LEP2に電子・陽電子を供給する入射部、陽子加速器の入射部であった。特に、世界で初めて11個の反水素原子*を生成した低エネルギー反陽子リング(LEAR)を見学したことは、速報性があり大変有意義であった。(図1-1参照) また、OPALの見学では、平成8年7月から8月に実施した重心系エネルギー161GeVでの電子・陽電子衝突実験の結果が見学者用の掲示板に張り出され、ゲージ粒子の一つであるWボソンの生成断面積が出ていた。わずか1、2週間前の実験結果が公表されていることに驚かされた。

尚、今回の実験を開始する前にリングにビームが回らないという事件があったが、調査の結果、ビールの空き瓶2本がビームパイプの中にあることが発見された。当局は何者かの悪戯と判断しているが、このような失敗談を見学者に紹介すること自身日本と異なる印象を持った。

*G. Baur *et al.*, Phys. Lett. **B368** (1996) 251.

# 第2章

# PSIにおける技術討論

## 2.1 訪問日時

1996年9月2日及び3日

## 2.2 訪問場所

Villigen, Switzerland

## 2.3 研究所の概要

PSIは、ドイツ国境から南に約20km、チューリッヒ空港から急行列車で約90分の場所に位置し、約1200人のスタッフと年間約160億円の予算規模の国立研究所として、加速器による原子核研究や原子炉の開発などを行っている。(付録-9参照)

研究所が創立された1980年頃は加速器を用いた原子核や素粒子研究が中心であったが、最近では加速器から得られる中性子、ミューオン、イオン及びレーザー光などを用いて材料研究を行うと伴に原子炉の安全性についての研究も行っている。

特に中性子を用いた材料研究を行うために平成9年1月陽子加速器(600MeV、1.5mA、0.9MW)から得られる陽子ビームを液体金属ターゲットに照射し、中性子を発生させる計画がある。これは大電力陽子線を世界で初めて液体金属ターゲットに照射する実験でもある。

## 2.4 固体ターゲットに関する技術討論

LINAC96で発表した中空状金属円板を多数用いるRing & Disk方式のビームダンプを中心にPSIで製作された種々の固体ターゲットについて製作担当者(G.Heidenreich氏)と技術討論を行った。事業団が製作したRing & Disk方式のビームダンプはPSIのビームダンプを参考としているため、担当者には電気的絶縁機構など事業団で改良した点を主に説明

した。その結果、事業団で改良したことにより、電子ビームによる熱の伝導経路を把握するのに優れた性能を持つビームダンプになったことを評価された。

また、LINAC96という国際会議に設計データの一部を論文として発表している点も十分評価できると賞賛された。これは、PSIのRing & Disk方式ビームダンプがその設計データを初めとしてまだ論文発表をしていないためと考えられる。LINAC96で発表した設計データと合わせて、さらに詳しい熱応力の解析結果やビームダンプの構造などを加えて早急に論文としてまとめるべきであるとG.Heidenreich氏から激励された。論文の内容(見出し)をY.Takeda氏、G.Heidenreich氏らと討論を行ったので、付録-10に示す。

尚、PSIのRing & Disk方式ビームダンプの設計データを頂いてきたので付録-11に示す。この資料は、楕円状中空円板の弾塑性変形を解析した結果を表わす4分の1モデルである。この結果は、熱歪みが0.2%、許容繰り返し数が$10^4$回以上であることを示している。

## 2.5 液体金属ターゲットに関する技術討論

液体金属ターゲットの設計グループのリーダーG.S.Bauer氏から液体金属ターゲットの全般的な説明を受けた後、技術討論を行った。(付録-12参照) その結果、液体金属ターゲットはビームと液体金属が接する部分の取り扱いに注意すれば、固体ターゲットと比較して熱応力の点などで比較的設計が容易であることがわかった。特に、ビームが液体金属に入射する方法は、液体金属ターゲット計画の全体を決定する重要な要因と言っても過言ではない。

具体的な例として、中性子を用いた材料研究を行うためにPSIに設置された鉛-ビスマスの液体金属ターゲット(SINQ)に関して調査した。(付録-13参照) SINQでは、陽子ビームを鉛直上向きに入射させているため、液体金属と真空を隔てるビーム窓がある。このビーム窓はヘリウムと水を用いて冷却しているため、図2-1に示した巨大な純水精製装置が必要になり、SINQ計画の中で重要な付帯設備であることがわかった。また、液体金属内の熱伝導は自然対流を利用した一次元の流れで十分説明できるため、液体金属自身から熱を奪うことは比較的容易であることもわかった。(付録-14及び図2-2参照)

このため、液体金属にビームを照射する方法や加速系を含めた全体の安全性などを考慮したコンセプト作りに重点を置いた研究が必要であるとG.S.Bauer氏から指摘された。特に事業団の量子工学試験施設増設計画では、模擬的に核変換が行えるような核種でビーム照射実験を行い、理論的に予想された変換効率と比較を行うことを考えてコンセプトを作るべきであると激励された。この方法により将来の消滅処理システムの設計に役立つ情報が得られると伴に消滅処理の分野に多大な貢献が期待出来るとコメントを頂いた。

# 第3章

# まとめ

LINAC96での発表は、大電流線形加速器の主要要素である加速管及びビームダンプに関する設計資料の公表であり、質問者との討論から新たな知見や問題点を得られ大変有益であった。討論の中で、現在性能試験を行っている事業団の加速器に関して、最新の試験結果を聞いてくる研究者がかなり多く、国際的にも注目をされていることが実感できた。この試験結果は、日本国内だけに留まらず、海外も視野に入れた論文として早急にまとめ、発表する必要性があると感じた。

また、会議を聴講して、現在の加速器開発は長さ数キロメーターの衝突型電子・陽電子線形加速器に代表される高エネルギー・高輝度化へ向かう開発と材料照射試験などに用いられる大電力化へ向かう開発に大きく分けられるが、共通して高効率な加速器を目指しているという印象を受けた。さらに、次世代の加速器としてレプトンの一種類であるミューオンを用いた衝突型線形加速器の概念設計が行われており、加速器開発のフロンティアを感じることができた。

PSIでのターゲットに関する技術討論では、ビーム照射体である液体金属ターゲットの取り扱いを検討することより、液体金属にビームを照射する方法や加速系を含めた全体の安全性などを考慮したコンセプト作りに重点を置くようにと意見を頂いた。このような考え方は、将来の消滅処理システムを考えるうえで重要なマイルストーンになると思われる。技術討論を通して「液体ターゲットを自分達で作ろう」という気迫が感じられ、第一線で活躍している研究者に接することができた。今後、このような研究者達との密接な意見交換をすることが重要であると思う。

(a) 電子銃外観

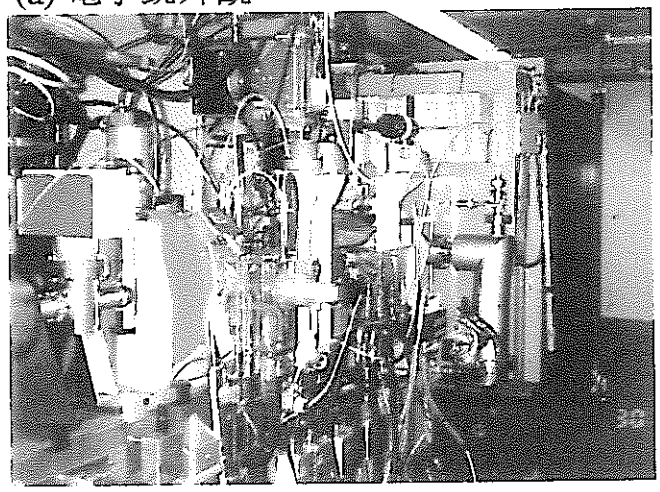

(b) 陽電子源外観

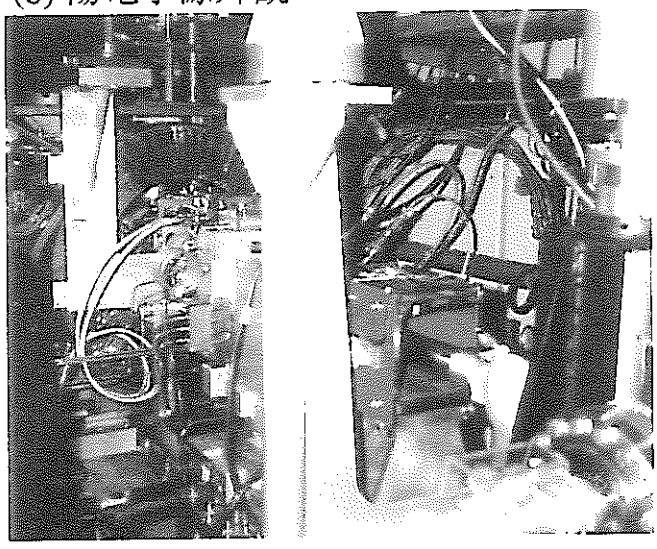

(c) LEAR

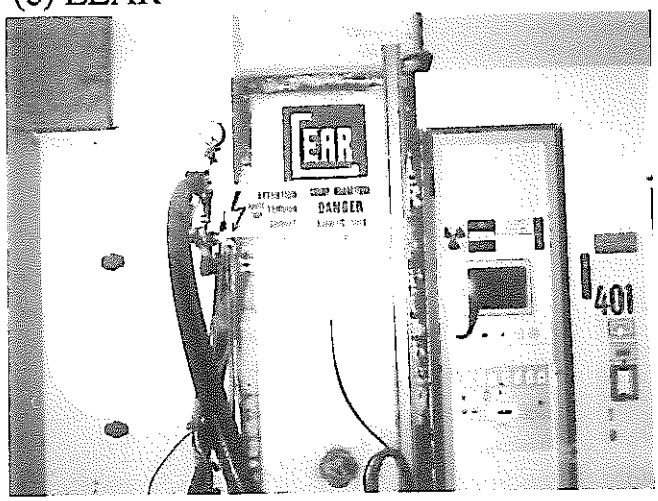


図1-1 CERNでの見学

(a) ターゲット外観

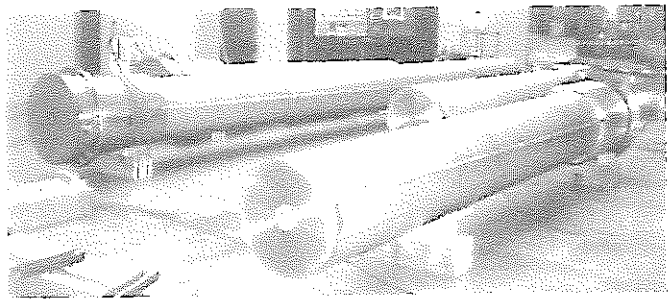

(b) 純水精製装置

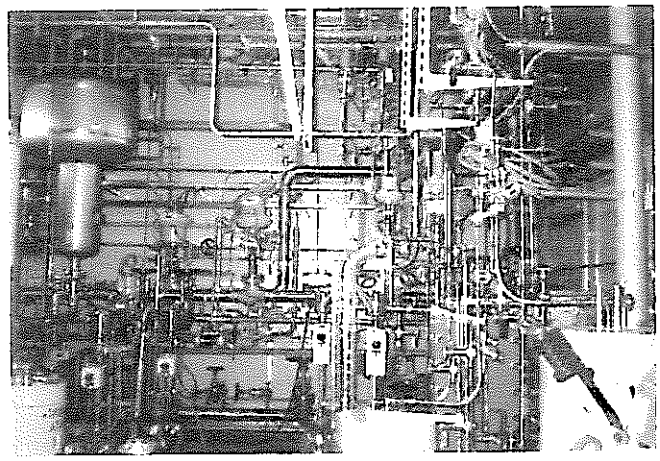

(c) ビームライン (ターゲット側)

(d) ビームライン (加速器側)

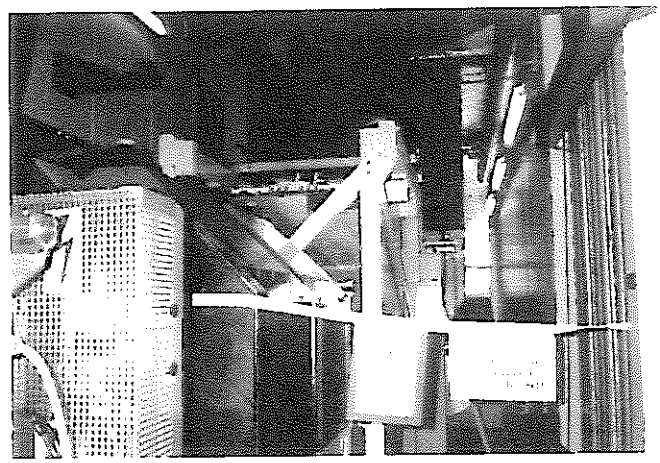

図2-1 SINQターゲット(PSI)

(a) SSE外観

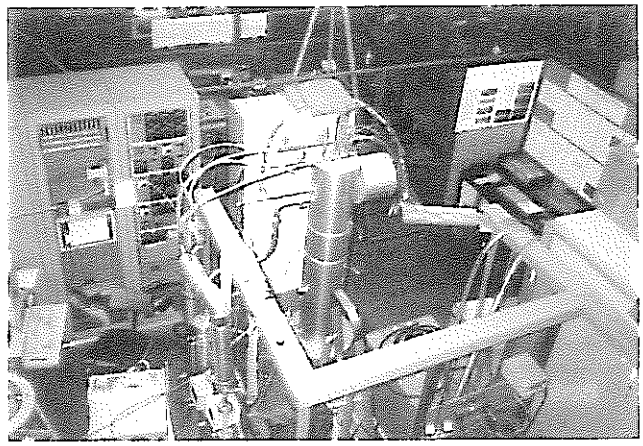

(b) Pb-Bi 保管容器

図2-2 Small-Scale Experiment (SSE) の実験装置

付録-1

LINAC96 Session Time Table

# LINAC96 SESSION TIME TABLE

| Monday 26th August | | Tuesday 27th August | | Wednesday 28th August | | Thursday 29th August | | Friday 30th August | |
|---|---|---|---|---|---|---|---|---|---|
| 8:30 | Welcome and announcements | 8:30 | TU101<br>G.A. LOEW (SLAC)<br>Review of Linear Colliders | 8:30 | WE101<br>H. HAYANO (KEK)<br>ATF Linac Commissioning | 8:30 | TH101<br>J. BILLEN (LANL)<br>Smooth Transverse and Longitudinal Focusing in High-Intensity Ion Linacs | 8:30 | FR101<br>R.B. PALMER (BNL)<br>The Design of High Luminosity μ⁺μ⁻ Colliders |
| 9:00 | MO101<br>W.K.H. PANOFSKY (SLAC)<br>The Creation of SLAC Leading to 30 Years of Operation | 9:00 | TU102<br>T.O. RAUBENHEIMER (SLAC)<br>SLC Status and NLC Design and R&D | 9:00 | WE102<br>I. WILSON (CERN)<br>CLIC Test Beam Facilities Status and Results | 9:00 | TH102<br>Y. YAMAZAKI (KEK)<br>Design Issues for High Intensity, High-Energy Proton Accelerators | 9:00 | FR102<br>P.B. WILSON (SLAC)<br>Advanced RF Power Sources for Linacs |
| 9:30 | MO102<br>M. PROME (CEA)<br>Major Projects for the Use of High Power Linacs | 9:30 | TU103<br>J. ROSSBACH (DESY)<br>New Linac Based FEL Projects using Bright Electron Beams | 9:30 | WE103<br>R. WANZENBERG (DESY)<br>Review of Beam Dynamics and Instabilities in Linear Colliders | 9:30 | TH103<br>S. YU (LBNL)<br>Review of New Developments in the Field of Induction Linacs (Electrons and Ions) | 9:30 | FR103<br>S. CHATTOPADHYAY (LBNL)<br>Role of Lasers in Linear Accelerators |
| 10:00 | Coffee/tea break | 10:00 | Coffee/tea break | 10:00 | Coffee/tea break | 10:00 | Coffee/tea break | 10:00 | Coffee/tea break |
| 10:30 | MO201<br>B. DUNHAM (CEBAF)<br>CEBAF, A Status Report | 10:30 | TU201<br>H. HASEROTH (CERN)<br>Lead Ion Injector at CERN | 10:30 | WE201<br>M. DOHLUS (DESY)<br>Accelerating Structures for Multibunches | 10:30 | TH201<br>U. AMALDI (Univ. Milan)<br>TERA Programme : Medical Applications of Protons and Ions | 10:30 | FR201<br>G. FORTUNA (INFN)<br>Status of ALPI and Related Developments of Superconducting Structures |
| 11:00 | MO202<br>D.J. SCHNEIDER (LANL)<br>APT Accelerator Technology | 10:50 | TU202<br>U. RATZINGER (GSI)<br>The New GSI Injector Linac for High Current Heavy Ion Beams | 11:00 | WE202<br>H. KUGLER (CERN)<br>Laser Ion Source Development for Heavy Ions | 10:50 | TH202<br>A. WAMBERSIE (UCL)<br>Medical Applications of Electron Linacs | 11:00 | FR202<br>G. GESCHONKE (CERN)<br>Superconducting Structures for High Intensity Linac Applications |
| 11:30 | MO203<br>M. PABST (KFA)<br>Halo Simulation in a Realistic Proton Linac Design | 11:10 | TU203<br>A. UENO (KEK)<br>Beam Test of the Preinjector and the 3 MeV H⁻ RFQ with a New Field Stabilizer PISL | 11:20 | WE203<br>S. ARAI (INS)<br>Beam Test Results of the INS RFQ/IH Linac | 11:10 | TH203<br>M.E. THUOT (LANL)<br>The Success and Future of EPICS | 11:30 | FR203<br>C.H. LLEWELLYN SMITH (CERN)<br>Physics at LHC |
| 12:00 | MO204<br>J.A. NOLEN (ANL)<br>Overview of Linac Applications at Future Radioactive Beam Facilities | 11:30 | TU204<br>J. CLENDENIN (SLAC)<br>RF Photoinjectors | 11:40 | WE204<br>D.K.C. CHAN (LANL)<br>Conceptual Design of a Superconducting High Intensity Proton Linac | 11:30 | TH204<br>C. HOVATER (CEBAF)<br>Operational Experience with the CEBAF Control System | 12:00 | Closing remarks |
| 12:30 | Lunch | 11:50 | TU205<br>D.X. WANG (CEBAF)<br>Measurement of Short Bunches | 12:00 | Excursion to Gruyère | 11:50 | TH205<br>A. SERY (CEA and BINP)<br>Ground Motion Studies with Respect to Linac Performance | 12:30 | CERN Lunch and Visit (12:30-18:00) |
| 14:00 | MO301<br>W. GAI (ANL)<br>Performance of the Argonne Wakefield Accelerator (AWA) Facility and Initial Experimental Results | 12:10 | TU206<br>M. ROSS (SLAC)<br>High Performance Spot Size Monitors | | | 12:10 | TH206<br>H. MATSUMOTO (KEK)<br>Dark Currents | | |
| 14:20 | Oral Poster Presentations<br>(10 of 5 minutes each) MOP01.....<br>Poster session 14:20-18:00<br>Coffee/tea break 15:30-16:00 | 12:30 | Lunch | | | 12:30 | Lunch | | |
| | | 14:00 | TU301<br>M.M. WHITE (ANL)<br>Construction, Commissioning and Operational Experience of the Advanced Photon Source (APS) Linear Accelerator | | | 14:00 | TH301<br>A. ENOMOTO (KEK)<br>Upgrade to the 8 GeV Electron Linac for KEKB | | |
| | | 14:20 | Oral Poster Presentations<br>(10 of 5 minutes each) TUP01.....<br>Poster session 14:20-18:00<br>Coffee/tea break 15:30-16:00 | | | 14:20 | Oral Poster Presentations<br>(10 of 5 minutes each) THP01.....<br>Poster session 14:20-18:00<br>Coffee/tea break 15:30-16:00 | | |
| | | | | | | 18:30 | Mövenpick Hotel<br>E. KNAPP (Santa Fe)<br>New Directions for Science<br>*****<br>Gala Dinner | | |

付録-2

# Major projects for the use of high power linacs

# MAJOR PROJECTS FOR THE USE OF HIGH POWER LINACS

M. Promé
CEA/DSM
Saclay, 91191 Gif/Yvette France

## Abstract

A review of the major projects for high power linacs is given. The field covers the projects aiming at the transmutation of nuclear waste or the production of tritium, as well as the production of neutrons for hybrid reactors or basic research with neutron sources. The technologies which are common to all the projects are discussed. Comments are made on the technical difficulties encountered by all the projects, and the special problems of the pulsed linacs are mentioned. Elements for a comparison of normal conducting linacs versus superconducting ones are given. Finally the technical developments being made in various laboratories are reviewed.

## Introduction

It seems reasonable to place the lower boundary for "High Power Linacs" at the level of 1 MW average power. There is no upper boundary; some projects reach almost 200 MW. Most of these linacs accelerate protons (or $H^-$), with the exceptions of IFMIF (International Fusion Material Irradiation Facility), which is a deuteron accelerator, and of a CW electron linac designed for PNC (Power Reactor and Nuclear Fuel Development Corporation in Japan) [1].

The main purpose of these proton or deuteron linacs is the production of neutrons, by spallation for the proton linacs, or by breaking the deuteron for IFMIF. As far as spallation is concerned, there is a possible trade off of beam current against energy. Above 1 GeV, the number of produced neutrons is roughly proportional to the beam power.

The neutrons are intended to be used in 4 main classes of applications:

1. For transmutation [2], either for treating nuclear waste or for producing tritium. Transmutation requires beams with a power above some tens of MW. For such a power the CW mode is the most convenient and the chosen energy varies from one project to an other from 600 MeV to 1.7 GeV, depending of the neutron flux needed and the technology chosen for the high energy part of the accelerator (normal conducting or superconducting cavities). The beam spot is enlarged from the centimer size at the linac exit to the meter size on the target. For such a large magnification, non linear optics is usually preferred to other systems like raster scanning or linear optics. A non linear optics can give an almost homogeneous power deposit on the target area and is less sensitive to beam displacements at the linac output.
2. Future hybrid reactors are subcritical reactors where the deficit in neutrons is compensated by the neutrons produced by a proton beam shooting directly into the reactor core. Here a CW beam is required, with a power in the range of 10 to 30 MW. On the low side of this range, cyclotrons may be competitors to linacs [3].
3. For basic research with neutrons [4]. Here one needs pulsed neutrons, with a pulse length of about 1 μs. The so-called research reactors have up to now produced abundant continuous neutron fluxes for research in physics. These neutrons have the advantage of being thermalized at a temperature which can be chosen to some extent. But it is very difficult to get pulsed neutrons from reactors (an essential feature for time of flight measurements) without reducing drastically the averaged flux. Most proposed neutron sources are based on accelerators, which can easily produce pulsed beams. In addition, it is not so difficult to obtain the needed public acceptance for a new accelerator than it is for a new reactor. There is no criticity risk with accelerators, and they do not produce long lived radioactive waste in the spallation target. Even if a pulsed mode of operation is more natural for accelerators than with reactors, one cannot get at once from a linac a large average power in very short pulses. This is the reason why a rather long linac pulse is injected into a synchrotron or a storage ring in a multiturn injection mode, then extracted on one turn. The ring behaves as a compressor, or an accelerator-compressor. An efficient multiturn injection requires a non-Liouvillian mechanism: the linac accelerates $H^-$ which are converted into proton when passing through a stripping foil.
4. Irradiation of materials. IFMIF is designed to evaluate the damages in materials created by 14 MeV neutrons, those which are created in the deuterium-tritium reaction of the future fusion reactors. This neutron energy is the reason for the choice of 30 to 40 MeV for the accelerator. To get the required neutron flux, one has to accelerate a rather large beam current.

Regarding the project of the electron linac mentioned above, it is intended to produce a large photon flux for the treatment of nuclear waste by photo-reactions.

There are common features to all the linac projects (except the electron linac to which the rest of this text does not apply). They consist of an ion source, a RFQ, a DTL section (more or less modified) leading to roughly 100 MeV, and a high energy part, usually referred to as CCL (coupled cavity linac). When the beam current at the linac output is in excess of 100 mA for protons, (or below for $H^-$), the first part of the linac (ion source, RFQ and sometimes a part of the DTL section) is doubled. The two beams are then mixed in a funneling process, which consists in interleaving the bunches with the help of an alternate radial deviation produced by an RF cavity. When funneling is used, it is mandatory that the cavities after the funneling use a frequency being an even multiple of the cavities before the funneling (usually twice).

## Normal conducting versus superconducting cavities

As pointed out by R. Jameson [8], "The age of adventure (high risk) in SC is over... Projects can decide to use RT or SC technology on the basis of their performance, cost, availability, flexibility, and upgradability requirements". One will see below that almost all the major projects of high

power linacs considered using SC. Most projects are based on RT cavities, with SC as an option, with the exception of the japanese project that is now rather based on SC. For projects with superconducting cavities, the RFQ and DTL section still in standard room temperature technology. Only the high energy part involves superconducting cavities (but this high energy part represents 90% of the investment). However, SC low energy cavities are being considered for IFMIF as an alternative solution (a Toshiba design, see [8]).

It may not be unuseful to summarize here the classical arguments in favor of SC or against it, since they apply to almost all the projests described below.

1. With the same beam hole, the accelerating gradient may be larger than for RT, reducing significantly the linac length. But actually the usable gradient is not as high as one could think, because the possibility of entering a large amount of RF power per unit length along the linac is limited.
2. Alternatively, with the same gradient one can chose a much larger beam hole, hence a reduced risk of cavity activation.
3. SC cavities are usually short, due to the limited power passing through a single RF coupler. Therefore the cavities have a large velocity acceptance. The same cell length can be appplied to large parts of the linac, offering the possibility of having spare cavities.
4. The needed RF power is less for SC as it is for RT, since there are only small losses in the cavity walls. But these losses occur at very low tempeerature (2 K or 4 K) and cost about 1000 times more at 2 K (or 300 at 4 K) to be evacuated as compared to the same losses at room temperature , requiring powerful cryogenic plants.
5. SC cavities must have thin walls to be efficiently cooled. Lorentz forces mechanically deforms the structure when operated at high gradient. This is a problem especially for pulsed linacs.
6. RF couplers for SC cavities is a subject of concern.
7. Investment cost is not larger for SC than for RT (possibly smaller).
8. Operating cost is smaller for SC.
9. Reasonable prices for CW RF power can be obtained only with large (1 MW) units. Therefore the power must be split between several cavities (4 or 8). This applies for both SC and RT, but RF level and phase is more difficult to control for SC cavities when several of them are fed by a single RF source.
10. SC offers the possibility of upgrading the linac to higher energy and current as the performance of couplers and windows is improved.

SC clearly appears as an emergent technology, but a quantitative study of cost and risk benefits has yet to be done [8]. It appears that the weight of each of the arguments above is evaluated for each project depending of the local context.

### The European Spallation Source

The first phase of the studies for a European Spallation Source is now reaching its term, that is to say that a choice has been made between several possibilities [4–7]. The chosen configuration, at room temperature, is shown on Fig. 1. It consists of a 1.33 GeV $H^-$ linac and two compression rings. The requirements for the proton beam on the target are the following:

1 μs long proton beam on the target
50 Hz repetition rate
5 MW average power
(actually there will be a second target accepting 1 MW at 10 Hz)

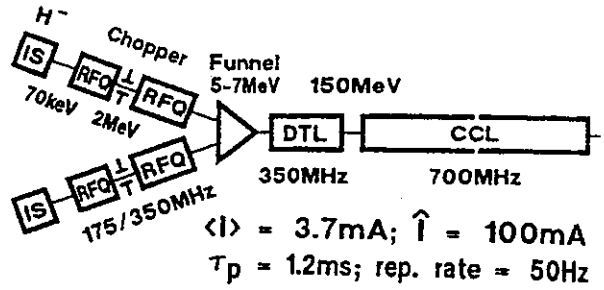


Fig. 1 ESS LINAC, 1.33 GeV, 5 MW.

It may be noted that each proton pulse carries an energy of 100 kJ, which is the subject of some concern with the building of stress waves in the target, and the reason for chosing a liquid (Hg) target.

The linac beam pulse is 1.2 ms long, working at 50 Hz. The injection into the rings must be made in such a way that the rings are not homogeneously filled (40% of the circonference is void), a condition necessary for an efficient extraction. So the 1.2 ms pulse is sliced in 360 ns long micropulses, separated by 240 ns gaps.

As one can see on figure 1, it has been impossible to avoid a funnel, which takes place at the level of of 5 to 7 MeV. With the present state of the art for $H^-$ sources, it would be too difficult to get the required peak current of 100 mA at the linac output with a single ion source. Moreover, the RFQ behaves better for moderate currents. The DTL section is a classical one. The quadrupoles are pulsed in the first cavity to ease the cooling problem in very short drift tubes. An accelerating gradient $E_0T$ of 2.8 MV/m and a synchronous phase of 25° are chosen. It must be noted that such a gradient is substantially higher than the gradients chosen for CW RT linacs, which usually stay at the 1 MV/m level. But the 6% ESS duty cycle allows a gradient comparable to injector linacs, where the power dissipated in the walls can be easily evacuated.

The RF system for the high energy part of the linac consists of 66 4 MW peak power klystrons feedind 264 cavities. That is to say that 1 MW is available for each cavity. The power going into the beam and the cavity wall amounts to 0.75 MW. Field and phase stabilization respectively at 1% and 1° require the 0.25 MW extra power. This is particular to pulsed linacs, where the transient behavior requires a sizable percentage of the total RF power to be correctly mastered.

Side coupled or disk and washer cavities are proposed for the high energy part of the linac. The cavity length (1.27 m to 1.95 m) is short enough to allow a constant cell length inside a cavity. Transverse focusing is provided by doublets located every second cavity. Doublets are favored over singlets as they give a more circular and smaller diameter beam.

Even if RT is the base line design, the ESS project considered the possibility of a SC linac from 150 MeV up to 1.33 GeV, or even 2.5 GeV with a halved current. Figure 2 shows a SC module which consists of a couple of 2 cell cavities. The chosen frequency is 352 MHz, hence the working temperature is 4 K. Several possibilities have been contemplated, with accelerating gradients in the range of 8 to 10 MV/m, RF power per input coupler from 300 to 500 kW and 200 to 300 cavities. The whole energy range can be covered with 20 different structures (20 different β).

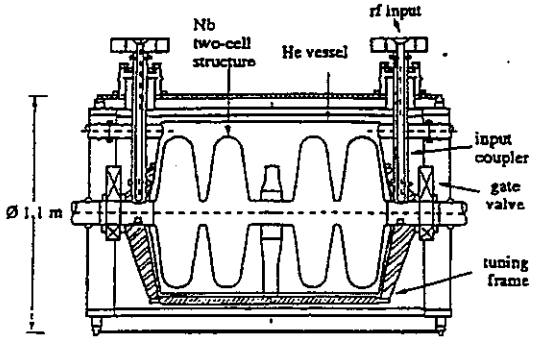


Fig. 2 Cryomodule for the ESS LINAC.

### Other Spallation Sources

There is a large number of spallation source projects around the world [8, 9]. Most of them do not enter in the scope of this paper for various reasons: too low power linac, no linac at all. However it seems useful to mention of few of them:

1. The IPNS project (Intense Pulsed Neutron Source) at Argonne consists of a 400 MeV $H^-$ linac with an average power of 400 kW and one RCS (Rapid Cycling Synchroton) boosting the energy up to 2 GeV, or two RCS in cascade reaching 10 GeV. The average power on the target amounts respectively to 1 MW and 5 MW.
2. The 1 MW level is being reached on a spallation target at PSI near Zürich with a cyclotron.
3. LAMPF has been operating at Los Alamos with an average beam power exceeding 1 MW. It has been proposed [10, 11], to upgrade LAMPF for injecting into a accumulator/ compressor ring. A single turn extraction would allow to obtain a 1 MW average power short pulse spallation source (SPSS). The LAMPF modification would consist in replacing the old part below 100 MeV by a new one including a 100ÊkeV $H^-$ injector, RFQ and DTL sections, the side coupled cavity section being unchanged.
4. It must be noted that the Japanese high power proton linac project (see section 5) includes the possibilty of injecting into a storage ring to obtain a short beam pulse to be sent onto a spallation target.

### The Japanese project

JAERI proposed in 1984 a Neutron Science Research Program (NSRP) [13, 14]. At the core of this program is a 1.5ÊGeV proton linac with an average current of several mA. This program covers OMEGA (transmutation of minor actinides), basic neutron researches, nuclear energy related technologies on material science, neutron irradiation, radioactive beams, etc. JAERI originally proposed a pulsed linac with a 100 mA peak current and 10% duty cycle. An important R/D work has been made for the front end portion of this linac (see section 9). JAERI has now modified the original proposal to meet new requirements. Figure 3 shows the conceptual diagram of the accelerator as it is now. One can see that the high energy part of the linac, above 100 MeV, uses SC cavities. The linac will be operated first in a pulse mode for a spallation neutron source, with a 1 mA average beam current in 2 ms long pulses at 50 Hz, and a $H^-$ source. In a second stage the linac will be operated in a CW mode, the current being raised progressively up to 10 mA in protons. An ultimate goal could be several tens of mA.

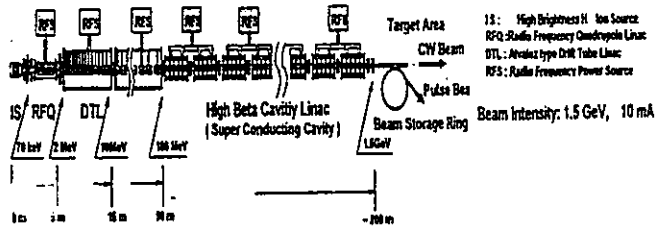


Fig. 3 The Japanese Project.

In addition to the classical advantages in favor of SC (see section 2) there is here an other one: the linac length can be substantially reduced, an important point knowing the limited space available at Tokai-Mura. One drawback in shifting to SC is the necessity to modify the front end design to accept a CW operation. Presently the RFQ is designed to work with a 10% duty cycle and the hot test model of the DTL for 20%. For a reliable operation in a CW mode, the maximum electric field will be reduced from 1.68 EK (Kilparick limit) down to 1.43 EK.

The chosen frequencies are 200 MHz for the RFQ and the DTL and 600 MHz for the SC section. The EIMAC tetrode tube used for the front end has an output peak power of the order of 1 MW. The conceptual design work for high power CW tetrodes and klystrons has been started, taking into account the two modes of operation, pulsed and CW.

Figure 4 shows the schematic drawing of the SC cryomodule. For a maximum electric field of 16 MV/m and an iris radius of 7.5 cm, the accelerating field $E_0T$ is (in MV/m):

2.90 at β = 0.45
5.67 at β = 0.73
7.18 at β = 0.88

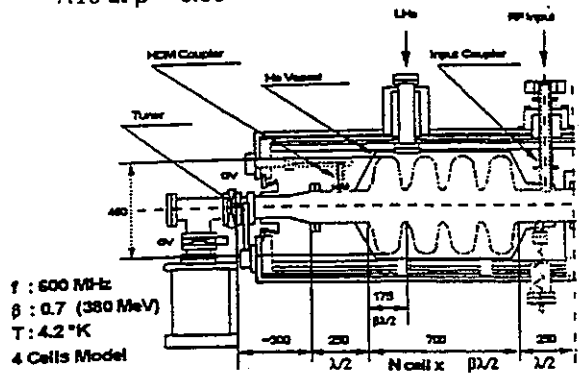


Fig. 4 Half of a cryomodule for the Japanese Project.

With a synchronous phase angle of 30° the total active length is of the order of 250 to 300 m, for a physical total length of 650 to 750 m.

## IFMIF

IFMIF is the project of an International Fusion Material Irradiation Facility. The main motivation for IFMIF is to test the behavior of materials which could be used for DEMO, the Tokomak to come after ITER, presently being designed. The neutron flux should produce 50 dpa (displacement per atom) per year in a volume of 0.1 litre and 1 dpa/year in 10 litres. The IFMIF requirements will be met by two 125 mA, 40 MeV CW deuteron linacs operating in parallel. The target will be a curtain of molten lithium flowing with a speed of 15 m/s.

The IFMIF accelerator is shown on Fig. 5. A dual ion source (one operating, one in stand by) generates a 140 mA deuteron beam at 100 keV. Then an RFQ accelerates 125 mA up to 8 MeV. The final section of the accelerator consists of DTL cavities. Both the RFQ and the DTL are operated at the relatively low frequency of 125 MHz, a conservative approach to minimize the beam losses. There will be ten 1 MW RF power units per linac.

The 8 MeV RFQ is 11.7 m long. It is segmented in 3 longitudinal RF segments that are resonantly coupled through irises in the intermediate end walls. This gives a fair separation of the operating mode from the unwanted longitudinal modes of the RFQ. Each of the 3 RF segments is made from 4 physical pieces. The needed RF power is about 3 MW. All the losses (from 140 mA to 125 mA) occur below 2 MeV.

The DTL section consists of 7 Alvarez cavities with post couplers, each fed by a 1 MW unit. The control of the resonant frequency will be made by controling the temperature of the cooling water. The inner diameter of the drift tubes is 3 cm, the goal for current losses being 3 nA/m. It should be noted that the accelerator may be operated with no acceleration in the last (or the two last) cavity, providing a selectable output energy of 30, 35 or 40 MeV.

The accelerator will be will be operated with $H_2^+$ to avoid activation during testing periods, and pulsed for tune-up and start-up. The beam calibration station (see Fig. 5) will accept the full intensity only with a duty factor < 2%.

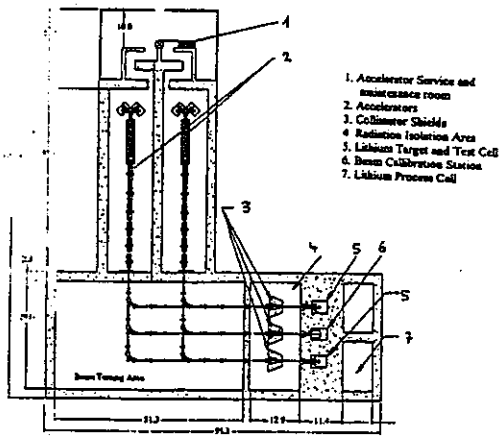


Fig. 5 IFMIF general lay out

The high energy beam transport is basically a FODO channel including "momentum compactor" cavities to fulfill the requirement that the energy dispersion on the target be limited to + and - 0.5 MeV. The beam spot on the target must be 5 * 20 $cm^2$ with a flat top uniformity of + and - 5%. So there is a beam expander section which comprises 2 octupoles separated by 2 quadrupoles. An energy dispersion cavity broadens the beam energy distribution in order to spread the Bragg peak and reduce the maximum power density in the lithium curtain. To prevent beam scraping throughout the channel, a large beam pipe radius is chosen (12 cm). In addition to the achromatic 90° bend that can be seen on figure 5, there will be a 10° kick so as to shield as much of the final optics from the backstreaming neutrons as possible.

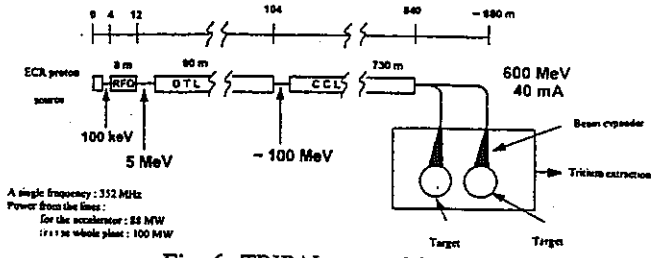


Fig. 6 TRIPAL general lay out.

A thorough RAM (Reliability, Availability, Mintenability) study has been made for IFMIF. The expected availability of the accelerator itself is 88%. It is estimated that the accelerator is designed with sufficient derating but no significant upgrade capability. Additional beam current, if desired, would be provided by adding other 125 mA modules.

## TRISPAL

TRISPAL (TRItium, SPALlation) is the French project for the production of tritium by spallation. The parameters have been changed since a previous presentation [16]. It is now estimated that the amount of tritium to be produced per year will be covered by a 600 MeV proton accelerator with a 40ÊmA beam operating in the CW mode. The design of the accelerator is deliberately conservative, for a number of reasons. The goal is here to convince that an accelerator is as reliable as a nuclear reactor. The key words are: feasability, reliabiliby, proven off the shelf technology, existing RF tubes. This is the reason for a CW low current, low energy accelerator instead of a higher energy, higher current shorter pulsed accelerator, a single RF frequency for which klystrons do exist (350 MHz), of course no funneling, and RT technology, even is a SC version is envisaged as an option.

Figure 6 shows the general lay out of the accelerator, which consists of an ECR proton source, a 5 MeV RFQ working at 1.7 EK, a DTL section up to about 100 MeV, and a CCL section. Then there is a transport channel to the 2 targets, only one being used at a time. The system includes a 82° bend, a FODO channel, a non linear expander and a final 8° bend to avoid backscattered neutrons. The beam spot on the target is a square with a side of 60 to 80 cm.

The chosen CCL uses the slot coupled structure working at the $\pi$ mode, similar to the LEP RT cavities or the ESRF

cavities, with adequat cell length according to the β. Several comments must be made on this choice. First on the frequency: it seems that a 750 MHz CCL would a offer a shunt impedance better by a factor √2; this is untrue if one keeps the beam hole the same at 750 MHz as it is at 350 MHz; in that case one can show [17] that, on the average from 100 to 600ÊMeV, the effective shunt impedance is roughly the same in both cases; what is lost in $Z_S$ is gained on T and $Z_S T^2$ is conserved. The second comment is about the chosen structure; the choice has been made between several possibilities on the gound of construction cost; moreover, there was some suspicion on the behavior of on axis coupling structures under heavy beam loading (the field in the coupling cells may cause multipactoring problems); the fact that the π mode has a zero group velocity is a question of concern for long cavities, but not here for 5 to 7 cells cavities (same cell length inside a cavity). Coming to the RF system, a single 1 MW klystron feeds 8 cavities working at an average effective field $E_0T$ of 1.12 MV/m. There will be 40 klystrons, for an active length of 500 m. It may be noted that here is here some derating of the klystrons: for a nominal 1.3 MW power, they will be operated at 1 MW for a better reliability.

There is no serious feasibility problem for the DTL section, even if lodging DC quadrupoles in the first drift tubes is not easy. However one can have second thought about the necessity of quadrupoles inside the drift tubes. It is a technology which is rather expensive due to the mechanical difficulties of feeding and cooling the quadrupoles, but also the stringent radial tolerance on the drift tube positioning. The tolerance could be substantially relaxed were it not for the quadrupoles. Structures with quadrupoles outside of the drift tubes have been proposed at Los Alamaos (see section 8). The TRISPAL project has a somewhat different approach. It is well known that the effective shunt impedance for DTL is better for long cavities where the end walls have a small relative contribution to the losses. This is true, but if one compares a good long cavity with quadrupoles inside the drift tubes to a short cavity (let say 5 cell) with drift tube shape optimized without worrying for a quadrupole inside, then one ends up with a better effective shunt impedance for the short cavity [17]. This is what is being investigated now as a possibility for optimizing the TRISPAL construction cost.

## APT

APT, the Accelerator for Production of Tritium, is the most advanced project of a family of accelerators studied at Los Alamos for several years (transmutation of waste, plutonium burning, energy production [2]). The present base line is a RT 1.3 GeV proton linac; there are two versions, depending on the quantity of tritium to be produced per year: one with a 100 mA beam, the other with 134 mA; in the latter case there are two front end accelerators and a funnel. Figure 7 gives the main parameters. It is worthwhile to point out that the classical Alvarez DTL section has been replaced by a CCDTL section (Coupled Cavity Drift Tube Linac) [18, 19]. This structure is the solution chosen by Los Alamos to the problem mentioned above (see section 7), after imagining and rejecting an other solution, the BCDTL (Bridge Coupled Drift Tube Linac). One can almost say that the construction of the front end part (RFQ, CCDTL) has already begun under the name of LEDA (see section 9). The CCL section consists of side-coupled cavities. It is estimated that the RT CCL technology is very mature; only a modest effort will be needed to carry out the conceptual design of this base line high energy part of the linac.

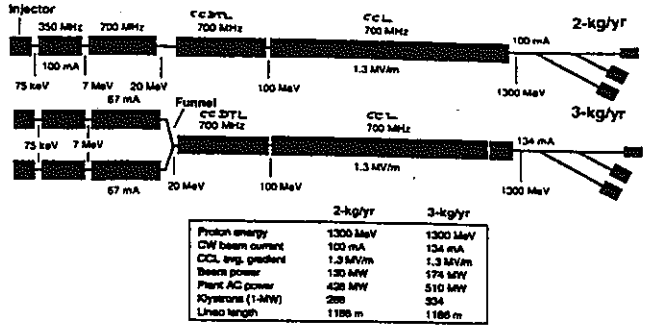


Fig. 7 APT room temperature linac (baseline).

But it is also believed that an SC solution should be emphasized for this high energy section. One can see on figure 8 the two versions of this SC linac: same front end part as RT, SC from 100 MeV up to 1.3 GeV or 1.7 GeV depending on the quantity of tritium. In both versions there is a 100 mA beam, hence no funnel. Cryomodules have been designed for two or four 4 cells cavities. the cavities are equiped with stiffeners to reduce mechanical vibrations. The decision of SC becoming the base line will be taken when electrical and mechanical performance of single cell cavities are confirmed, and when questions concerning the radiation tolerance of niobium are answered. Single cell cavities are now being fabricated and an experimental program for the niobium behavior under radiation has been started.

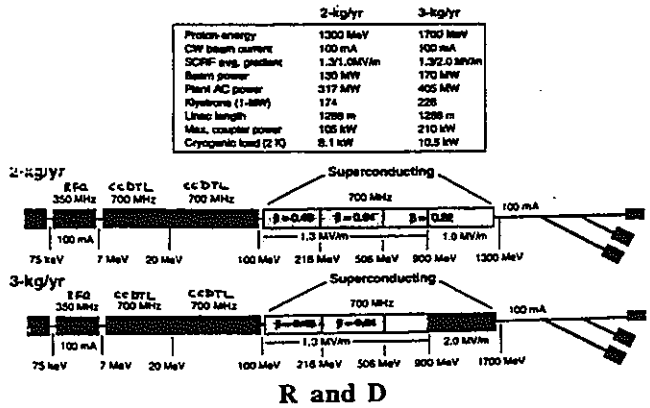


Fig. 8 APT superconducting linac.

## R and D

RFQs have been one of the major breakthrough in accelerator technology. They do work perfectly well in CW mode for low currents, as cyclotron injectors, for instance. Or for high pulsed currents as synchrotron injectors. However their reliability when applied to large CW currents has to be confirmed. It is the nature of RFQ that the focusing field cannot be tuned separately from the accelerating field. High current means strong focusing, high fields, high power density

in the walls; a CW operation brings the difficulties of cooling the structure and avoid sparking between the vanes. There is little experience around the world with the operation of CW RFQs and DTLs [20, 21]. So it would be unwise to start the construction of a large CW linac without a deeper acquaintance with the technology of CW RFQs and DTLs, and also their daily behavior. This is the reason why several laboratories decided to build a front end part of a future large linac.

The Japanese started at Tokai-Mura an important program consisting of a proton source and an RFQ working at 10% duty cycle, and a DTL hot model without beam [22, 23]. The proton source has given 140 mA, of which 120 mA are protons, and the RFQ accelerated 70 mA with a duty cycle reduced to 7%. The measured transparency was 70% for a design value of 95% [14]. This front end was taylored to a pulsed project which is now shifted to CW (see section 5), so it has to be accordingly modified.

At Los Alamos, where RFQ tradition is strong, an "Accelerator Performance Demonstration Facility" has been proposed [24, 25]. A new version, LEDA, (Low Energy Demonstration Accelerator) is now under construction. It is intended to provide design confirmation and operational experience. LEDA will be a nearly exact replica of the APT accelerator front end, 100 mA CW, but will include extra diagnostics and instrumentation. It consists of a proton source, a 6.7 MeV RFQ and a 20 to 40 MeV CCDTL, with an "almost seamless" transition between the RFQ and the CCDTL section. The 8 m long RFQ is made of 4 segments stabilized by resonant coupling.

At Saclay an ion source named SILHI is being constructed. Oriented for TRISPAL and IFMIF, it will be able to deliver CW currents of 100 mA in protons or 140 mA in deuterons. It has been decided recently to go further: the now authorized IPHI program will consist of a 7 m long RFQ plus a 6 m long DTL, accelerating protons up to 12 MeV. Of course the RFQ and DTL design will benefit from the studies made for TRISPAL.

## References


[1] "PNC high power CW electron linac status", T. Emoto et al., LINAC-94, Tsukuba, page 181.

[2] "Transmutation and energy production with high power accelerators", G. Lawrence, PAC-95, Dallas, page 35.

[3] "Important design issues of a high efficiency cyclotron complex to drive the enrgy amplifier", P. Mandrillon et al., EPAC-96, Sitges

[4] "Spallation neutron sources", H. Klein, LINAC-94, Tsukuba, page 322.

[5] "Outline design for the European Spallation Source", editors: I.S.K. Gardner, H. Lengeler, G.H. Rees, ESS report 95-30-M September 1995.

[6] "Accelerator Physics of High Intensity Proton linacs", K. Bongardt, M. Pabst, EPAC-96, Sitges.

[7] "The European Spallation Source Study", 13th Meeting of the International Collaboration on Advanced Neutron Sources, PSI, 1995

[8] "Discussion on superconducting and room-temperature high intensity ion linacs", R. Jameson, EPAC-96, Sitges.

[9] "Conceptual Design for One Megawatt Spallation Neutron Source at Argonne", Y. Cho et al., PAC-93, Washington, page 3757.

[10] "Feasibility Study of a 1-MW Pulsed Spallation Source", Y. Cho et al, PAC695, Dallas, page 363

[11] "A Los Alamos Design Study for a High-Power Spallation-Neutron-Source Driver", A. Jason et al., PAC-93, Washington, page 3760.

[12] "Linac-Driven Spallation-Neutron Source", A. Jason, PAC-95, Dallas, page 1183.

[13] "A proposal of Neutron Science Research program", T. Tone et al., 10th Pacific Basin Nuclear Conference, October 1996, Kobe, Japan.

[14] "Development of High Intensity Proton Acelerator", M. Mizumoto et al, 2nd International Conference on Accelerator Driven Transmutation Technologies and Applications, June 1996, Kalmar, Sweden.

[15] "IFMIF Conceptual Design Activity Interim Report", JAERI memo 08-108, March 1996.

[16] "Conceptual Studies for a High Power Proton Linac", M. Promé, LINAC-94, Tsukuba, page 146.

[17] C. Bourat, private communication.

[18] "A New RF Structure for Intermediate-Velocity Particles", J. Billen et al, LINAC-94, Tsukuba, page 341.

[19] "A versatile, High-Power Proton Linac for Accelerator Driven Transmutation Technologies", J. Billen et al., PAC- 95, Dallas, page 1137.

[20] "RF tuning and initial operation of RFQ1", B. Chidley, EPAC-88, Rome, page 544.

[21] "Initial operation of a 100% duty factor 3 MeV Alvarez linac", J. Ungrin, PAC-81, Washington, page 3495.

[22] "First beam test of the JAERI 2 MeV RFQ for the BTA" M. Mizumoto et al, LINAC-94, Tsukuba, page 113.

[23] "Fabrication and test of the DTL hot model in the R&D works for the Basic Technology Accelerator (BTA) in JAERI", M. Mizumoto et al., LINAC-94, Tsukuba, page 119.

[24] "Review of the APDF and other low-b, high-duty-factor linacs", R. Haedekopf, LINAC-94, Tsukuba, page 328.

[25] "Accelerator Performance Demonstration Facility in Los Alamos", D. Chan et al, LINAC-94, Tsukuba, page 101.

付録-3

# Analysis of Wake Fields on TWRR Accelerator Structure in PNC

# Analysis of Wake Fields on TWRR Accelerator Structure in PNC

S. Tôyama and H. Takahashi*

*Power Reactor and Nuclear Fuel Development Corporation(PNC)*
*4002 Narita, Oarai-machi, Ibaraki-ken 311-13 Japan*

**Brookhaven National Laboratory,*
*Upton NY 11973 USA*

## Abstract

A high power CW (Continuous Wave) electron linac has been developed so as to accelerate 10 MeV-100 mA beam, and its injector section has been completed in 1996 at PNC. It is essential for higher beam acceleration to reduce the beam instability caused by the space charge effect and the beam-cavity interaction. Both are important for PNC linac, because an accelerator with a high beam loading generally has a low accelerating gradient.

In this paper, beam induced fields for the regular section with PNC accelerator structure are examined by means of a numerical wake field analysis. The BBU start current is estimated in the relationship of the wake potential to space charge force in injector section.

## Introduction

The development of a high current electron accelerator is being carried out to target to treat high level nuclear wastes via photo-nuclear reaction which is selective and clean more then the spallation reaction. The elementary design and the experiments[1-3] for the high current linac are in progress using L-band RF source which is effective to a high beam loading. The traveling wave accelerator with an RF feed back called Traveling Wave Resonant Ring(TWRR) is employed to get higher with transfer with a shorter accelerator length, the reasonable cost, and the ease of the maintenance. The accelerator structure has a constant gradient disk loaded type and accelerate 80 pC charge per bunch for 100 mA average current. The accelerating gain from PNC structure is 1.3 MeV which is so low compared with S-band linac that the effect on the beam such as a microwave instability may cause undesirable beam broadening in longitudinal and transverse direction at lower than usual beam current.

In the regular section which beam energy is over than 3 MeV in PNC linac, the beam instability originates from the interaction with the accelerator structure. The analysis for this interaction is recently developed by means of a wake field approach for both circular and linear accelerators. Monopole and dipole components of wake field a nd related loss factors were calculated by ABCI[4] and MAFIA[5] T3 in order to have the potential and voltage compared with the accelerating condition. Finally, the BBU start current was estimated by the scaling of the wake voltage with the voltage and the space charge parameter of the behavior in the envelope equations.

## Definition and Calculation

When charged particle passes through a structure with the speed of light $c$, it produces the electromagnetic field. The wake fields $W_{\|}$ and $W_{\perp}$ [6,7]both for monopole and dipole components are described as

$$W_{\|} = -\frac{1}{Q}\int dz\, E_z(r,\theta,z,(z+s)/c)\ ,$$

$$W_{\perp} = -\frac{1}{Q}\int dz\,(E_{\perp} + c\times B)(r,\theta,z,(z+s)/c)$$

where $E_{Z,\perp}$ and $H_{\perp}$ are the electric and magnetic fields produced inside the cavity, and $Q$ and $s$ are the bunch current and the bunch coordinate, respectively. The coordinate inside the cavity is represented in cylindrical in this case. The associated loss factors $k_0$ and the induced voltage $\Delta V$ are presented as

$$k_{\|} = -\frac{1}{Q}\int ds\,\lambda(s)V_z(s)\ ,$$

$$k_{\perp} = -\frac{1}{Q^2}\int ds\,\lambda(s)V_{\perp}(s),$$

$$\Delta V = 2Q\ k_{\|}$$

where $\lambda$ is a bunch distribution. $V_{Z,\perp}$ is the wake voltage derived by the total beam bunch and the wake potential for the longitudinal and transverse in each. These quantities except the induced voltage are ready to several codes for numerical calculation.

The actual parameters for the calculation used for the beam and the accelerator structure is summarized in Table 1. The typical dimensions of the accelerator structure used are $a$ = 50, $b$ = 90, $t$ = 8 and $D$=24 mm, which are exactly or approximately equal to the actual structure dimensions for PNC linac. The beam bunch shape is assumed filamentary and gaussian shape in the longitudinal direction. Numerical calculation was done

mainly by ABCI because of the less demand of cpu time, while MAFIA was used for 3-dimensional structures which is not available for ABCI. In the case of off-centered beam, MAFIA is suited because of the symmetry free input for the beam parameter.

Monopole and dipole component were estimated to examine the dependence of the bunch shape, the cell distance and cell shape distance.

Table 1 Parameters of wake field analysis.

| | |
|---|---|
| Iris ($a$) | 90 (mm) |
| Boa ($b$) | 50 (mm) |
| Disk thickness ($t$) | 8 |
| Pulse Length | 0.3 ~ 200 (mm) |
| Periodic distance($D$) | 24 ~ 64 (mm) |
| Charge of single bunch($Q$) | 80 (pC) |
| Bunch length | 0.3 ~ 200 (mm) |
| Beam displacement | 0 ~ 20 (mm) |

### Characteristics of Wake Fields for PNC linac

The analysis was carried out for the cases of a single cavities and the accelerator structure consists of many cells in order to make the effects in PNC linac clear.

### Case of Single cavity

In the case of 2.5 mm bunch seen in Fig. 1, there exists one down warding swing which is essentially only a spike in this situation. This picture is magnified for an only shot to display the potential on the beam bunch. Fig. 1 has the abscissas which is presented by volt. The gradient of the curve has a down swing at first which means the gradient of the wake field is negative, which can cause to have an attractive force on particles in the right-shoulder in the bunch. The bias is changed around 10 cm bunch length. The wake potential for 10 cm and 1 cm are 10 V and 50 V in each for each 80 pC of the single bunch. the voltages are small enough to consider the stability for PNC linac.

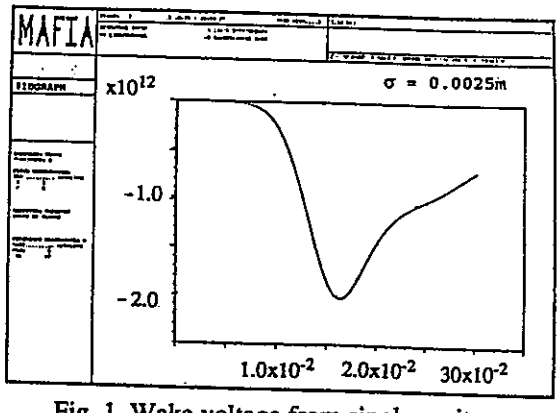


Fig. 1 Wake voltage from single cavity.

The analysis of the potential dependence for an off-centered beam shows that there is basically only a spike both in the longitudinal and transverse wake fields. But MAFIA calculation may neglect calculation of higher frequency area, because of luck of cpu time. This picture notices also that the beam bunch gets an attractive force for the longitudinal wake field at first and a repulsive force for the transverse. The shapes of the potential are the same but the amplitudes are different. The loss factor normalized to a single bunch current and an induced transverse voltage is summarized in Table 2. The deflection voltage for 1 cm off-centered filamentary beam with bunch length of 0.3 cm is almost -200 V which corresponds to 6 KV/m in the beam pipe. This potential is not so strong compared with the potentials in the beam pipe in present colliders like SLC and designed value for SSC. Total loss of a wider beam is reduced for transverse case, while the factor is enhanced for the longitudinal. The energy emission is clearly mainly by longitudinal process. Effectively there is no significance for such a small energy loss into cavity for PNC linac.

Table 2 Loss factor and induced voltage in a single bunch for beam displacement.

| Displacement (cm) | Loss factor* (V)*** | Induced voltage** (V) |
|---|---|---|
| σ= 1 cm | | |
| 0.5 | -17.4 | 112.0 |
| 1.0 | -61.02 | 10.0 |
| 2.0 | -243.8 | 420.0 |
| 3.0 | -548.4 | 630.0 |
| σ= 0.3 cm | | |
| 0.5 | -56.8 | 89.9 |
| 1.0 | -199.9 | 168.8 |
| 2.0 | -798.0 | 338.9 |
| 3.0 | -1792.5 | 511.0 |

* Longitudinal.
** Transverse.
*** Normalized to a single bunch current.

### Case of Accelerator structure for PNC

The examples of wake potentials and the impedances are pictured in Fig. 2 for the longitudinal and transverse wake field resulted from changing the cell displacement. The effect is totally capacitive because of actual bunch length and the speed of an electron beam. The patterns of the potential change very little in different cell numbers. This is caused by that Fourier component of the wake field has stronger fundamental than high harmonics, which can be travel inside the accelerator guide. This seems plausible because the impedance spectrum has a strong peak around 1.25 GHz which mode is $2\pi/3$. The dependence of Fourier component for the bunch length

between 0.3 ~1.0 cm is nearly constant. The strength of the longitudinal wake potential is basically smaller than the gradient from RF in monopole case. In the dipole case, it gets larger, but still is coherent with bunching effect as mentioned in single cavity case. It is notable from general analysis that in the case of 3.3 ~ 10 cm bunch length in which the bunch length is nearly equal to the depth of the cavity, there is strong resonance which is chanced by the accelerator structure. It is seen in the impedance calculation that the resonance of wake field is build by 1.9 GHz RF in the transverse wake potential.

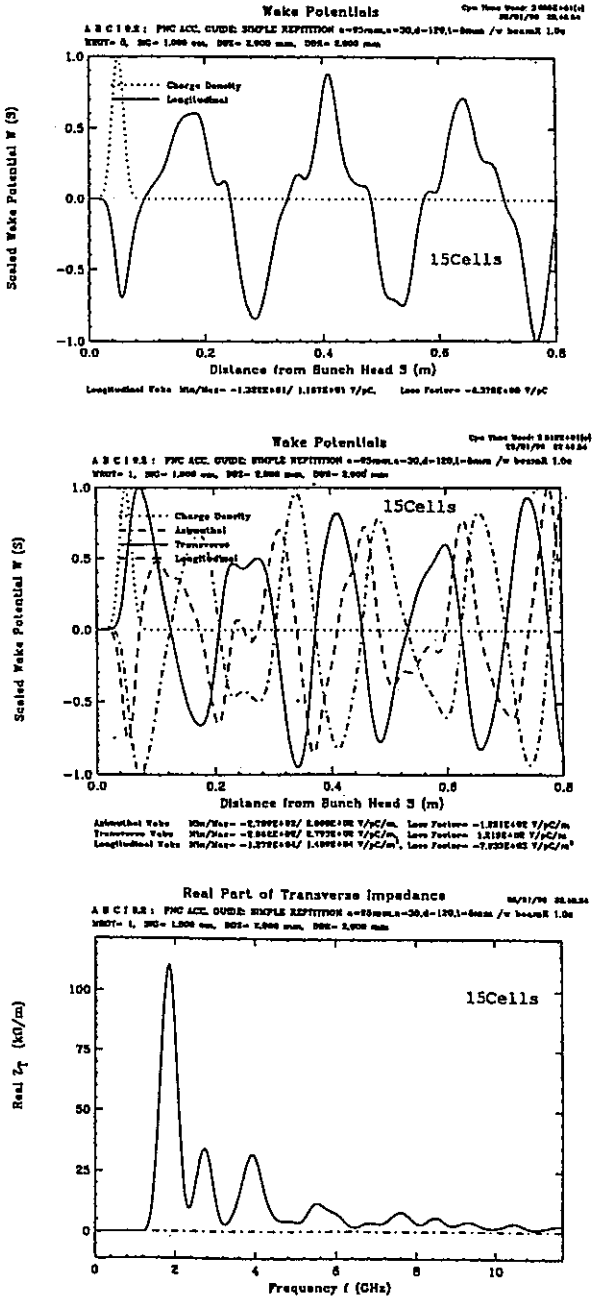


Fig. 2 Wake potential from PNC accelerator structure.

From a numerical evaluation, the transverse spike amounts to -270 V/pC, which correspond to -2.2 kV per bunch. This value is smaller than 100 kV order which appears in modern colliders. Qualitatively, just like a theory of a electron synchrotron , the tune shift by space charge is also applicable to a linac. In the scaling the space charge parameter $\xi$ in the envelope equation from the value of modern colliders to one for PNC linac, the wake transverse voltage is 100 times higher than the voltage from 0.1 A beam. However, the space charge parameter for the wake voltage for 1 cm radius beam is $10^{-12}$ and still $10^{-2}$ smaller than beam defocusing value emerged in colliders. The margin from 0.1 A is order of one hundred. Therefore, from above comparison, BBU starting current is assumed around 5 A for PNC linac.

## Summary and Conclusion

The longitudinal wake field has one down swing followed by many smaller oscillation in the beam condition of PNC linac. It may assist phase stability if the attractive force and repulsive wake can be controlled so as to synchronize with RF bucket. Transverse wake field is 100 times higher than the space charge force but still considerably lower than the wake field of present linear colliders. The wake field in the accelerator guide for PNC linac is formed from the coherent sum of single cells. The longitudinal wake has the same period as RF frequency. The dipole component has -2.2 KV, which is the highest potential of all transverse field. The transverse wake potential in PNC structure is essentially not so high that BBU by the transverse component is expected not to start up to 5 A.

There is a possibility that the longitudinal instability comes first because of phase instability. It is important to observe the bunch lengthening which is common phenomena called microwave instability known circular accelerators. The accumulation of wake field should be estimated for more accurate estimates for the BBU for TWRR. It is important to analyze an overlap integral of higher frequency from the dispersion relation in TWRR which may have a resonance.

## References

[1] S.Tôyama *et al*, "High Power Linac in PNC", Proceeding of 1993 Particle Accelerator Conference, Washington D.C., p546 (1993)

[2] M.Nomura *et al*, "Status of High Power CW Linac at PNC", Proceeding of 1994 European Particle accelerator Conference, London., p546 (1993)

[3] K.Hirano *et al*, "Development of High Power 1.2Mw CW L-band Klystron", Proceeding of 1995 Particle Accelerator Conference, Dallas., p745 (1996)

[4] Y.H.Chin, "User's guide for ABCI Version 8.8", LBL-35258 (1994)

[5] MAFIA group, "MAFIA(_320) The ECAD System", (1994)

[6] O.Napoly *et al*, "A generalized method for calculating wake potentials", Nucl. Instr. and Meth A 334, p225 (1993)

[7] P.L.Morton, "Introduction to Impedance For Short Relativistic Beam", SLAC-PUB-6052 (1993)

付録-4

# Conceptual Design of Beam Dump for High Power Electron Beam

# Conceptual Design of Beam Dump for High Power Electron Beam

H. Takei and Y. Takeda*

*Power Reactor and Nuclear Fuel Development Corporation (PNC)*
*4002 Narita, Oarai-machi, Ibaraki-ken 311-13 Japan*

**Guest Scientist from Paul Scherrer Institut (PSI), Switzerland*

## Abstract

A high power CW (Continuous Wave) electron linac has been developed at PNC and its injector section has been completed in 1996. This paper presents the conceptual design of beam dump for a high power low energy beam (200 kW of 10 MeV electron). It has a Ring and Disk structure. The thermal analysis, stress analysis showed that 200 kW electron beam could be securely stopped in the beam dump. The temperature rise at highest position was estimated to be 343 degree.

## Introduction

Design and construction of a high power CW electron linac to study feasibility of nuclear waste transmutation[1] was started in 1989 at PNC. The injector has been completed and started its operation at 3.5 MeV beam energy in summer 1996 and the whole facility is planned to be commissioned at 1997. Main specification of the accelerator is shown in Table 1.

**Table 1 Main specification of the electron linac**

| | |
|---|---|
| Energy | 10 MeV |
| Maximum Beam Current | 100 mA |
| Average Beam Current | 20 mA |
| Pulse Length | 100μs ~ 4 ms |
| Pulse Repetition | 0.1 Hz ~ 50 Hz |
| Duty Factor | 0.001 ~ 20 % |
| Norm. Emittance | 50 π mm mrad * |
| Energy Spread | 0.5 %* |

* estimated value by simulation

As the beam is a considerably high power and of low energy electron, the average power density of heat generation due to the energy deposition is quite large, so that it is of extreme importance to realize the beam dump to be secured by removing the heat very efficiently. At the same time, radiation shielding of the beam dump is also of the major concern.

## Design

The conceptual design of the beam dump is based on the following design criteria:

(1) to disperse the beam by magnet in front of the beam entry
(2) to stop the beam part by part in spatially separated blocks
(3) to minimize the induction of radioactivity

The first criteria is for making the power density smaller by defocusing/spreading the beam. It is also assuring to avoid mishaps of the pin point beam hitting the component. The second criteria makes also a reduction of power deposition in a small region of the beam dump. The third criteria eliminates the use of water to stop the beam. Liquid target does necessarily increase the total inventory of the radioactive materials.

The concept of the present design is, as shown in Figure 1, Ring and Disk (RD) system : The part where energy is deposited consists of 17 rings and 5 disks (thickness of 5 cm). Each plate is made from OFHC (Oxygen Free High-purity Copper). All the rings have different inside diameters (the beam runs inside this ring.). The frontmost ring has the inside diameter of 19.6 cm and other rings have smaller diameter with increment of 1.2 cm from upstream to downstream.

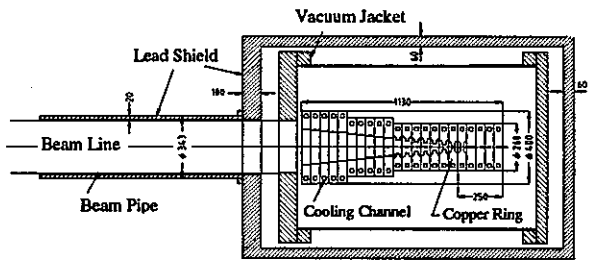


Fig. 1. Beam Dump in cross-section

The beam enters into the cylindrical vessel through a dispersion magnet which is located 2 m front of rings. Since the beam has spatially a Gaussian profile, the inner front edges of rings stop the narrow annual lobe of the beam, from outside as going to the backward. Finally the beam is stopped by the disk set at the backend of the block. Figure 2 is a front view of the inner front edges.

These rings and disks are formed into 4 modular units. Each module is electrically insulated from each

other in order to measure the beam current deposited on them. It can be replaced/exchanged as a unit. In a module a cooling water flows in series from ring to ring. In order to reduce radiolysis of cooling water and to eliminate the vacuum window between the beam dump (target) and the accelerating tube, cooling water is not exposed to direct incident electron beam.

These modules form a total target block and it also electrically insulated from the main body of the beam dump. A total view of this target block is given in Figure 3 and the PNC beam dump is shown in Figure 4.

The problem of connecting between the beam dump and the accelerator (the pressure difference between $1\times10^{-5}$ torr and $1\times10^{-7}$ torr in the accelerating tube) was solved by using a differential pumping stations and a low conductance beam transport tube.

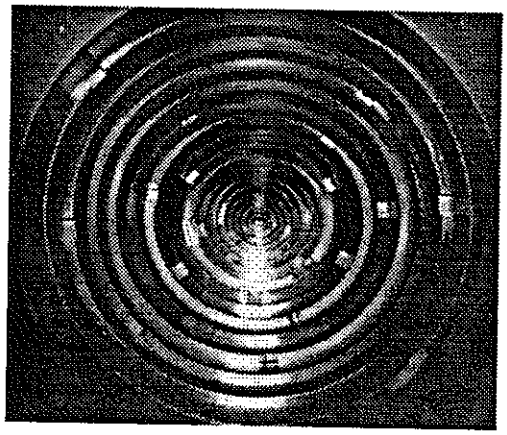

Fig. 2. A front view of the inner front edges

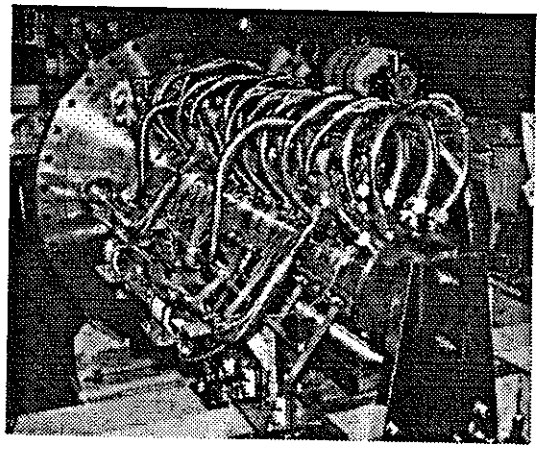

Fig. 3. A total view of target block

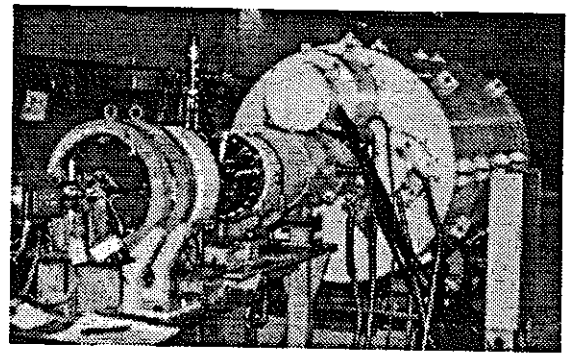

Fig. 4. View of the PNC beam dump

## Thermal and Stress Analysis

Several computer codes were used in order to estimate the temperature rise and the stress of rings with full beam power. This calculation assumed that the transverse beam intensity is Gaussian distribution and the electron is injected to the target block with the angle of incidence varied between 0° and 3°.

Firstly, the power density in the target block is calculated using the EGS4 [2] code. The EGS4 code performs Monte Carlo simulations of the radiation transport of electrons, positrons and photons in any materials. Then we applied the PRESTA algorithm (Parameter Reduced Electron-Step Transport Algorithm) [3], which was developed by Bielajew and Rogers to improve the electron transport in EGS4 in the low-energy region. The maximum power density was estimated to be 2.2 kW/cm³.

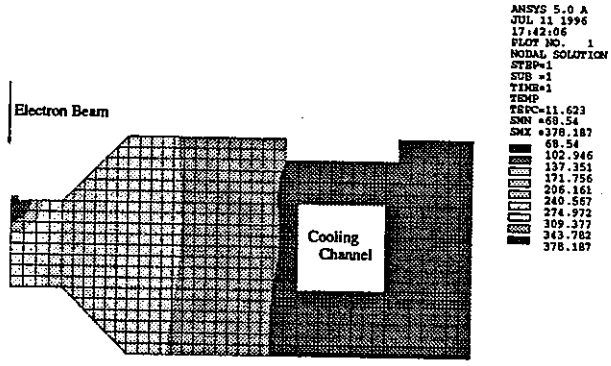


Fig. 5. Thermal analysis of a ring

Using the power densities from the EGS4, we proceeded to the thermal analysis using the finite element method code ANSYS [4]. Examples of the results of the analysis are shown in Figures 5 and 6. They are cross-sectional views of a ring in which stress is estimated to become maximum. The results predicted that the

maximum temperature rise in the ring is at the inner front edge of ring and is 343 degree, and peak stress of 2.3 kg/mm².

Since the Von Mises stress exceeds the yield stress of copper (0.63 kg/mm²), a plastic deformation might be induced over a major portion of the ring. As it is considered that the thermal stress cracking could be generated by this deformation, we design the beam dump such a deformed disk is easily replaced with a new one.

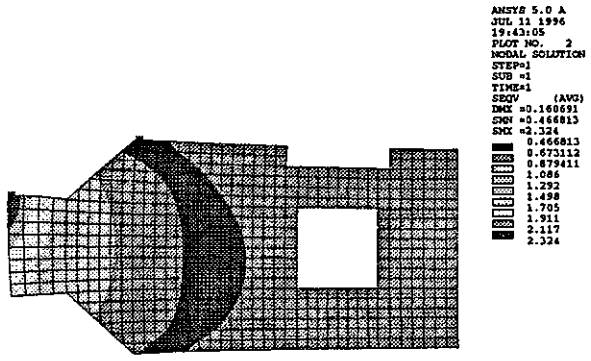


Fig. 6. The Von Mises stresses for the heat loads calculated with ANSYS

## Photon Production

The energy distribution of photons ( γ-rays ) generated by incident electrons in the target block are studied using the EGS4 code. Figure 7 shows the relationship between its energy $E$ and the scattering angle θ of the photon, where θ is the angle from the incident direction of electron beam.

Electrons are particularly susceptible to a large angle deflection by scattering from nuclei and they are backscattered out of the target block. In this context, Figure 7 shows the concentration of backscattered photons in the direction of 180°. A preliminary estimate of the absorbed dose rate in the backward direction (180°) at 1 m is 9000 Gy/h with full beam power.

## Conclusion

A beam dump at PNC, employing the Ring & Disk system, has been designed for the high power low energy beam (200 kW of 10 MeV electron). The beam could be stopped at the inner edge of the rings which are cooled by water.

The maximum power density in the target block is 2.2 kW/cm³ with full beam power assuming Gaussian distribution of the transverse beam intensity. The maximum temperature rise in the ring ( at the inner front edge of ring ) is estimated to be 343 degree.

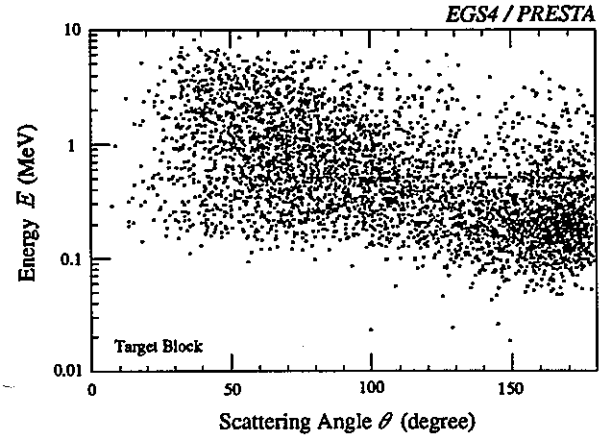


Fig. 7. Correlation between the photon energy $E$ and the scattering angle θ

## References

[1] S. Toyama *et al.*, "Transmutation of long-lived Fission Product ($^{137}$Cs, $^{90}$Sr) by a Reactor-Accelerator System", Proceeding of 2nd International Symposium on Advanced Energy Research (1990).

[2] W. R. Nelson, H. Hirayama and D. W. Rogers,"The EGS4 Code System", SLAC-Report-265, December 1985.

[3] A. F. Bielajew and D. W. O. Rogers, "PRESTA: The Parameter Reduced Electron-Step Transport Algorithm for electron monte carlo transport", Nucl. Instr. and Meth., **B18** (1987) 165.

[4] ANSYS, Ver. 5.0a, Swanson Analysis Systems. Inc.

付録-5

# Design of the NLC positron source

# DESIGN OF THE NLC POSITRON SOURCE

H. Tang, P. Emma, G. Gross, A. Kulikov, Z. Li, R. Miller, L. Rinolfi*, J. Turner, and D. Yeremian
Stanford Linear Accelerator Center, Stanford University, Stanford, CA 94309
* CERN, Geneva, Switzerland

## Abstract

The design of the positron source for the Next Linear Collider (NLC) is presented. The key features of this design include accelerating positrons at an L-band frequency (1428 MHz) and using a rotating positron target with multi-stage differential pumping. Positron yield simulations show that the L-band design yields at the source 2.5 times the beam intensity required at the interaction point and is easily upgradable to higher intensities required for the 1 TeV NLC upgrade. Multibunch beam loading compensation schemes in the positron capture and booster accelerators and the optics design of the positron booster accelerator are described. For improved source efficiency, the design boasts two parallel positron vaults adequately shielded from each other such that one serves as an on-line spare.

## 1 Introduction

The NLC is designed to collide a 90-bunch positron beam with an identical electron beam with a bunch intensity as high as $1.25\times10^{10}$ particles for each machine pulse [1,2]. The beam pulse intensity requirement for the NLC represents more than a 20-fold increase over its SLC counterpart! While the SLC positron source [3], by virtue of its relative design simplicity and its proven operational reliability, is used as a design basis for NLC, significant changes are made to greatly boost the positron beam intensity to meet the NLC needs. In this paper, we will first present a design overview, then concentrate on the important aspects of the design and report on the progress made in the design since the writing of our previous paper [4].

## 2 Design Overview

The NLC positron source is of a conventional type based on $e^{\pm}$ pair production from an electromagnetic shower created in a thick, high-Z target upon bombardment by high energy electrons. Three subsystems comprise the NLC source: a drive beam electron accelerator, a positron production and collection system, and a positron booster linac. Table 1 summarizes the important parameters of the NLC positron source for both its phase-I design and its phase-II upgrade (500 GeV and 1 TeV center-of-mass energy, respectively).

The drive beam accelerator uses S-band (2856 MHz) RF for acceleration and has an injector consisting of a thermionic gun, two subharmonic and one S-band bunchers. The positrons are generated in a $W_{75}Re_{25}$ target, adiabatically phase-space transformed in a flux concentrator and a tapered-field solenoid, and captured in an L-band (1428 MHz) accelerator embedded inside a 0.5-T uniform-field solenoid. Acceleration of the positron beam to 2 GeV for emittance damping occurs in an L-band booster accelerator with a dense array of quadrupole magnets providing transverse focusing.

**Table 1.** NLC Positron Source Parameters

| Parameters | NLC-I | NLC-II |
|---|---|---|
| *Drive Electron Beam:* | | |
| Electron Energy (GeV) | 3.11 | 6.22 |
| No. of bunches per pulse | 90 | 90 |
| Bunch Intensity | $1.5\times10^{10}$ | $1.5\times10^{10}$ |
| Repetition rate (Hz) | 180 | 120 |
| Beam power (kW) | 121 | 161 |
| Beam $\sigma$ on target (mm) | 1.2 | 1.6 |
| Pulse Energy Density $\rho$ (GeV/mm$^2$) | $4.6\times10^{11}$ | $5.2\times10^{11}$ |
| *Positron Target:* | | |
| Material | $W_{75}Re_{25}$ | $W_{75}Re_{25}$ |
| Thickness (R.L.) | 4 | 4 |
| Energy deposition (J/pulse) | 126 | 188 |
| Power deposition (kW) | 23 | 23 |
| *Positron Collection:* | | |
| Tapered field (T) | 1.2 | 1.2 |
| Uniform field (T) | 0.5 | 0.5 |
| Flux concentrator field (T) | 5.8 | 5.8 |
| Flux concentrator minimum radius (mm) | 4.5 | 4.5 |
| Accel. RF frequency (MHz) | 1428 | 1428 |
| Accel. gradient (MV/m) | 25 | 25 |
| Minimum iris radius (mm) | 20 | 20 |
| Edge Emittance (m·rad) | 0.06 | 0.06 |
| Collection efficiency (%) | 19% | 17% |
| Positron yield per electron | 1.4 | 2.1 |
| Positron bunch Intensity | $2.1\times10^{10}$ | $3.2\times10^{10}$ |

The L-band design for the NLC positron capture and booster accelerators is the key to achieving the order of magnitude higher positron beam intensity over that of the SLC positron source. By quadrupling the transverse phase space admittance and boosting the longitudinal phase space admittance as well, it not only immediately provides a >4-fold increase in the positron capture efficiency, but ultimately ensures the upgradability of the source to NLC-II intensities, with a large intensity safety margin.

In operation, system reliability is always a critical issue. The reliability of the positron production and capture system is particularly important since the high radiation levels in these areas would prevent human access for prompt repair in case of hardware failure during a physics run. In addition to engineering the best possible reliability into each component, a most effective way to mitigate the reliability problem is to

build redundancy into the system. In our proposal, two side-by-side positron vaults housing identical positron production and capture systems that are adequately shielded from each other will be built. If one system fails, we may immediately switch over to the other to continue the run. In the meantime, we may wait for the radiation level in the vault with failed hardware to drop and then repair the failed component(s). As long as the mean time to fail exceeds the mean time to repair, which we hope will be the case based on the superior reliability demonstrated by the SLC positron source, such a redundancy design will ensure excellent reliability.

## 3 Target Engineering

By the nature of this design, the positron target that serves the dual purposes of generating an electromagnetic shower upon electron bombardment and inducing $e^{\pm}$ pair production must absorb a considerable amount of energy from the drive beam. The drive beam energy density must be kept below a critical threshold, which depends on the target material, or excessive single pulse beam heating may cause the target to fail. As in the SLC positron source, $W_{75}Re_{25}$ is chosen as the target material because of its high $e^{\pm}$ pair production efficiency and excellent thermo-mechanical properties. Target R&D at SLAC using 20–25 GeV drive electrons and 5–7 R.L. (radiation length) thick targets [5] established a failure threshold for $W_{75}Re_{25}$ due to single pulse beam heating at

$$\rho_{\max} = \frac{N\_E\_}{2\pi\sigma^2} = 1\times10^{12}\,\frac{\text{GeV}}{\text{mm}^2}, \qquad (1)$$

where $N\_$ is the number of drive electrons per pulse, $E\_$ the energy of the electrons, and $\sigma$ the rms radius of the electron beam. Thus, the rms beam radius at the target has been chosen to be 1.2 mm for NLC-I and 1.6 mm for NLC-II, respectively, to keep the beam energy density per pulse about 50% below this threshold.

The $W_{75}Re_{25}$ target, shaped into a ring with an outer radius of 25 cm and a radial thickness of 0.7 cm, will be rotated at a frequency of 2 Hz. In this way, areas of successive beam pulse impacts on the target will be adequately separated and the target will be heated uniformly. Unlike other types of target motions such as trolling, the rotating motion preserves the geometry of the target with respect to the incident drive beam and the emerging $e^{\pm}$ beams as well. Therefore, it is expected to eliminate positron beam intensity modulations that might be induced if the target motion is such that its geometry with respect to the beam changes periodically, as in the SLC source. The target will be cooled from the inner ring surface to which a silver or copper casting containing stainless steel cooling tubes is brazed. With a cooling water flow rate of ~2 l/s and a velocity of ~10 m/s, the steady state temperature of the target is estimated to be ~400°C for the cases of both NLC-I and NLC-II, which is a rather comfortable temperature for $W_{75}Re_{25}$.

The rotating motion along with the necessity to cool the target leads to a design in which the target is attached to a rotating shaft that passes from vacuum where the target resides to atmosphere where a driving motor is connected and cooling water is coupled in and out. The high radiation levels near the target precludes the use of conventional vacuum seals made of organic materials such as viton. Instead of pursuing a vacuum-tight seal, we propose to use multi-stage differential pumping along the length of the shaft with radiation resistant seals that limit conductance relying on tight clearances (<15 μm) between sealing surfaces and long path lengths. Candidate seals include axial and radial face seals, axial and radial labyrinth seals, and magnetic face seals.

Figure 1 depicts a conceptual design of the positron target system with three stages of differential pumping. In such a three-stage design, the first stage could use an oil-free dry scroll pump, the second and third stages could each use a turbomolecular pump backed by a dry scroll pump. If the pressure drops by three orders of magnitude after each stage, which we have reason to believe, then, such a design could easily realize the desired $10^{-7}$ Torr vacuum in the target chamber. A test two-stage differential pumping system with a rotating shaft will be built and experimented to prove the feasibility of this design and also to select the best seals.

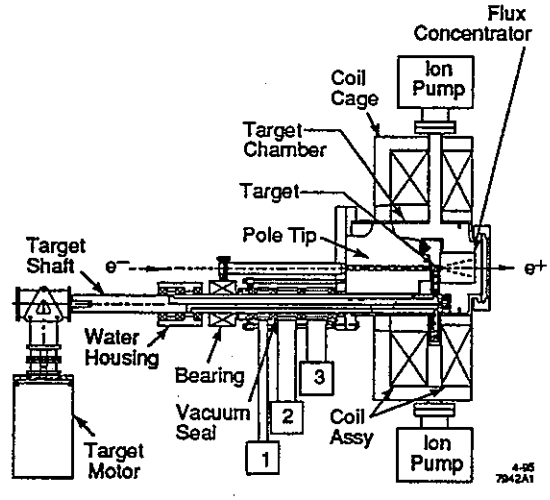


**Figure 1.** A conceptual design of the NLC positron target system with three stages of differential pumping.

## 4 Capture and Booster Accelerators

The capture accelerator is required to quickly accelerate the positron beam to relativistic energies to minimize debunching due to the initial huge energy spread. As electrons are also accelerated along with positrons, it also must be able to handle up to 14 A of multibunch beam loading current in the case of NLC-II. In our design, two 5-m detuned L-band (1428 MHz) structures with an average gradient of 25 MV/m will be used for acceleration, and two 3-m L-band structures sandwiched in between will be used for beam loading compensation by operating off-frequency at 1428 ± 1.428 MHz (i.e., the ΔF method). Each of the acceleration and compensation structures will be driven by two 75-MW L-band klystrons with SLED-I pulse compression. The beam will be

focused by a long DC uniform-field solenoid with a 0.5 T axial field that encloses all four structures.

The 250-MeV positron beam emerging from the capture accelerator will be injected into the booster linac after an achromatic and isochronous bend doublet, which also allows the electron beam to be separated from the positron beam and dumped. The booster linac, designed to accelerate the beam to 2 GeV, consists of 12 accelerating modules. Each module contains two 5-m detuned L-band structures with a minimum iris radius of 20 mm and will be powered by two 75-MW L-band klystrons feeding one SLED-I cavity. The unloaded gradient is about 20 MV/m. Beam loading in the booster linac, with a maximum loading current of 2.75 A, will be accomplished by using the $\Delta T$ method, i.e., injecting the beam before the structure is completely filled. In contrast to the $\Delta F$ method, the $\Delta T$ method offers the advantage of not introducing a large single-bunch energy spread, thus minimizing chromatic emittance growth. The booster linac has roughly a 15% energy headroom.

The lattice for the booster linac is designed using TRANSPORT up to second order. It consists of a dense array of FODO cells whose spacing is scaled approximately as $\sqrt{E}$ along the linac except for the first structure where the cell spacing is kept constant. Most of the quadrupole magnets have apertures large enough to surround the L-band structures, with one or two small-aperture quadrupoles in between successive structures to match the optics across the gaps. The strengths of the large-aperture quadrupoles are kept nearly the same. The phase advance per cell starts at 60° at the beginning of the lattice and gradually decreases to about 25° at the end. This design leads to a quasi-linear $E$ scaling of the maximum $\beta$ function. First-order TRANSPORT calculation shows that the positron beam size is shrunk to <15 mm after the first few structures.

Using the program LINACBBU [6], multibunch beam blow-up due to long-range transverse wake field has been calculated for the booster linac. It is concluded that such effects are negligible for structures with a 10% full-range Gaussian frequency detuning.

## 5 Yield Calculation

The yield for both positrons and electrons from $W_{75}Re_{25}$ targets of thicknesses ranging from 3.5 to 6 R.L. (1 R.L. = 3.43 mm) are calculated using the program EGS [7] for both drive beam energies, i.e., 3.11 and 6.22 GeV. While it is desirable to maximize the positron yield, the volume density of pulse energy deposition in the target must be kept safely below the failure threshold. These considerations leads to the choice for the optimal target thickness to be 4 R.L.. The positron and electron yields per drive electron from such a target are, respectively, 7.2 and 9.0 for 3.11 GeV drive electrons, and 12.5 and 17.1 for 6.22 GeV drive electrons. About 18% and 14% of the drive beam energies are deposited in the target for 3.11 and 6.22 GeV beams, respectively.

The particle rays obtained from the EGS simulation are traced through the adiabatic phase space transformer and the capture accelerator, whose parameters are listed in Table 1, using the program ETRANS [8]. The best positron yield at the exit of the capture accelerator where the beam reaches an energy of about 250 MeV is found to be 1.4 and 2.1 per drive electron for NLC-I and NLC-II, respectively, after applying 6-dimensional phase space admittance cuts. Correspondingly, the positron beam intensities at the 250 MeV point are $2.1\times10^{10}$ /bunch and $3.2\times10^{10}$ /bunch, respectively, each exceeding the respective maximum desired bunch intensity at the IP (i.e., $0.85\times10^{10}$ and $1.25\times10^{10}$) by a factor of 2.5.

Using the program TURTLE, the positron rays are further traced through the booster linac, whose alignment is assumed to be perfect. After applying a 0.06 m-rad transverse emittance cut and a ±2% energy spread cut, it is found that beam transmission through the booster linac is about 95%. While structure and magnet misalignments are inevitable in a real machine, the transverse and energy admittances of the pre-damping ring with an energy compressor are 0.09 m-rad and ±3%, respectively, or 1.5 times greater than the cuts applied to the rays traced to the end of the linac. These two factors have offseting effects on the beam transmission. Thus, the large intensity safety margins after the capture accelerator are almost fully preserved to the end of the booster linac.

## Acknowledgments

We thank J. Clendenin, S. Ecklund, W. Nelson, K. Thompson, T. Umemoto, and M. Woodley for their valuable help. This work is supported by Department of Energy through contract DE-AC03-76SF00515.

## References

[1]. For details on the NLC parameters and its design, see The NLC Design Group, "*Zeroth-order Design Report for the Next Linear Collider*", SLAC Report 474, 1996.

[2]. For early works on the NLC positron source, see S. Ecklund, "NLC positron source - A first look", SLC Positron Source Group internal memorandum, 3/22/90; and H. Braun, et al, "A possible design for the NLC $e^+$ source", Proc. of EPAC92, vol. 1, p. 530, 1992.

[3]. "*SLC Design Handbook*", SLAC (1984).

[4]. H. Tang, et al., "The NLC positron source", Proc. of the 1995 Part. Acc. Conf. and Intern. Conf. on High-Energy Accel., Dallas, Texas, 1995, p. 1033.

[5]. S. Ecklund, "Positron target material tests", SLAC-CN-128, 1981. Note: the effective area for a Gaussian-shaped beam with a distribution width $\sigma$ is $2\pi\sigma^2$, not $\pi\sigma^2$.

[6]. K. Thompson and R. Ruth, "Controlling transverse multibunch instabilities in linacs of high energy colliders", Phys. Rev. D 41, 964 (1990).

[7]. W. Nelson, H. Hirayama, and D. Rogers, "The EGS4 Code System", SLAC-Report-265, 1985.

[8]. H.L. Lynch, "ETRANS", SLAC memorandum, 1989.

付録-6

# Temperature stabilisation of the accelerating structure

# Temperature stabilisation of the accelerating structure

Frank-R. Ullrich
MKK2, DESY, Notkestraße 85
Hamburg, Germany

**Abstract**

An important issue for the operation of a Linear Collider with heavy beam loading is the temperature stability of the accelerating structure. The phase and energy error is a function of the temperature distribution on the surface of the accelerating structure. Calculations prove, that keeping the temperature constant at a specific point on constant gradient accelerating structure minimises the energy error. This will be used for a feedback system. The temperature at this point is a function of the inlet water temperature, the average RF-power and the beam loading.

## Temperature Distribution

An important issue for the operation of a Linear Collider with heavy beam loading is the temperature stability on the accelerating structure. The heat source is the difference of the total input power and the power extracted by beam loading. This difference can be calculated as the vector sum of the accelerating voltage and the beam loading. The shunt impedance, the altennation , the repetition rate and the pulse length are additional parameters. The phase error itself is a function of the temperature distribution calculated by this difference voltage. It is a function of the wavelength, the group velocity, the thermal expansion coefficient and the temperature difference between the steady-state situation and the instantaneous average temperature at every point on the surface [1].

The taper of the group velocity is linear and its value at the inlet side is ≅ 4% and at the outlet side ≅ 1.3 % of the velocity of light. The temperature rises almost linear, but the temperature distribution on the surface is not.
In order to calculate this temperature distribution the following assumptions were made :

- the heat flow over the circumference is at every point the same
- because of the symmetry only 1/8 of the geometry is calculated
- the temperature gradient over the thickness has been neglected
- the water inlet and outlet are on the same side as the beam input (counter flow)

The following picture shows the average temperature between the cooling tubes.

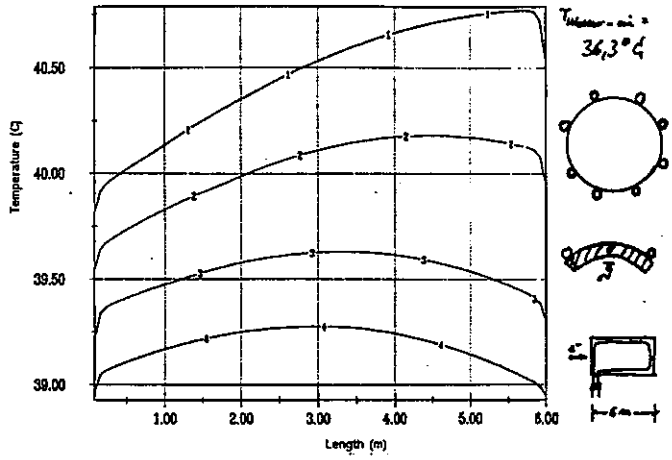


Fig. 1 : Distribution of the surface temperature
curve 1 : no beam
curve 2 : beam current 100 mA
curve 3 : beam current 200 mA
curve 4 : beam current 300 mA

The temperature at the surface rises along the length of the structure in absence of beam current. With increasing beam current the power which is dissipated along the structure decreases. Therefore the heat flow into the water is lower at the end of the structure than at the beginning. This effect is more pronounced with increasing beam current. Because the heat flow from the surface to the water is a function of the temperature difference between them, the surface temperature increases at first and then decreases along the length with increasing currents.

The strong gradients on both ends are produced by the heat flow into the tubes and in addition the return of the water at the end.

The temperature distribution in a 3D-plot is shown in the next picture. The beam current is 300 mA

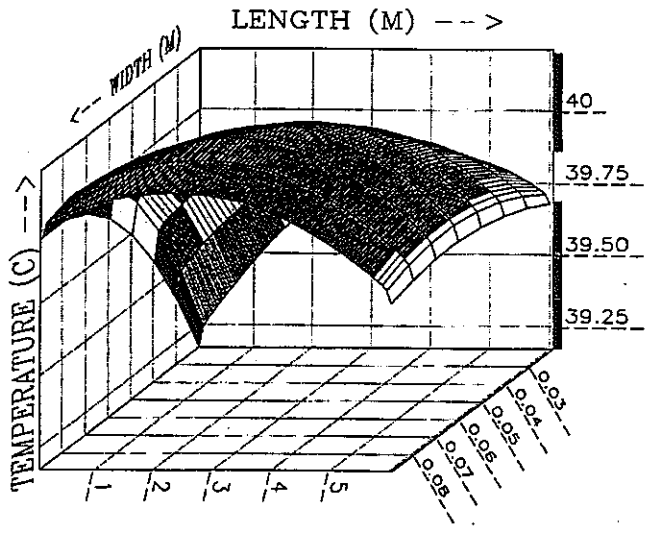


Fig. 2 : Distribution of the surface temperature
beam current 300 mA

The next picture shows the phase error caused by the temperature distribution from figure 1. The temperature for the steady-state system was arranged to be 40 $^{0}$C with a constant temperature at the inlet.

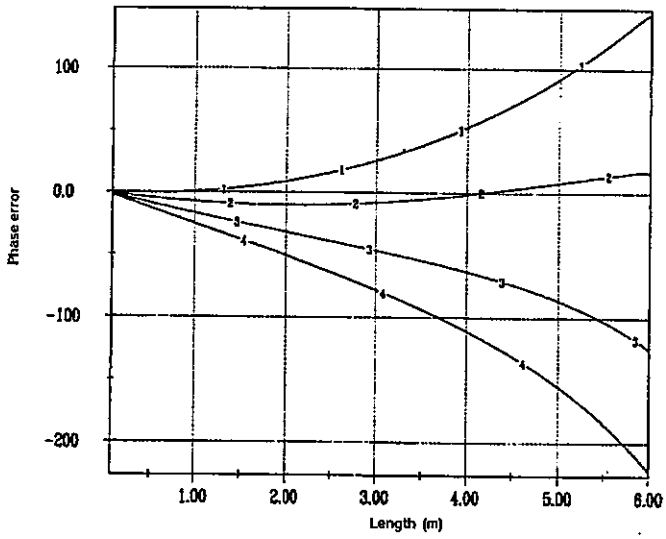


Fig. 3 : Integrated Phase error along the section
curve 1 : no beam
curve 2 : beam current 100 mA
curve 3 : beam current 200 mA
curve 4 : beam current 300 mA

The integrated phase error turns into a beam energy error along the structure length. This energy error on the other hand can be minimised by changing the inlet water temperature unless the integrated phase error is zero, which is always possible because positive and negative phase deviations appear along zero. Calculation shows that at a specific point the temperature remains constant with varying beam or RF power, and varying inlet water temperature for compensation.[2]

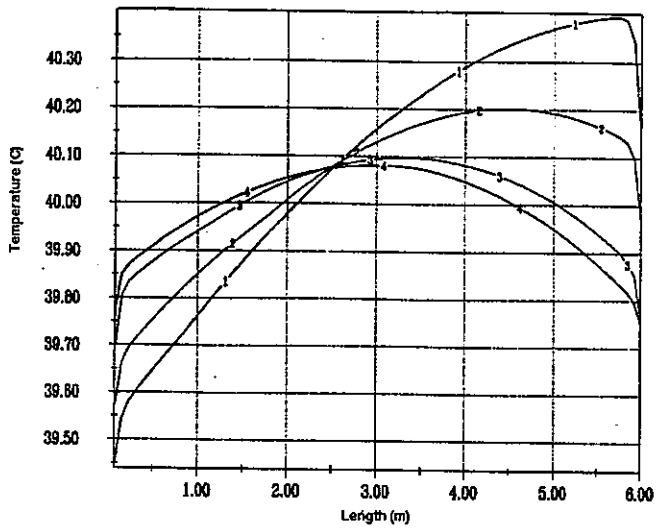


Fig. 4 : Surface temperature with optimised inlet water temperature in order to cancel the sum of the single cell phase error towards the end of the structure
curve 1 : no beam
curve 2 : beam current 100 mA
curve 3 : beam current 200 mA
curve 4 : beam current 300 mA

### Cooling circuit

There are two layouts for the cooling circuit of the linac :
The **first** one is for the test-facility. The main demand for this cooling circuit was the high temperature stability over a large range of power deviations.[3]
The **second** is for the overall layout. The main demand here was to have a simple cooling system with only a few elements but flexible power handling capabilities

For the control of both systems the same elements will be used :
the temperature is measured by a sensor at the specific point, the temperature of the inlet water and the RF-power difference between the input and output. The last one will be used for a fast feedback system: with beam loading a definite input temperature is required and therefore it is possible to change the inlet water temperature before the surface temperature changes. The time available to do this depends on the water flow and the heat capacity of the structure and is about two seconds. Therefore in both systems a hot and a cold line is required and the reqired temperature is mixed by fast pneumatic mixing valves.

At the test-facility the solenoid of the klystron is used as the main heat source for the hot line and for the power reduction ( cool line ) a heat exanger. The rectangular waveguides have a similar control system. The scheme is presented in the next picture

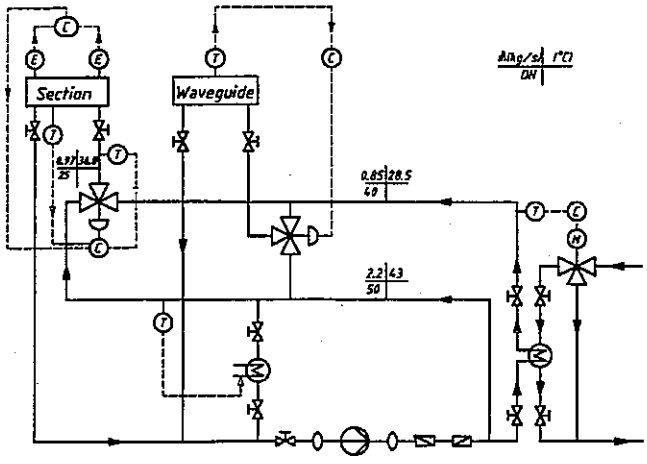


Fig. 5 : Outline of the cooling system for the test-facility

For this circuit a simulation [4] was made ( without the feedback-system !): the power in the section and in the waveguide was reduced by a factor of five ( this means e.g. changing the repetition frequency from 50 Hz to 10 Hz ). The next picture shows the result:

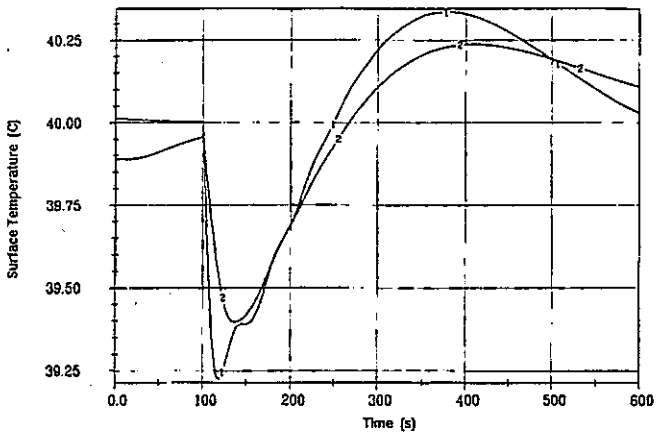


Fig. 6 : Temperature of the surface by changing the repetition frequency from 50 Hz to 10 Hz
curve 1 : accelerating structure temperature
curve 2 : waveguide temperature

For the Linac Collider the klystron collector is used as a main heater source. It isn't possible to connect the heater with the supply water tube because the waterflow wouldn't be enough for cooling the section. Therefore it is connected with the return water tube and so a booster-pump is needed. The next picture shows such a possibility using only a few elements but on the other hand not applicable for a large range of power changes.

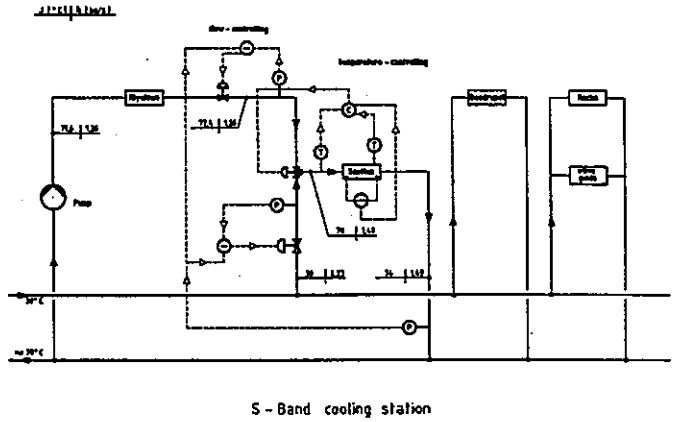


Fig. 7 : Outline of the cooling system, overall layout

For this circuit a simulation was also made without the advantages of the feedback-sytem for the control. The next picture shows the inlet water temperature into the structure and the structure temperature when the power into the structure and klystron is reduced to a third of the previous value

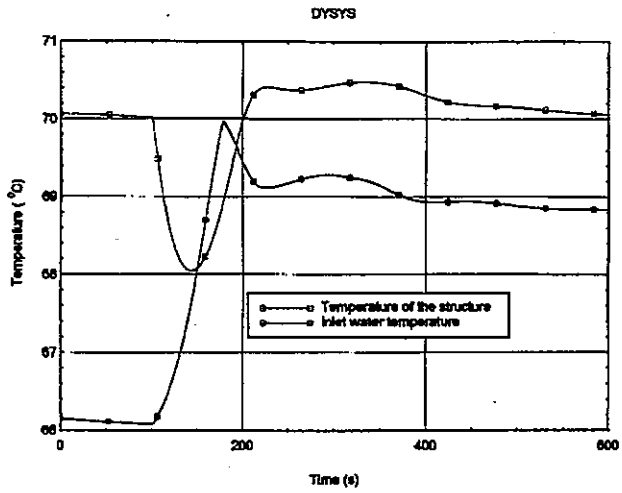


Fig. 8 : Temperatures by changing the power into the structure and klystron

## References

[1] P. Lapostolle, A.Septier, 'Linear Accelerators Accelerating Structures Technology ', North Holland Publishing Company, Amsterdam 1980
[2] J. Hamsom, 'High duty factor electron linac'
[3] J.G. Noomen, N.Geuzebrouk, C. Schiebaan, ' A modular cooling system for the MEA high duty factor electron linac, IEEE Transactions on Nuclear Science, Vol NS - 28, No 3
[4] Frank-R. Ullrich, 'Leistungsrampen des PETRA-Ringes' , MKK-Aktennotiz 24/91 , DESY Internal Report

付録-7

First experimental results of the BNL inverse free electron laser accelerator

# FIRST EXPERIMENTAL RESULTS OF THE BNL INVERSE FREE ELECTRON LASER ACCELERATOR

A. van Steenbergen [1*], J. Gallardo[1**], J. Sandweiss[2], J-M Fang[3]

[1]Brookhaven National Laboratory, Upton NY 11973
[2]Physics Department, Yale University, New Haven CT 06511
[3]Department of Applied Physics, Columbia U., New York NY 10027

**Abstract**

A 40 MeV electron beam, using the inverse free-electron laser interaction, has been accelerated by $\Delta E/E$ = 2.5 % over a distance of 0.47 m. The electrons interact with a 1-2 GW $CO_2$ laser beam bounded by a 2.8 mm ID sapphire circular waveguide in the presence of a tapered wiggler with Bmax ≈1 T and a period 2.89cm ≤ $\lambda_w$ ≤ 3.14 cm. The experimental results of $\Delta E/E$ as a function of electron energy E, peak magnetic field Bw and laser power $W_l$ compare well with analytical and 1-D numerical simulations and permit scaling to higher laser power and electron energy.

## Introduction

The study of the Inverse-Free Electron-Laser (IFEL) as a potential mode of electron acceleration has been pursued at Brookhaven National Laboratory (BNL) for a number of years [1-4]. Recent studies have focused on the development of a low energy, high gradient, IFEL accelerator [5] as a first step toward a multi-module electron accelerator of maximum operating energy of a few GeV. Experimental verification of the IFEL accelerator concept was obtained in 1992 [6] , using a radiation wave length of $\lambda$ = 1.65 mm, and more recently [7] using a wavelength of 10.6 μm. In this report further experimental evidence of the IFEL interaction ($\lambda$ = 10.6 μm) is presented. The experiment used a 50 MeV electron beam, a 1-5 GW $CO_2$ laser beam provided by BNL's Accelerator Test Facility (ATF) and a uniquely designed period length tapered wiggler.

The wiggler is a fast excitation electromagnet with stackable, geometrically and magnetically alternating substacks of Vanadium Permendur (VaP) ferromagnetic laminations, periodically interspersed with conductive (Cu), nonmagnetic laminations, which act as eddy current induced field reflectors [8,9]. Four current conducting rods, parallel to the wiggler axis, are connected at the ends of the assembly, constituting the excitation loop that drives the wiggler. The overall wiggler stack is easily assembled, is compressed by simple tie rods, and readily permits wiggler period ($\lambda_w$) variation. Configured as a constant period wiggler, $\lambda_w$ = 3.75 cm and $B_{max}$ = 1 T, the system has shown [10] an rms pole-to-pole field variation of approximately 0.2 %.

The $CO_2$ laser beam is brought into the IFEL interaction region by a low loss dielectric ($Al_2O_3$ ,sapphire) circular waveguide which evidenced very good transmission properties [11] of the high power $CO_2$ laser beam. Extensive studies were carried out to establish optimum coupling into the guide and to measure the transmission loss of the long (1.0 m) extruded single crystal sapphire guides. Also, because of the overmoded guide configuration (ID = 2.8 mm), attempts were made to determine the transverse mode spectrum. To this end various wave guide configurations were tested at low laser beam power with the beam focused to a Gaussian waist with adjustable radius at the entrance of the waveguide. The beam profile was measured using a pyroelectric vidicon TV camera combined with digital frame grabber. For the 2.8 mm. ID sapphire dielectric guide a laser power attenuation factor of 0.2 dB/m was measured. The laser beam profile within the guide was inferred by measuring the beam diameter at the guide exit for various guide lengths.The results show that, commensurate with the near constant beam profile within the guide, the mode structure is dominated by the guide fundamental mode only. This is in accord with the absence of mode mixing reported in Ref.[11] for filamentary sapphire guides for $CO_2$ laser radiation transport.

In the IFEL accelerator, the electron beam is accelerated by the interaction with the laser radiation wave in the medium of a periodic wiggler field. The theoretical description of the interaction has been given by a number of authors [3,12]. Approximate analytical expressions derived in Ref.[3] were used to parameterize a single acceleration stage. Subsequently, 1-D and 3-D simulation programs were written solving the self consistent system of Lorentz equations for the electrons and the wave equations for the input laser field as discussed in Ref. [12]. The 1-D program has been used to determine the self-consistent wiggler period length and its taper for given values of electron beam energy and laser power and to calculate the bucket acceptance and bucket leakage for a single or multi module accelerator. The 3-D code has been used to study beam walk-off, transverse phase space distributions and emittance growth.

### Experimental Arrangement and Result

Extensive IFEL simulation studies were carried out both for a single IFEL accelerator module and for a sequence of IFEL modules. The objective of the present experiment was a proof of principle performance of a single IFEL unit incorporated in beam line II of the ATF [13,14]. A schematic layout, specific to the IFEL experiment only, is shown in Fig.1. Beam transport downstream from the nominal 50 MeV Linac is so dimensioned as to yield a dispersion free IFEL interaction region. The electron beam, at the IFEL location, is matched vertically to the natural wiggler betatron amplitude $\beta_y = 0.17$ m, $\alpha_x = 0.0$ and to a horizontal amplitude $\beta_x = 0.3$ m, $\alpha_x = 0.0$ . Downstream of the IFEL interaction region the optical system is configured as a momentum spectrometer with adjustable dispersion magnitude ($0.0 < \eta_p < 3.0$ m) at a diagnostic endstation; there the beam momentum dispersion is measured by means of a phosphor screen-vidicon TV camera-Spiracon frame grabber. Also shown schematically in Fig.1 is the $CO_2$ laser beam entry into the interaction region vacuum envelope through a ZnSe window, and its propagation as a free-space mode, to the sapphire dielectric waveguide entry. With deliberation, the dielectric guide was taken to be 0.6 m in length, whereas the accelerator module length (wiggler length) was set at 0.47 m. This was done to approximate a mode matching section, enhancing thereby the mode purity in the IFEL module proper.

The design parameters used in this IFEL accelerator experiment are listed in Table 1. With optimized overlap of the electron and CO2 laser beams, both spatially and timewise, and the interleaving of the lower repetition rate $CO_2$ laser pulses with the higher repetition rate electron beam pulses, the IFEL electron beam acceleration could readily be established. Electron acceleration was measured with the spectrometer at the diagnostic screen. An example of the momentum spectrum of the unaccelerated and accelerated electrons is given Fig.2, where the beam intensity distribution is shown versus $\sqrt{\beta_x \varepsilon_x} + \eta_p \Delta p/p$, with the spectrometer optics adjusted so that $\eta_p \Delta p/p >> \sqrt{\beta_x \varepsilon_x}$ . Optimization of the IFEL effect and exploration of parameter space,

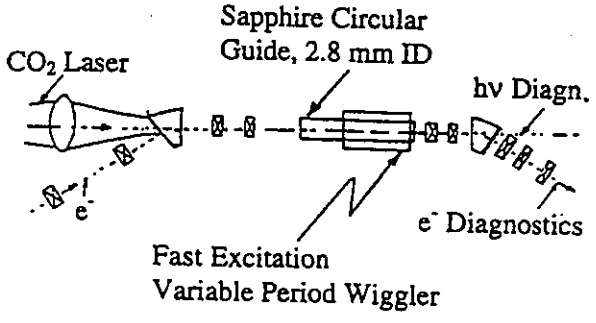


Fig.1, Schematic of the Experimental Configuration

Table 1
IFEL Experiment, First Phase

| | | | |
|---|---|---|---|
| $e^-$ beam | Injection Energy | 40.0 | MeV |
| | Exit Energy | 42.3 | MeV |
| | <Accel.Field> | 4.9 | MV/m |
| | Current, nominal | 5 | mA |
| | N(bunch) | $10^9$ | $e^-$ |
| | I(max.) | 30 | A |
| | $\Delta E/E$(one $\sigma$) | $\pm 3.10^{-3}$ | |
| | Emittance (one $\sigma$) | $7\ 10.^{-8}$ | m.rad |
| | Beam radius | 0.3 | mm |
| Wiggler | Wiggler Length | 0.47 | m |
| | Section Length | 0.6 | m |
| | Period Length, $\lambda_w$ | 2.9--3.1 | cm |
| | Wiggler Gap | 4 | mm |
| | Field max. | 10 | kG |
| | Beam oscill.,$a_{1/2}$ | 0.16-0.2 | mm |
| $CO_2$ Laser | Power, $W_l$(Laser) | $10^9$ | Watts |
| | Wave Length, $\lambda$ | 10.6 | μm |
| | Max.Field, $E_o$ | $0.78\ 10^3$ | MV/m |
| | Guide Loss, $\alpha$ | 0.05 | $m^{-1}$ |
| | Field Attenuation | 0.26 | dB/Sect. |
| | Pulse, (fwhm) | 220 | psec |
| | $A_o$ | $1.53\ 10^3$ | |
| | $r_o(L_w/2)$ | 1.0 | mm |

with variation of the electron beam injection energy, $CO_2$ laser power and wiggler maximum magnetic field magnitude was carried out in several consecutive runs, the results of which established the unambiguous signature of the IFEL acceleration. This is illustrated in Figs.3 and 4, where $(\Delta E/E)_{IFEL}$ is shown both as given by the 1-D model simulations and as obtained experimentally. Fig.3 shows the relative energy gain for $B_w$ and $W_l$ constant; in Fig.4 the plot $(\Delta E/E)_{IFEL}$ vs. $B_w$ is given.

The approximate IFEL design equations [3] are:

$d\gamma/dz = A(K/\gamma)f(K)\sin\psi$ with $\psi = (k + k_w)z - kct$ (1)

where the normalized laser electric field is $A = (e/mc^2)(1/R_o)(\pi W_l Z_o)^{1/2}$, $K = (eB_w\lambda_w)/(2\pi mc) \approx 2.7$ is the wiggler parameter, $f(K) \approx 0.38$ is a correction factor due to the linear polarization of the wiggler, $Z_o = 377\ \Omega$, $R_o$ is the waveguide radius and k, $k_w$ are the radiation and wiggler wavevectors, respectively. The resonance condition leads to:

$\lambda = 0.5\ \lambda_w/\gamma^2(1 + K^2/2)$ (2)

The relative energy gain of the electron beam in a wiggler of length $L_w$ is:

$\Delta\gamma/\gamma = (\Delta p/p)_{IFEL} = A(K/\gamma^2)f(K)\sin\psi_r L_w$ where (3)

$\psi_r$ is the resonance phase (45° for optimum bucket size).

In Fig.3 the solid line shows the results of the numerical simulations with laser power $W_l = 1$ GW and $B_w = 10$ kG normalized to the maximum experimental value. The agreement of the simulations with the experimental results are good. Similarly, in Fig.4 experimental results are compared with the simulations for 35 MeV and 40 MeV, in both cases the agreement is good. The maximum $(\Delta p/p)_{IFEL}$ for initial electron energy

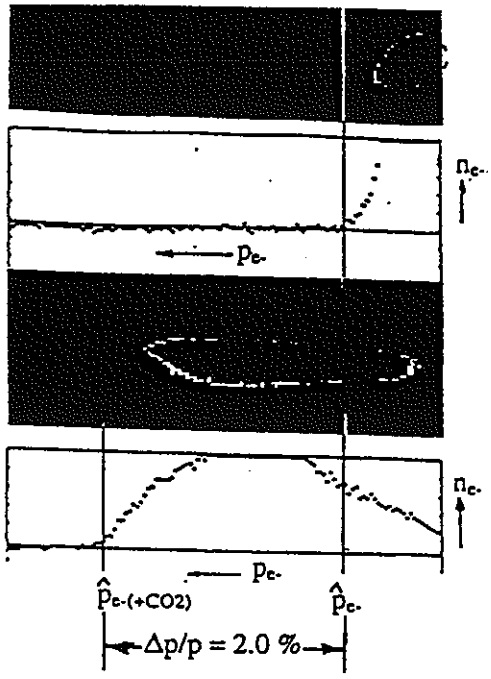


Fig. 2, Momentum Spectrum of the unaccelerated and IFEL accelerated electron Beam
$E_i = 40$ MeV, $B_w = 10$ kG, $\lambda_w = 2.9$ - 3.1 cm, $W_l = 1$ GW

of 35 MeV leads to a value of the magnetic field $B_w$ = 8.35 kG, to be compared with the experimental value of 8.44 kG, and for E = 40 MeV, the calculated $B_w$ is 9.98 kG and the experimental value was $B_w$ = 9.96 kG.

In conclusion, the IFEL acceleration of a 40 MeV electron beam by $\Delta E/E$ = 2.5 % with a 1 GW $CO_2$ laser and a tapered wiggler with peak field on axis of 10 kG has been confirmed. Agreement with the model predictions is satisfactory, permitting the scaling of anticipated results to higher laser power. Present IFEL operation is limited to a maximum laser power of $\leq 2$ GW. With the upgrading

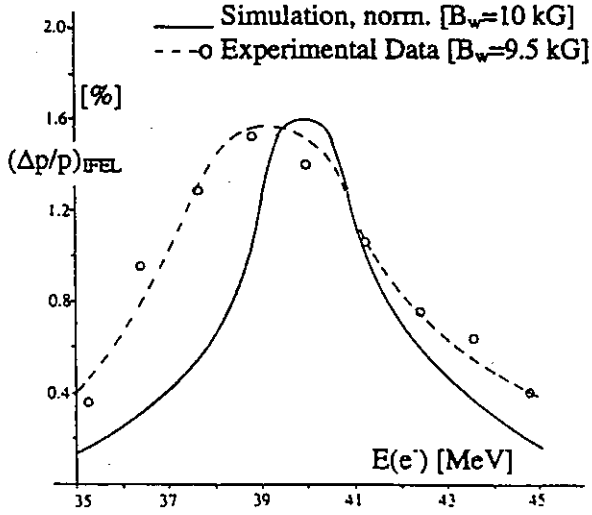


Fig.3, Relative Energy Gain $\Delta E/E$ vs E, with $B_w$, $W_l$ constant

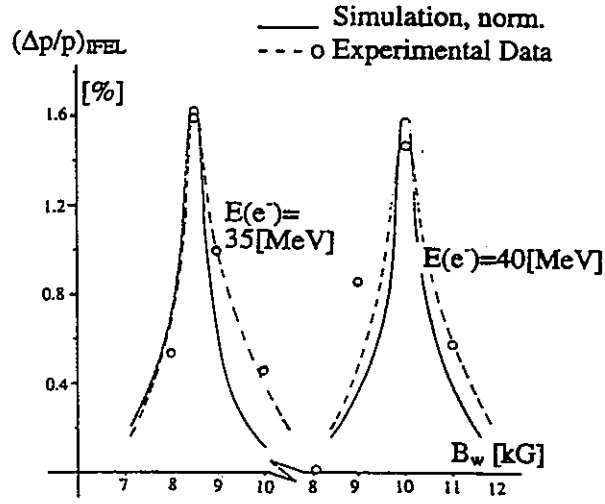


Fig.4, Relative Energy Gain vs $B_w$ with E and $W_l$ constant

of the ATF $CO_2$ laser to the 1TW level as presently underway, an IFEL mean acceleration gradient of 100 MeV/m might become achievable.

The authors wish to acknowledge the invaluable support and participation in the experiment of the ATF staff M. Babzien, K. Batchelor, I.Ben-Zvi, A.Fisher, K. Kusche, R. Malone, I.Pogorelsky, J. Qiu, T. Romano, J.Sheehan, J.Skaritka, T. Srinivasan-Rao and X-J Wang.

This work was supported by the Advanced Technology R&D Branch, Division of High Energy Physics, U.S.Department of Energy, DE-AC02-76CH00016.

### References

[1] R. Palmer, J. Appl. Phys. 43, 3014 ,1972.
[2] C. Pellegrini, P. Sprangle,W. Zakowicz, Proc. of the XIIInt.Conf. on High EnergyAccelerators, p.473 ,1983.
[3] E. Courant,C. Pellegrini,W. Zakowicz, PR A32, 2813,1985.
[4] A. Fisher, J. Gallardo, J. Sandweiss, A.van Steenbergen, "Inverse Free Electron Laser Accelerator", Proc. Adv. Accel. Concepts, Port Jefferson, NY, AIP 279, p.299 ,1993.
[5] A. Fisher, J. Gallardo, A. van Steenbergen, J. Sandweiss, "IFEL Accelerator Development", Nucl. Instr. Meth.A341,1994
[6] I. Wernick and T. C. Marshall, Phys. Rev. A46, 3566 ,1992.
[7]A.vanSteenbergen,J.Gallardo,J.Sandweiss,J.Fang,M.Babzien, K.Batchelor,A.Fisher,K.Kusche,R.Malone,I.Pogorelsky,J.Qiu, T.Romano, J.Sheehan, J.Skaritka, T.Srinivasan-Rao, XJWang, "Inverse Free Electron Laser Single Module e⁻ Acceleration", Proceedings BNL CAP/ATF Users Meeting, Dec., 1995
[8]A.van Steenbergen,Pat.Appl.368618,June 1989 (Aug.'90)
[9] A. van Steenbergen, J. Gallardo, T. Romano, M. Woodle, "Fast Excitation Wiggler",Proc.PAC SF.,IEEE NS, May 1991
[10]A.Fisher,J.Gallardo,A.van Steenbergen,J.Sandweiss,J.Fang, "IFEL Development",VI Workshop Adv. Accel.,Fontana,WI '94
[11] J. Harrington, C. Gregory, Optics Letters 15, (1990)
[12] N.Kroll, P.Morton, M.Rosenbluth,Physics of QE 7,89,1979
[13] I. Ben-Zvi, Proc. Adv. Accel. Concepts, Port Jefferson, NY, AIP 279, 590 (1993)
[14] I. Pogorelsky, Proc. Adv. Accel. Concepts, Port Jefferson, NY, AIP 279 608 (1993)

# 付録-8
# Compendium of Scientific Linacs

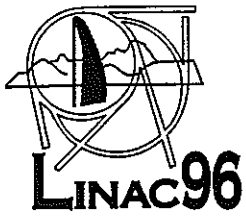


XVIII International Linac Conference
Geneva, Switzerland
26-30 August, 1996

CERN/PS 96-32 (DI)

# Compendium of Scientific Linacs

J. Clendenin*, L. Rinolfi, K. Takata**, D.J. Warner

*SLAC, Stanford, USA
**KEK, Tsukuba, Japan

CERN – PS Division
European Organization for Nuclear Research
Switzerland
November 1996

## Table of Contents

### AMERICA, NORTH AND SOUTH

| LOCATION | INSTITUTION | LINACS | FUNCTION | Page |
|---|---|---|---|---|
| NEW YORK | | | | |
| Ithaca | Cornell University | e- /e+: 350/200 MeV | CESR Injector | 50/51 |
| Stony Brook | University of New York | ions : 12 MeV/u | Atomic physics | 52 |
| Troy | RPI | e- : 90 MeV | Research experiments | 53 |
| Upton | BNL | e- : 120 MeV | NSLS injector | 54 |
| | | e- : 70 MeV (ATF) | Accelerator physics | 55 |
| | | H- : 200 MeV | AGS injector | 56 |
| NORTH CAROLINA | | | | |
| Durham | Duke University | e- : 295 MeV | Injector of storage ring | 57 |
| | | e- : 45 MeV | MKIII FEL Injector | 58 |
| TENNESSEE | | | | |
| Oak Ridge | ORNL | e- : 178 MeV (ORELA) | Nuclear physics | 59 |
| VIRGINIA | | | | |
| Newport News | CEBAF | e- : 4 GeV | Nuclear physics | 60 |
| WASHINGTON | | | | |
| Seattle | Boeing | e- : 100 MeV | FEL | 61 |
| | | e- : 25 MeV | Injector for 100 MeV linac | 62 |
| | University of Washington | ions : 15 MeV/u | Post accelerator | 63 |

## ASIA

| LOCATION | INSTITUTION | LINACS | FUNCTION | Page |
|---|---|---|---|---|
| CHINA | | | | |
| Beijing | IHEP | e-/e+ : 1.8/1.6 GeV | Injector for BEPC | 67/68 |
| | | e- : 30 MeV | FEL Driver | 69 |
| | | p : 35 MeV | Proton beam application | 70 |
| Hefei | HLS | e- : 225 MeV | Injector for Light Source | 71 |
| JAPAN | | | | |
| Hirakata, Osaka | FELI | e- : 165 MeV | FEL | 72 |
| Ibaraki, Osaka | ISIR, Osaka University | e- : 150 MeV (S-Band) | Scientific research | 73 |
| | | e- : 38 MeV (L-Band) | Scientific research | 74 |
| Inage-ku,Chiba | NIRS | ions : 6 MeV/u | Injector for HIMAC | 75 |
| Kamigori, Hyogo | SPring-8 | e-/e+: 1.15/0.9 GeV | Injector for SPring-8 | 76/77 |
| | Sumitomo Electric | e- : 120 MeV | Injector for NIJI-III and FEL | 78 |
| Kita-ku, Sapporo | Hokkaido University | e- : 45 MeV | Atomic Science | 79 |
| Oarai-Machi, Ibaraki | PNC-OEC | e- : 10 MeV | Transmutation | 80 |
| Sennan-gun, Osaka | KURRI, Kyoto University | e- : 46 MeV | Neutron source, X-ray, e+ prod. | 81 |
| Taihaku-ku, Sendai | Tohoku University | e- : 300 MeV | Nuclear physics | 82 |
| Tanashi, Tokyo | INS, University of Tokyo | e- : 15 MeV | Injector for INS synchrotron | 83 |
| | | ions: 1 MeV/u | ISOL post accelerator | 84 |
| Tokai, Ibaraki | JAERI | e- : 23 MeV (SCARLET) | FEL | 85 |
| | | p : 2 MeV RFQ | Beam test | 86 |
| | | ions : 30 MeV/u | Booster linac | 87 |
| | NERL, University of Tokyo | e- : 35 MeV | Radiation Physics | 88 |
| Tokyo | RLNR | ions : 3.4 MeV/u (TIT-IH-2) | Booster Linac Heavy Ion Acc. | 89 |
| | | ions : 2.4 MeV/u (TIT-IH) | Main Linac Heavy Ion Acc. | 90 |
| | | ions : 1.7 MeV/u (Deuteron IH Linac) | Radio-isotope Prod. for PET | 91 |
| | | ions : 0.22 MeV/u (TIT-RFQ) | Plasma experiment | 92 |
| Tsukuba, Ibaraki | KEK | e-/e+ : 3 GeV | Injector for PF and TRISTAN | 93/94 |
| | | e- : 2 GeV | Inj. linac for ATF Damping Ring | 95 |
| | | p : 40 MeV | Injector for synchrotron | 96 |
| | | H- : 5 MeV | Test facility for JHP | 97 |
| | ETL | e- : 0.5 GeV (TELL) | Injector for 3 SR rings | 98 |
| Uji, Kyoto | ICR, Kyoto University | e- : 100 MeV | Injector for KSR | 99 |
| | | p : 7 MeV | Accel. development | 100 |
| Wako, Saitama | IPCR (RIKEN) | ions : 3 MeV/u (RILAC) | Basic research | 101 |
| KOREA | | | | |
| Pohang | PAL (POSTECH) | e- : 2.0 GeV | Injector PLS | 102 |
| TAIWAN | | | | |
| Hsinchu | SRRC | e- : 50 MeV | Injector for 1.3 GeV storage ring | 103 |

## EUROPE

| LOCATION | INSTITUTION | LINACS | FUNCTION | Page |
|---|---|---|---|---|
| **ARMENIA** | | | | |
| Yerevan | Physics Institute | e- : 10 GeV (U-006) | Applied Research | 107 |
| | | e- : 0.120 GeV | High-current inj. for YerPHI Syn. | 108 |
| | | e- : 0.075 GeV | Injector for YerPHI Synchrotron | 109 |
| | | e- : 0.008 GeV (LAE-8) | Irr. of material + rad. techn. | 110 |
| | | e- : 0.005 GeV (U-003) | Applied Research | 111 |
| | | e- : 0.004 GeV (LAE-4) | Irr. of material + sterilization | 112 |
| **BELGIUM** | | | | |
| Geel | IRMM | e- : 200 MeV (GELINA) | Neutron and radiation physics | 113 |
| Gent | Gent University | e- : 15 MeV | Interdisciplinary research | 114 |
| **FRANCE** | | | | |
| Le Barp | CEA-CESTA | e- : 8 MeV (PIVAIR) | X-ray radiography | 115 |
| | | e- : 3 MeV (LELIA) | FEL | 116 |
| Bruyères-le-Châtel | CEA | e- : 20 MeV (ELSA) | FEL, R&D | 117 |
| Grenoble | ESRF | e- : 200 MeV | Injector for Synch. Rad. Fac. | 118 |
| Orsay | CNRS-LURE | e- : 2.3 GeV | Physics experiments | 119 |
| | | e-/e+ : 1 /1.4 GeV | Injector for Super-ACO | 120/121 |
| | | e-/e+ : 340/350 MeV (EPLUS) | Injector for SOLEIL | 122/123 |
| | | e- :100 MeV (ELIOS) | Injector for SOLEIL | 124 |
| | | e- : 70 MeV (FEL-CLIO) | Injector for FEL | 125 |
| | LAL | e- : 100 MeV (NEPAL) | High gradient accelerators | 126 |
| | | e- : 3 MeV (CANDELA) | Test facility for linear collider | 127 |
| Saclay | CEA | e- : 20 MeV (MACSE) | Test facility for SC linacs | 128 |
| **GERMANY** | | | | |
| Berlin | HMI | e- : 15 MeV | Radiography | 129 |
| | | ions : 0.36 MeV/u (RQ13) | Ion injector | 130 |
| Bonn | Bonn University | e- : 20 MeV (Linac I) | Injector for ELSA booster | 131 |
| | | e- : 30 MeV (Linac II) | Injector for ELSA booster | 132 |
| Darmstadt | GSI | ions : 1.4 MeV/u (Linac I) | Heavy ion injector for UNILAC | 133 |
| | | ions : 1.4 MeV/u (Linac II) | Heavy ion injector for UNILAC | 134 |
| | | ions : 15 MeV/u (Linac III) | Synchr. injector, physics exp. | 135 |
| | IKP | e- : 130 MeV (S-DALINAC) | Nuclear physics + FEL driver | 136 |
| Dortmund | University of Dortmund | e- : 100 MeV (DELTA) | Inj. for 1.5 GeV SR | 137 |
| Hamburg | DESY | e-/e+ : 900/550 MeV (LINAC II) | Injector for PIA | 138/139 |
| | | e- : 600 MeV (TTF) | Test facility for linear collider | 140 |
| | | e- : 450 MeV (SBTF) | Test facility for linear collider | 141 |
| | | H- : 50 MeV (LINAC III) | Injector for DESY III | 142 |
| Heidelberg | Max Planck Institüt | ions : 13 MeV/u | Atomic physics | 143 |
| | | ions : 2 MeV/u | Atomic physics | 144 |
| Mainz | Kernphysik Institüt | e- : 3.5 MeV | Injector for RTM (MAMI) | 145 |
| Munich | Technical University | ions : 6 MeV/u | Post-accelerator | 146 |
| **ITALY** | | | | |
| Frascati | INFN-LNF | e-/ e+ : 800/550 MeV | Injector for Dafne | 147/148 |
| Legnaro | INFN | ions : 20 MeV/u (ALPI) | Heavy ion linac | 149 |
| Trieste | Sincrotrone Trieste | e- : 0.1 GeV (ELETTRA) | Preinjector | 150 |
| | | e- : 1.2 GeV (ELETTRA) | Injector for ELETTRA | 151 |
| **NETHERLANDS** | | | | |
| Amsterdam | NIKHEF | e- : 800 MeV (MEA) | Injector for AmPS | 152 |
| Nieuwegein | FOM | e- : 45 MeV (FELIX) | FEL | 153 |
| Twente | Twente University | e- : 7 MeV (TEUFEL) | FEL | 154 |
| **POLAND** | | | | |
| Swierk | Soltan Inst. Nucl. Studies | e- : 22 MeV (S-20) | Accelerator technology | 155 |

# ELECTRON LINAC

Name of Linac : *PNC Linac*
Function : *Electron Linac for Transmutation*
Institution and address : *PNC-OEC * 4002 Oarai-machi, Ibaraki-ken 311-13, Japan*
Person in charge : *Takashi Emoto*
Name of person supplying these data : *Takashi Emoto*
e-mail : *emoto@oec.pnc.go.jp*
tel. : *+81 29 267 4141 ext.3130* fax : *+81 29 266 3868*

## HISTORY AND STATUS

Const. started : *1994* ; first beam : *1996*
Present status : *Under the commissioning*
Cost of facility : *5000 MJPY*
Present linac staff : *17 man-years*
Present yearly operation time : *NA* h

## LINAC PARAMETERS

### Electron Sources

Types : *Triode* ; energy : *200* keV
Beam intensity (peak) : *0.400* A
Normalized emittance (1σ) : *NA* π mm-mrad

### Injector

Longitudinal matching : *(1)*
Output : *2.0* MeV; intensity : *0.100* A
Pulse width, spacing : *4 ms, 16 ms*
Normalized emittance (1σ) : *NA* π mm-mrad

### Acceleration System

Total linac length : *18* m
No. sections : *8* ; lengths : *1.2* m
Field mode : *2π/3* ; frequency : *(2)* GHz
Wave type : *TW* ; filling time : *(3) 13* μs
$v_g/c$ range : *(4)* ; Q : *(5)*
Shunt impedance : *16.2 - 39.1* MΩ/m
Iris : aperture : diameter : *24.5 - 32.4* mm
thickness : *12* mm
Attenuation/section : *0.04076 - 0.06082* Np
Power units, Number : *2* type : *Klystron*
RF power peak : *1.2* MW; mean : *(6) 240* kW

### Focusing System

Type, No. of elements, and spacing :
*Solenoids up to 3.5MeV; a doublet at 3.5MeV and between sections to 10 MeV; a triplet at 10 MeV*

### Beam Pulse Structure (if applicable)

No. of bunches/pulse : *NA*
No. of particles/bunch : *NA*
Bunch separation : *NA*

## LINAC PERFORMANCE

| | | Normal Operation | Max, or Design | |
|---|---|---|---|---|
| Final energy | : | *0.01* | *NA* | GeV |
| Accel gradient | : | *1.0 - 1.4* | *NA* | MeV/m |
| ΔE/E (FWHM) | : | *0.2* | *NA* | % |
| Rep. rate | : | *0 - 50* | *NA* | Hz |
| Pulse length | : | *10 - 4000* | *NA* | μs |
| Beam intensity | : | *0.100* | *NA* | A |
| Norm. emit. (1σ) | : | *N/A* | *NA* | π mm-mrad |

## OTHER RELEVANT INFORMATION

* *Power Reactor & Nuclear Fuel Development Co. Oarai Engineering Centre*

*(1) L-band pre-buncher and buncher*
*(2) 1.249135*
*(3) Resonant Ring filling time*
*(4) 0.011-0.025*
*(5) 20130-15392*
*(6) 1.2MW klystron only*

# 付録-9
# A Brief Overview of PSI

# A Brief Overview of PSI

PAUL SCHERRER INSTITUT

The Paul Scherrer Institute (PSI) is a multi-disciplinary research centre for natural sciences and technology. In national and international collaboration with universities, other research institutes and industry, PSI is active in elementary particle physics, life sciences, solid state physics, materials sciences, nuclear and non-nuclear energy research, and energy-related ecology.

The institute's priorities lie in areas of basic and applied research, particularly in fields which are relevant for sustainable development, as well as of major importance for teaching and training, but which are beyond the possibilities of a single university department. PSI develops and operates complex research installations which call for especially high levels of know-how, experience and professionalism, and is one of the world's leading user laboratories for the national and international scientific community. Through its research, PSI acquires new basic knowledge and actively pursues its application in industry.

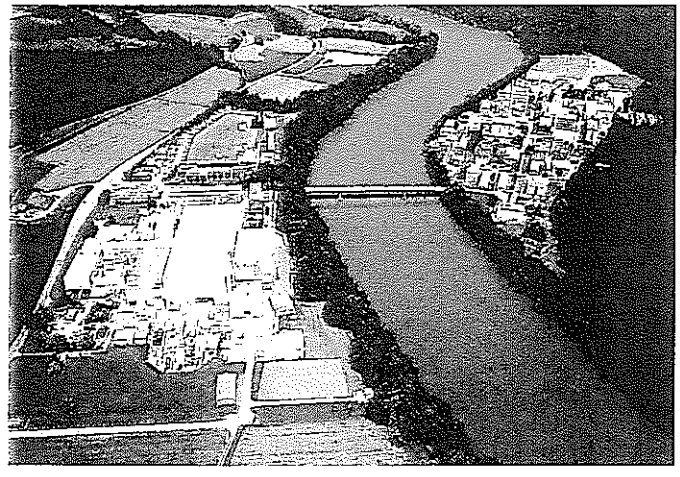

PAUL SCHERRER INSTITUT

Paul Scherrer Institut
CH-5232 Villigen PSI
Switzerland

Phone 056 310 21 11
Fax 056 310 21 99
http://www.psi.ch

## The Paul Scherrer Institute

# PSI's Guiding Principles

With a staff of 1200 and an annual budget of close to 160 million Swiss Francs, PSI is the largest national research institute in Switzerland. Its research is aimed at today's global challenges, oriented towards future needs of science and embedded in the international research community. PSI is affiliated to the Board of the Swiss Federal Institutes of Technology and, as such, contributes to basic scientific research and promotes new technologies for Swiss industry while supporting sustainable development.

## Guiding Principles

- Scientific excellence, promotion of interdisciplinary research, «market» orientation, development of leadership
- User Laboratory: design, construction and operation of large, complex research facilities for the national and international scientific community
- Contribution to education and training in close collaboration with universities
- Transfer of research results for application to new products and processes in partnership with industry
- Relevance to society
- Self-criticism, open-mindedness and accountability

# A changing PSI

PSI's research programme is being continually adapted to match the current state of scientific knowledge. Over the last few years, emphasis has shifted from the earlier priorities of **particle physics** and **nuclear-energy research** towards **solid state physics and materials sciences** as well as **general energy research and environmental sciences.** These developments are reflected in the distribution of government funding for personnel. The new Neutron Spallation Source, SINQ, and the planned Swiss Light Source, SLS, are initiating a strong shift of our research focus towards the study of the structure of materials.

## Development 1980 – 2000

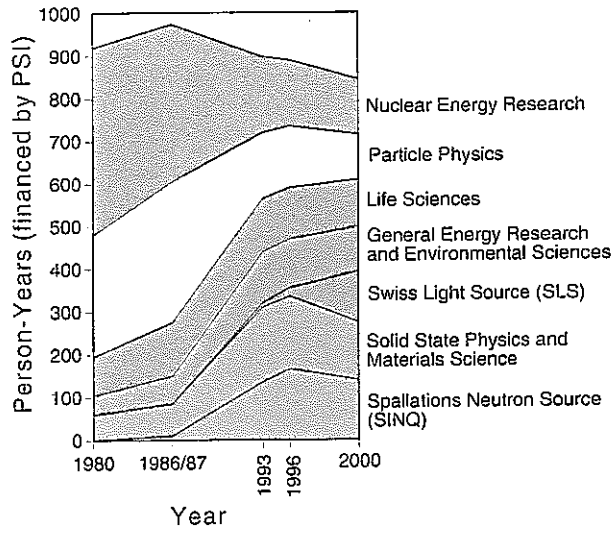

# Research at PSI

# Material Structure Studies at PSI

**Focal Points:**

## Nuclear Energy Research
- Research and scientific services in the area of reactor safety
- Safety studies on the disposal of radioactive wastes

## Particle Physics
- Study of fundamental interactions of matter
- Search for rare decays of elementary particles

## Life Sciences
- Cancer therapy and medical diagnosis using particle beams
- Effects of radiation on living organisms

## General Energy Research
- New methods for energy storage and energy use
- Environmentally oriented analysis of energy systems

## Solid State Physics and Materials Sciences
- Investigation of the atomic structures of solid matter and liquids by means of particle beams
- Analysis and production of minute structures, on the micrometer and nanometer scale

PSI is becoming a centre for the structural analysis of matter. New basic knowledge is being gained and new technologies developed through the application of different kinds of particle beams in life sciences, chemistry, materials sciences and physics. To this end, PSI is continuously upgrading its large and complex research facilties in order to match the needs of science.

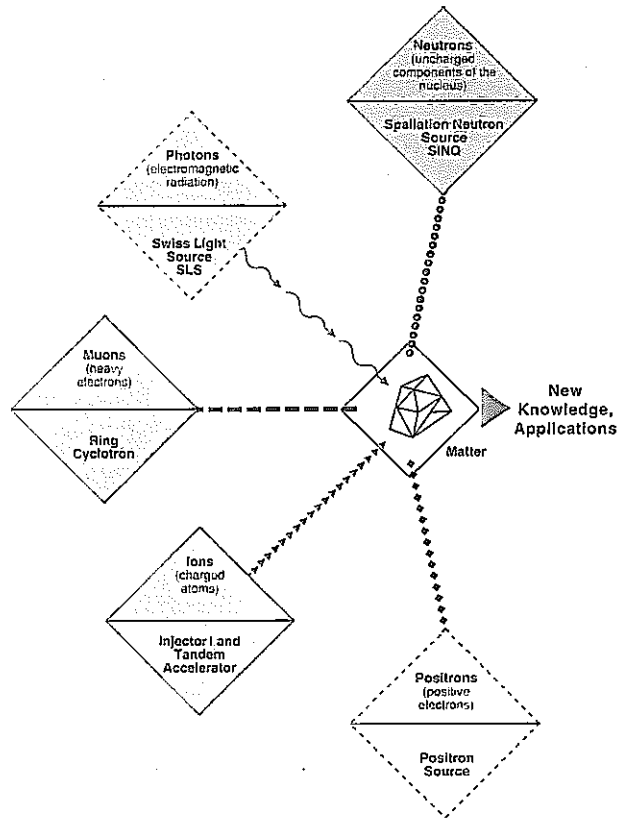

# PSI's Strength: Interdisciplinary Research with Large Facilities

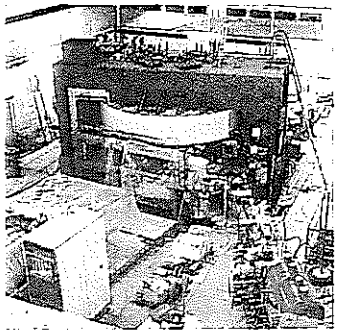

Injector I

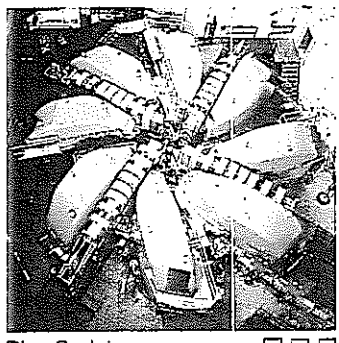

Ring Cyclotron

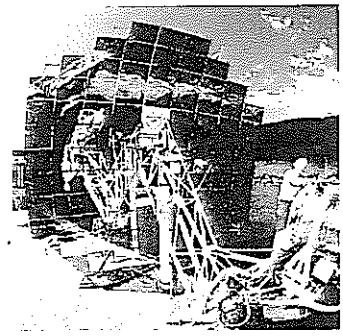

Parabolic Solar Mirror

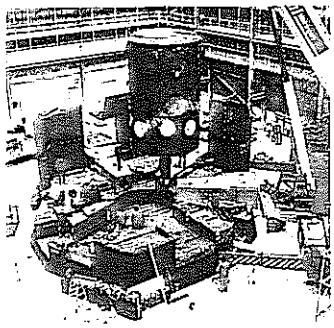

SINQ

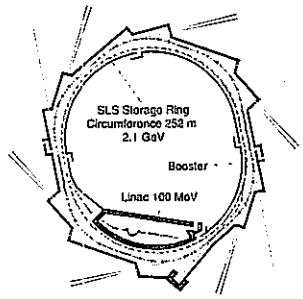


SLS

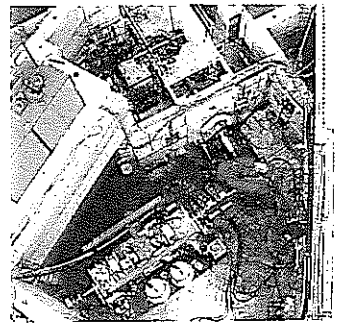

Muon Spin Rotation

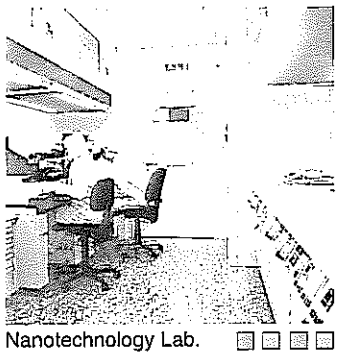

Nanotechnology Lab.

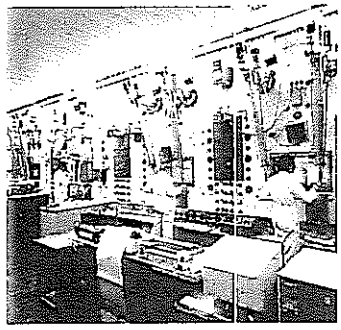

Hot Laboratory

- Particle Physics
- Biology / Medicine
- Solid State Physics and Materials Sciences
- Energy Research
- Chemistry

# 付録-10
# Beam Dump for High Power Electron Beam at PNC

Title "Beam Dump for High Power Electron Beam at PNC"

(1) Introduction

- (a) PNC加速器
- (b) Beam Dump

(2) Design

- (a) Concept
- (b) 全体形状
- (c) ディスク形状
- (d) EGS4の説明
- (e) Energy Deposition
- (f) Cooling Channel
- (g) モジュール化
- (h) 真空度
- (i) 遮蔽

(3) Thermal and Stress Analysis

- (a) 温度分布
- (b) 応力分布

(4) Test Run

- (a) 温度上昇
- (b) 真空度
- (c) 電流測定結果

(5) Conclusion

(6) Appendix

# 付録-11
# 中空円板の弾塑性変形に関する解析例

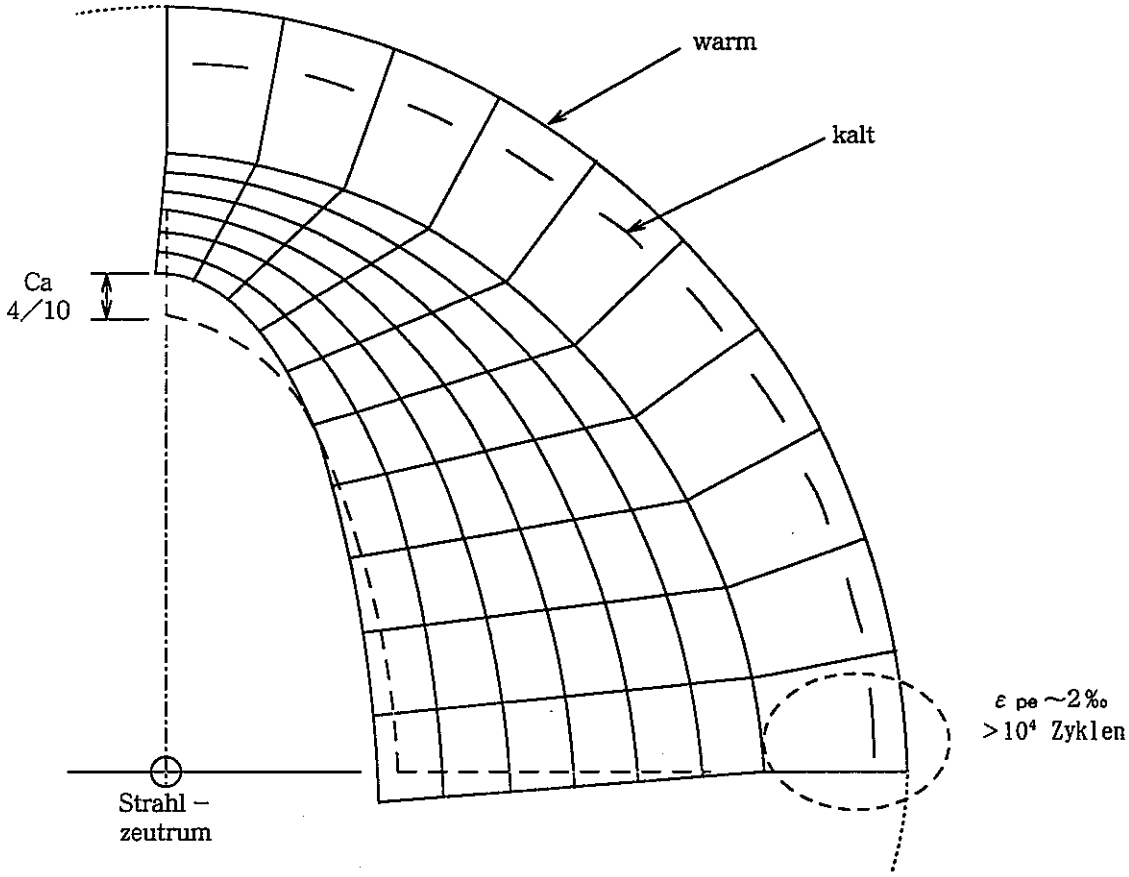


Displacements Kollimator 2

付録-12

# Research and development for molten heavy metal targets The European Spallation source Study, ESS

# Research and Development for Molten Heavy Metal Targets

**G.S. Bauer**

*Paul Scherrer Institut,*
*CH-5232 Villigen-PSI, Switzerland*

Paper prepared for

*Second International Conference on Accelerator Driven Transmutation Technologies and Applications*
**3-7 June 1996, Kalmar, Sweden**

H:\bq30\P9605.DOC

# Research and Development for Molten Heavy Metal Targets

G.S. Bauer
*Paul Scherrer Institut, CH-5232 Villigen-PSI, Switzerland*

**Abstract.** Spallation facilities of the future will, to a large extent, have to rely on molten heavy metal targets to be able to remove the heat from the reaction zone and to avoid excessive radiation damage in the target material. This, however, results in rather stringent requirements on the safety and durability of the proton beam window and of the walls of the liquid metal system. Effects to be considered in detail in this context are high gas production rates in both the solid window and the liquid target itself, transmutation and fission products and their effects on the solid material as well as on the corrosive and physical properties of the liquid metal. In this context it is not only important to understand the direct effects on the wall material, which are so far largely unexplored, but also the chemistry going on in the liquid metal between the various species present after prolonged operation. Destruction and formation of surface-coating layers, liquid metal-solid metal reactions and the effects of stress and irradiation on these processes must be investigated in detail in addition to such fundamental questions like flow configurations, the effect of buoyancy, heat transfer coefficients and the influence of gases in the liquid. A joint effort has been launched between various laboratories interested in the development of next generation neutron sources in which existing and available installations world wide shall be utilised to the largest possible extent in order to optimise the return for the resources used in a co-ordinated research and development effort.

## INTRODUCTION

In many accelerator driven neutron sources use of molten heavy metals as target materials is considered the most efficient way to obtain a high flux of fast neutrons and to remove efficiently the heat generated in the reaction zone. This is true for large future installations designed to advance present day nuclear technology towards more fuel-efficient systems and burning what is presently considered as problematic waste, as well as for medium power-high flux neutron research sources which hold a strong promise to extend and broaden the use of cold, thermal and epithermal neutrons in a variety of fields in fundamental and applied research [1]. As with high performance research reactors of the past, the requirements tend to be more stringent with the research neutron sources than with their industrial counterparts, but the basic problems to be solved remain the same. Presently, use of liquid metal targets is seriously contemplated for three research neutron sources under study or under construction: the Swiss SINQ-project [2], which is due to be commissioned early 1997, albeit still with a solid target, the 1 MW pulsed neutron source under study at Oak Ridge National Laboratory [3] and the European Spallation Source Project (ESS) [4], which is being designed for 5 MW of beam power. It is in the context of these plans that the needs and opportunities for research and development were analysed recently in a series of workshops [5], [6]. The present paper focuses mostly on the results of these workshops and on steps taken in the mean time towards realising a corresponding research programme.

## EXISTING EXPERIENCE WITH SPALLATION TARGETS

Although spallation neutron sources have now a cumulative operating time of almost 60 years (Table 1), available target experience is very limited in terms of accumulated proton dose, because all of the existing sources are of comparatively low power. Furthermore, since

metallic Uranium was used in the more powerful ones of them, data are by no means encouraging, as is obvious from Table 2.

Table 1 *Existing experience with spallation neutron sources*

| Facility | Beam power | Target | Operational since |
|---|---|---|---|
| KENS (Japan) | 3 kW | 238-U, Zy-clad | 1980 |
| IPNS (Argonne, USA) | 7 kW | 238-U, Zy-clad | 1981 |
| | | 235-U, Zy-clad | 1988 |
| LANSCE (Los Alamos, USA) | 60 kW | W, unclad | 1977 |
| TRIUMF (Vancouver, Canada) | 50 kW | Pb in SS | 1978 |
| ISIS (Rutherford Lab, UK) | 160 kW | 238-U, Zy-clad | 1985 |
| | | Ta, unclad | |

Table 2 *ISIS and IPNS target load data [7], [8]. Thermal cycles to failure and total protons to failure and approximate peak temperature Note: 1750 mAh at ISIS corresponds to 280 MWh*

| Target | Thermal Cycles* | Total Protons(mAh) | Peak Temperature (°C) | |
|---|---|---|---|---|
| ISIS depl.U #1 | | 92 | | |
| ISIS depl.U #2 | 40000 | 53 | 120 | |
| ISIS depl.U #3 | 10389 | 175 | 130 | |
| ISIS depl.U #4 | 4147 | 139 | 150 | |
| ISIS depl.U #5 | 5074 | 296 | 165 | |
| ISIS depl.U #6 | 2628 | 126 | 180 | |
| ISIS depl.U #7 | 1085 | 107 | 216 | |
| IPNS depl.U #1 | 89600 | 240 | 225 | |
| IPNS enr. U #1 | 28000 | 121 | 175 | |
| ISIS Tantalum #1 | 3375 | 1750 | 320 | (at e.o.l) |
| ISIS Tantalum #2 ** | 32630 | 1006 | 180 | (at b.o.l) |

* thermal cycling due to accelerator trips ** Target still in use

The Uranium targets at both, IPNS and ISIS were Zircaloy clad disks of metallic Uranium and their appearance after failure (cracks in the Uranium and in the cladding and significant deformations on the surface) was practically identical. Although no clear correlation can be found between thermal cycles (due to accelerator trips) or the number of protons, the life time of Uranium targets in higher power sources would clearly be unacceptably short. The ISIS-Tantalum target #1 did not actually fail, but the time to cool down after the beam was turned off became increasingly longer and the centreline temperature had risen from 180°C to 320°C, indicating severe degradation of the thermal conductivity of the material.

The Tungsten target used at LANSCE (Tab. 1) has been exposed to about $10^{21}$ protons/cm$^2$. At this point it was taken out of service because of corrosion products found in the cooling circuit. It was therefore made a design rule that Tungsten alloy should not be used in direct contact with cooling water in future targets at LANSCE [9]. Also, inspection of the target after it had been taken out of sevice showed that it had probably become too hot where it had been hit by the beam, inducating that the thermal properties of the material had degraded during irradiation.

The ISIS-Tantalum target #1 has been shipped to KFA Jülich for investigation under the current R&D-program. The Inconel window of this target and a test window from ferritic-martensitic steel for the SINQ-target irradiated at Los Alamos will also be examined. Experience with Los Alamos beam windows indicates that Inconel 718 can perform to a dose of at least $7x10^{21}$ protons/cm$^2$ [10]. This corresponds to about 1600 hours at ESS-parameters (85 A/cm$^2$), assuming no effects from being in contact with liquid metal (see below) but allowing for an effect of fast neutron flux similar to that of the protons.

## EXPECTED BENEFITS FROM USING MOLTEN HEAVY METAL TARGETS

Apart from the most significant feature of not being sensitive to structural radiation damage in the target material itself, liquid metal targets offer several other potential advantages:

- Heat removal occurs by convection which makes it unnecessary to subdivide the target into slabs or rods sufficiently thin to allow transport of the heat to the surface without generating excessive centreline temperatures or dangerously high surface heat loads that might impede efficient heat transfer and eventually lead to damage or destruction of the target.
- The pressure in the coolant (liquid metal) system can generally be kept lower than for water cooling systems, thus reducing the mechanical load on the beam window.
- Radiolysis and associated corrosion effects in the water cooling system can largely be avoided, eliminating the associated cleaning and recombination equipment.
- Water is not directly exposed to high energy radiation, avoiding the generation of $^7$Be from spallation of oxygen, which tends to plate out on all walls of the cooling circuit and has an unpleasant half life of 53.3 days.
- Due to the generally very large total target mass relative to the mass exposed to the proton beam at any time, the specific radioactivity and afterheat generation of the target are very low and no active emergency cooling system is required after the beam is shut off.

Candidate materials for liquid metal targets and their relevant properties are listed in Table 3.

Table 3. *Candidate materials for liquid metal targets and their relevant properties*

| Property | Pb | Bi | LME | LBE | Hg |
|---|---|---|---|---|---|
| Composition | elem. | elem. | Pb97,5% Mg2.5% | Pb45% Bi55% | elem. |
| Atomic number, Z | 82 | 83 | "82" | "82.5" | 80 |
| Atomic mass A (g/mole) | 207.2 | 209 | 202.6 | 208.2 | 200.6 |
| Density (g/cm$^3$) solid (20°C) | 11.35 | 9.75 | | (10.5) | - |
| liquid | 10.7 | 10.07 | 10.6 | 10.5 | 13.55 |
| Coefficient of thermal expansion ($10^{-5}$ K$^{-1}$) | 2.91 | 1.75 | | | 6.1 |
| Contraction upon solidification (%) | 3.32 | -3.35 | 3.3 | 0 | - |
| Melting point (°C) | 327.5 | 271,3 | 250 | 125 | -38.87 |
| Boiling point at 1 atm (°C) | 1740 | 1560 | | | 356.58 |
| Specific heat capacity (J/gK) | 0.14 | 0.15 | 0.15 | 0.15 | 0.12 |
| Thermal neutron absorption (barn) | 0.17 | 0.034 | 0.17 | 0.11 | 389 |

From its low melting point and high density, Mercury is a good candidate because there is no risk of freezing when the beam goes off and the operating temperature can be kept in a regime where heat transfer with conventional heat exchangers is not a problem. Furthermore, in contrast to Pb and Bi, no alpha-active spallation products are generated in Mercury. On the other hand, the large thermal neutron absorption cross section makes Mercury suitable only for fast neutron systems in which the generation of a high thermal neutron flux through long lifetime of the neutrons in the moderator is not a goal. PbBi-eutectic also has a reasonably low melting point but, in particular in a thermal neutron environment, alpha-active $^{210}$Po is generated and adds considerably to the radiotoxicity of the system. Adding 2.5% of Magnesium to lead also reduces the melting point significantly, but, since Mg is known to be a strong oxygen getter, the chemistry of such a system would have to be investigated carefully (see below).

## RADIATION EFFECTS IN THE TARGET CONTAINER MATERIAL

An evaluation carried out at the workshop in Oak Ridge [11] showed that for liquid metal targets operating at relatively low temperatures (mercury) and at pressure levels in the container not exceeding 200 MPa, austenitic stainless steel is the presently best known candidate material. For systems working at higher pressure levels or containing Bi, Nickel-free ferritic-martensitic steels are considered superior, because of their better corrosion resistance towards liquid metals and because their recommended design stress in the unirradiated condition is higher [12].

Although a vast amount of literature exists on the effects of irradiation on steels related to their use in fission and fusion devices, the pertinent knowledge for the specific situation in a spallation target is extremely limited and the effect on the mechanical properties of the structure materials when irradiated with a spallation-typical spectrum at the temperature and stress range in question is virtually unknown [13], [14]. The main uncertainty results from the high Helium and Hydrogen production rate relative to the displacement damage and the effect those high simultaneous production rates might have. For example, it was pointed out [15] that Hydrogen might be trapped in very small Helium bubbles rather than escaping from the material as is usually assumed in non-hydride forming materials. It is, therefore, crucial for any spallation materials development program to have available facilities which allow to do relevant experiments under controlled conditions.

At present, simulations can be performed on the dual and triple beam irradiation facilities at HMI, Berlin [16] and at ORNL, Oak Ridge [17]. These experiments are limited to very thin layers near the surface of the specimens, however and do not necessarily reproduce correctly the spatial correlation between displacement damage and gas generation in the situation where the generation of the gas ion itself is correlated with the generation of a damage cascade in the host material. A more realistic picture is expected to result from a series of irradiations currently under preparation at LANSCE in Los Alamos by an international research team [18]. Irradiations are due to start in autumn 1996 and to continue through autumn 1997.

An irradiation program is also being planned for the SINQ-spallation source in Switzerland, which is expected to be commissioned in spring 1997. The target development program for this source includes a solid, heavy water cooled rod target in the beginning which will eventually be replaced by a liquid metal target later. The basic concept of the two targets is shown in Fig. 1. The beam is injected from underneath into these targets.

The opportunity will be provided to remove individual rods from the target after the end of its usage and to examine them. This can be done on full size rods or on specially designed

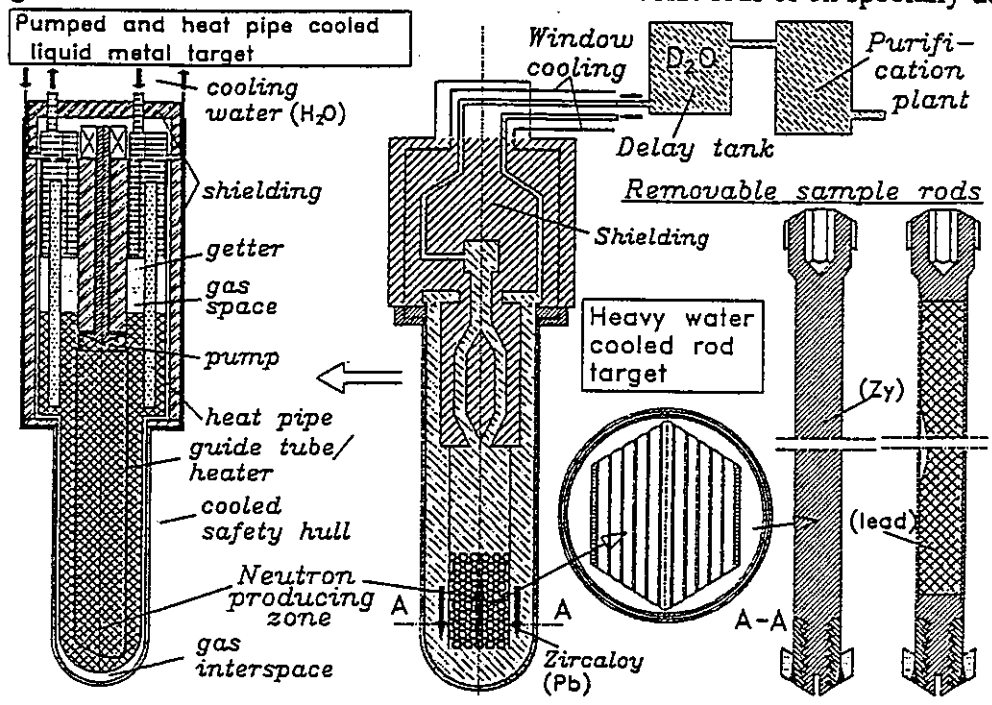


Figure 1. *Schematic representation of the solid and liquid metal targets foreseen for use in the SINQ-facility.*

irradiation capsules. Due to the rather severe level of radioactivity examination of full size rods (11 mm diameter) is likely to be limited to non-destructive methods that can be applied behind heavy shielding. One such class of investigations use neutrons as a highly penetrating probe. At present planning for several of the neutron instruments on SINQ provides for suitably shielded sample environment. The features to be investigated and the type of instruments foreseen are:

| | |
|---|---|
| Microstructural evolution and precipitates | Small angle neutron scattering |
| Hydrogen distribution | Transmission neutron radiography<br>Prompt gamma activation analysis |
| Internal stresses, phase separations | High resolution neutron diffraction |

Specially designed irradiation capsules have been proposed at the Oak Ridge workshop [6] to contain miniature tensile test specimens, miniature fatigue specimens and TEM-disks, together with a dosimetry package and a thermocouple, as sketched in Fig. 2. The program will be a joint effort between PSI (Switzerland), ORNL (USA), KFA Jülich (Germany), and LANL (USA) and interest in participation has also been expressed by CEREM (France). Preparations to include such specimens in the second target to be used in SINQ are now in progress. Testing of the irradiated specimens is foreseen to be done at the PSI and KFA hot cells.

At PSI, a proton irradiation facility, PIREX, has been in operation for several years [19], which is used for investigations in the European fusion program. In the framework of this program work is being performed on so called "low activation steels" which turn out to have

a lower ductile-to brittle transition temperature than HT-9 type ferritic/martensitic steels and do not contain Nickel at all. The increase of the ductile-to brittle transition temperature observed in HT-9 type steels at irradiation temperatures below 300°C seems to be much less severe in these new materials [20], which makes them of great interest in systems using Mercury or PbBi as target materials, where the window temperature is expected to be less than 300°C, but where the nickel contained in austenitic steels must be considered problematic because of potential corrosive attack by the Mercury. These materials will therefore be investigated in a co-operative program.

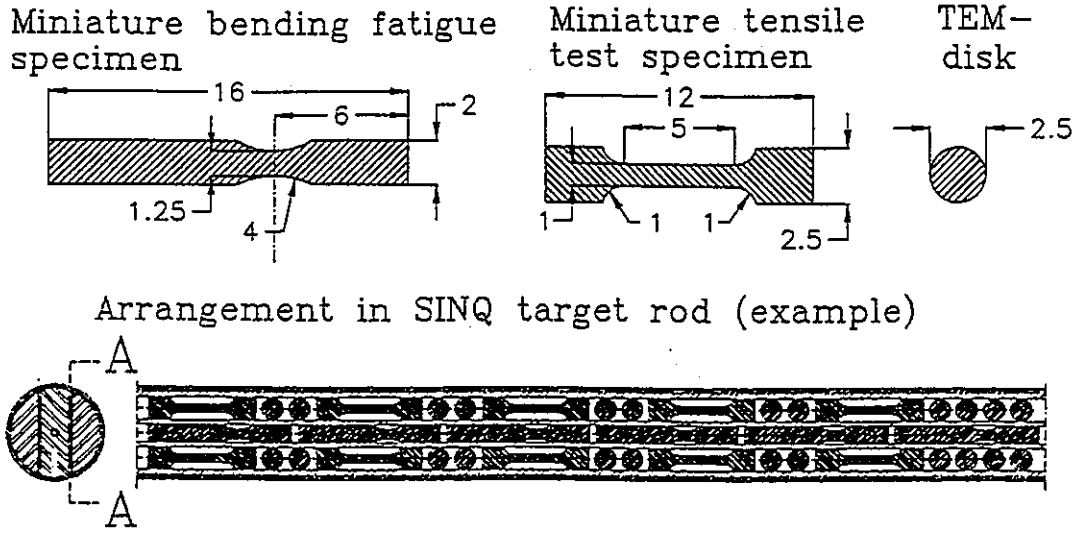


Figure 2. *Test specimens foreseen for irradiation in the SINQ-target*

## LIQUID METAL CHEMISTRY AND LIQUID METAL-WALL INTERACTION

As a consequence of the spallation process and of concurring fast fission in the target material significant amounts of elements throughout the periodic system with mass numbers lower than that of the target nuclei will be generated. Figure 3 shows the calculated distribution of the elements generated in a Mercury target (which, apart from the immediate neighbourhood of the parent element) is almost the same also for Pb and PbBi. Because the total target mass involved is very high (about 20 tons), the solubility for most of the elements is much higher than their concentration even after 10 years of full power operation, as exemplified for those elements where experimental data for the solubilities are available. Although this observation seems very comforting at a first glance, it may be very deceptive, too. Four factors must be borne in mind:

(1) Many of the elements tend to form compounds with the host materials, the solubilities of which may be quite different.

(2) The solubilities, given for a temperature of 450°C in Fig. 3 are often strongly temperature dependent and segregation is likely to occur at cold parts of the system.

(3) Although in rather dilute solution, elements must be expected to react among each other and some of them, such as halogens and chalcogens are known to enhance corrosion and to be readily transferred by metal halogenides and chalcogenides.

(4) A major problem may arise from the formation of mobile solid particles, intermetallic compounds, oxides, carbides nitrides, hydrides or hydroxides, which can have quite serious abrasive effects on protective surface layers on the walls.

Furthermore, some of the elements formed, as well as the hydrides, can be expected to reduce the protective oxide layer on the steel surface and thus give rise to severe enhancement of corrosion and liquid metal embrittlement.

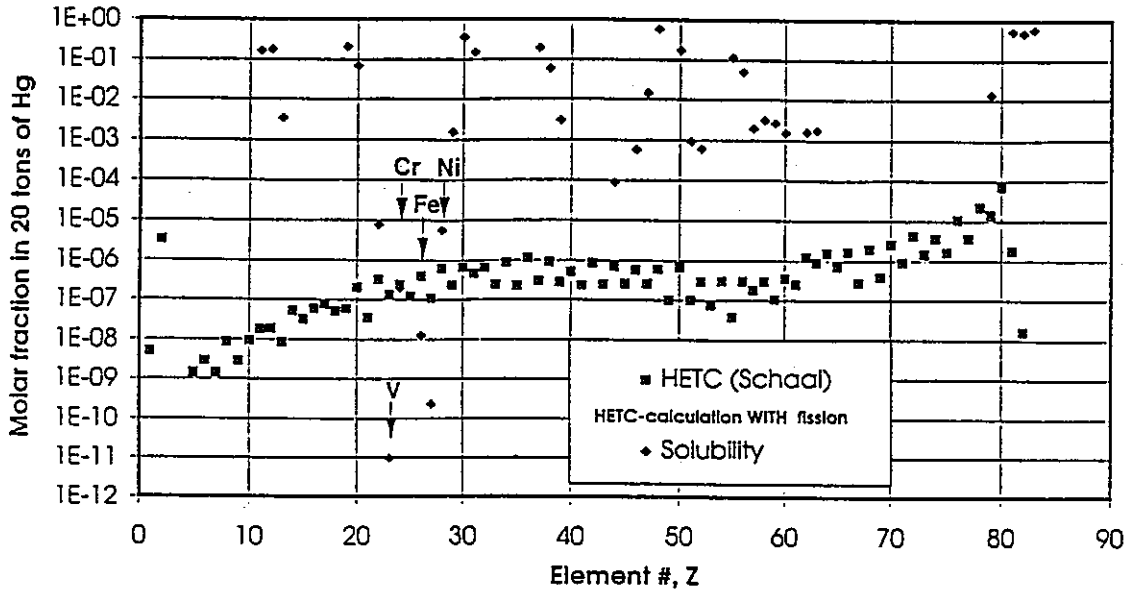


Figure 3. *Calculated element production in a mercury target after 10 years of operation at 5MW for 5000 hours per year [21], compared to experimental data on the solubilities (after [22]).*

It is, therefore, deemed necessary to study in some depth the chemistry of such a complicated system both, by theoretical as well as by experimental means [22]. As a theoretical basis it is proposed to use the MIEDEMA model [23] to calculate enthalpies of solution and reaction enthalpies for binary systems in order to identify most probable types of compounds as well as typical reaction partners as a basis for experimental verification.

For the experimental program solutions with known concentrations of selected elements will be prepared and marked by radioactive tracers generated in the PSI-isotope production facilities or with the fission product gas jet under construction at SINQ. Solid intermetallic compounds obtained from mixing solutions with different solutes will be analysed and the results compared to the theoretical expectations. Based on the results of these investigations which, at a later point, may also be extended to more complicated systems, it is expected to be able to predict the most significant potential problems in the target system and to devise means for their mitigation by suitable additions to the target material.

In order to determine the degree of corrosion attack by the "pure" target material on austenitic and martensitic stainless steels at different temperatures and for the situations of stagnant and flowing liquids, small-scale corrosion test rigs have been devised at PSI. The results of these investigations will contribute to determine the amount of foreign elements to be expected in a real target system and the degree of mass transport likely to occur between the hot and cold parts of the circuit. An important feature in these experiments is the possibility to examine samples under mechanical stress in order to determine its potential influence on liquid metal corrosion and/or liquid metal embrittlement.

Since, in the real situation, the walls will not only be subject to varying temperature and stress, but also to significant proton and fast neutron fluxes, the possibility is presently studied to set up an irradiation experiment at the beam stop of the Moscow Meson Factory of the Institute for Nuclear Research (INR) at Troitsk, Russia. The beam stop, as it is presently constructed, is shown in Fig. 4a [24]. Fig. 4b shows a schematic sketch of the bottom part of a possible replacement of the current Tungsten beam stop module by a liquid metal container which can be periodically rotated to minimise radiation damage to its walls, while the array of

specimens in the liquid metal is kept fixed to accumulate a high dose as desired. Specimens can be arranged such that some of them experience proton and fast neutron flux simultaneously while others are subject to the fast neutrons only.

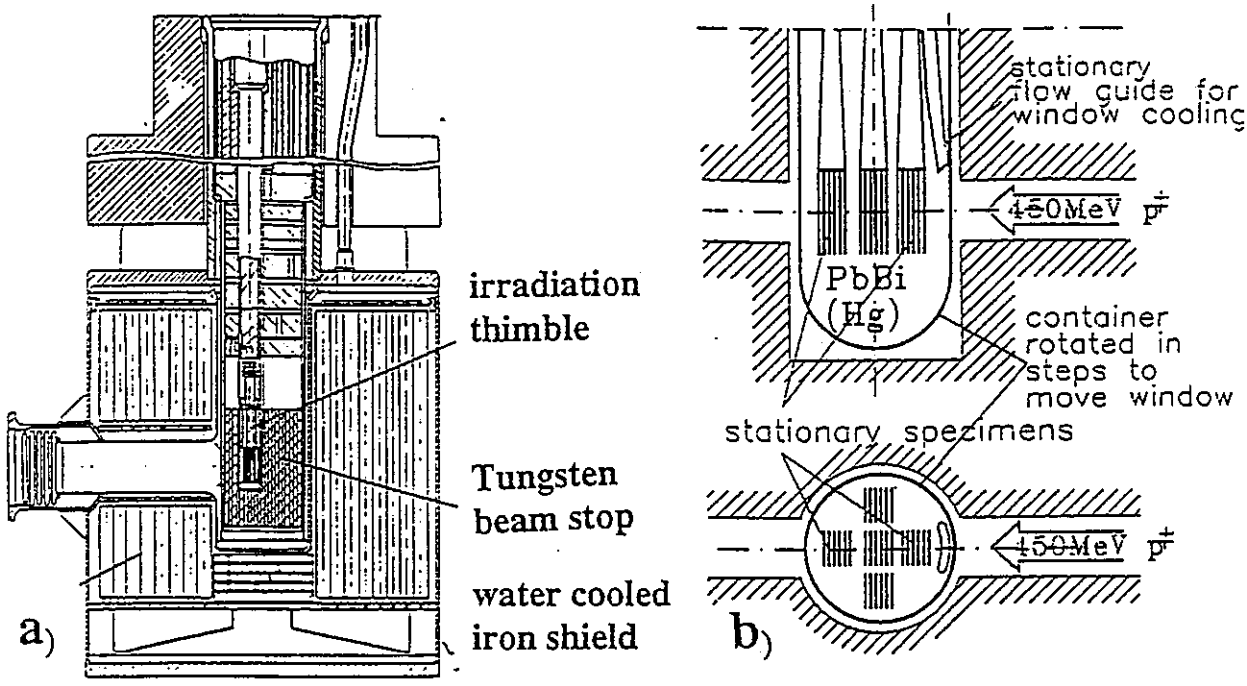


Figure 4. *The beam stop at the Moscow Meson Factory (a) and its proposed modification for irradiation experiments in liquid metals (b).*

While, in contrast to the situation in water, no highly reactive radicals are expected to prevail under irradiation in the liquid metal, it is not clear whether, or to what extent, synergetic effects must be anticipated from irradiation, stress and the chemical activity of the elements in contact. The proposed experiment could help answer this question.

## FLOW AND THERMAL HYDRAULICS IN HEAVY LIQUID METALS

In spallation systems the distribution of heat in the target-beam interaction zone is very inhomogeneous. Laterally it follows more or less the intensity distribution in the proton beam which, to a certain extent, can be controlled. Axially, however, the distribution shows a more or less exponential decrease, after a short build-up zone at the target head. For the case of ESS, for example, this results in a peak time average power density of 2.6 kW/cm$^3$, even with a beam whose footprint on the target is an ellipse with major axes of 20 and 6 cm [4]. In the steel window the peak power density is about 1.4 kW/cm$^3$ for the same conditions. Successful removal of this heat by liquid metal convection depends, among others, on sufficiently fast flow in all regions that need cooling. Modern CFD codes such as FLOW-3D or ASTEC allow to treat this problem theoretically in considerable detail, but experimental verification is required to validate these codes for the particular use and to demonstrate that the practical situation is in accordance with the theoretical model, in particular as far as solid-liquid heat transfer and the effects of heat conduction and buoyancy are concerned. While many such experiments can be carried out on model systems, a final full scale experiment is highly desirable, also to demonstrate that the system is mechanically stable and that no unexpected resonant vibrations are excited within the range of operating conditions, which might lead to premature failure from fatigue.

Experience with large liquid metal loops exists at MHD-Labs such as the ones at Ben Gurion University in Beer Sheva, Israel, and at the Institute of Physics of the Latvian Academy of Science in Riga. Planning is in progress to modify the large Mercury loop at Riga in such a way that test sections representative of the targets foreseen for SINQ, as well as for ESS, can be incorporated and measurements can be performed regarding the flow distribution, the mechanical stability and the heat removal from the beam entry window .

A technique to measure velocity distributions in opaque media by ultrasonic Doppler-shift analysis has been developed at PSI [25] and methods to investigate the heat transfer from an externally heated window into the liquid metal are currently being evaluated. This includes the use of small resistive heaters whose temperatures are determined via their resistivity through the voltage-to-current ratio and where the product of the two quantities is used to determine the power transferred to the wall. Another possible option to check for adequate window cooling might be to heat the window by radiation and to observe the temperature distribution with IR-cameras.

A question of particular concern in this context is the effect of wetting and/or gas residues in the liquid on the heat transfer from and to the walls. Both parameters may well be affected by the spallation products generated in the liquid and, in particular, by the cover gas atmosphere in the volume expansion tank of the system. Furthermore, in the case of ESS, one possible means discussed to mitigate the effect of pressure waves in the liquid is to inject in a dynamic way a small volume fraction of helium (see below). It is absolutely crucial that this shall not adversely affect the cooling of the beam window. By the same token, the effect of gas admixtures on the flow distribution itself must be studied.

## ADVANCED HEAT REMOVAL SYSTEMS

Removing the heat from the liquid metal requires special attention in two respects:

(1) the potentially high temperature level (in particular for Lead targets) may make use of conventional heat exchangers difficult due to the high temperature gradient across the walls;

(2) when the beam is shut off, heat removal must be terminated fast enough to avoid freezing of the target material in the heat exchanger (except for Mercury targets).

In an attempt to solve both of these problems, a study was initiated, aiming at variable conductance heat pipes that would contain a certain amount of non-condensable gas which would expand as the pressure in the heat pipe drops due to the lowering of the wall temperature and thus reduce heat transfer between the working fluid and the condenser part of the wall [26]. A design for such a heat pipe system suitable for use in a PbBi-target for SINQ and also (without the variable conductance feature) for the ESS-Mercury target has been completed and materials compatibility tests at the expected operating temperatures are presently being conducted. A PbBi-circuit is under preparation at PSI to allow field tests of complete heat pipes.

Use of heat pipes is expected to result also in an operationally very safe system because they provide extra decoupling for the secondary cooling system and overpressurization of the liquid metal circuit due to tube rupture in a heat exchanger is avoided, since only a small amount of working fluid is contained in each heat pipe. Also, there is enough design margin in each heat pipe to allow continued operation of the system even if one or a few of them fail.

## EFFECTS OF PULSED POWER INPUT

Since a liquid metal has only a very small compressibility, it is sensitive to sudden input of a large amount of energy. Hindered thermal expansion in a limited region will, in this case, give rise to the formation of pressure waves which, in turn, can cause substantial stress levels on the beam window and the container walls. This is particularly important for the case of ESS [4], where pulsed operation with 100 kJ per pulse at 50 Hz is planned. In order to estimate the magnitude of this effect, a computer code was developed [27]. The results of scoping calculations for a cylindrical target with a domed cover and the same peak power density as expected for ESS are shown in Fig. 5. The stress distribution along the wall (as labelled by a running index) is given as a function of time after the injection of a 1μs long pulse with an energy of 56 kJ, the fraction of the 100 kJ actually dissipated in the target volume as defined by the beam footprint and the axial distribution of the energy deposition. The peak stress reached (458 MPa), although only for very short time, is well beyond the maximum design limit for the type of steel foreseen for the target container. A reduction of more than two orders of magnitude can theoretically be obtained, if a volume fraction of 3% of gas is added in the interaction zone and the "bubbles" are assumed to have the same compressibility as Helium when compressed slowly.

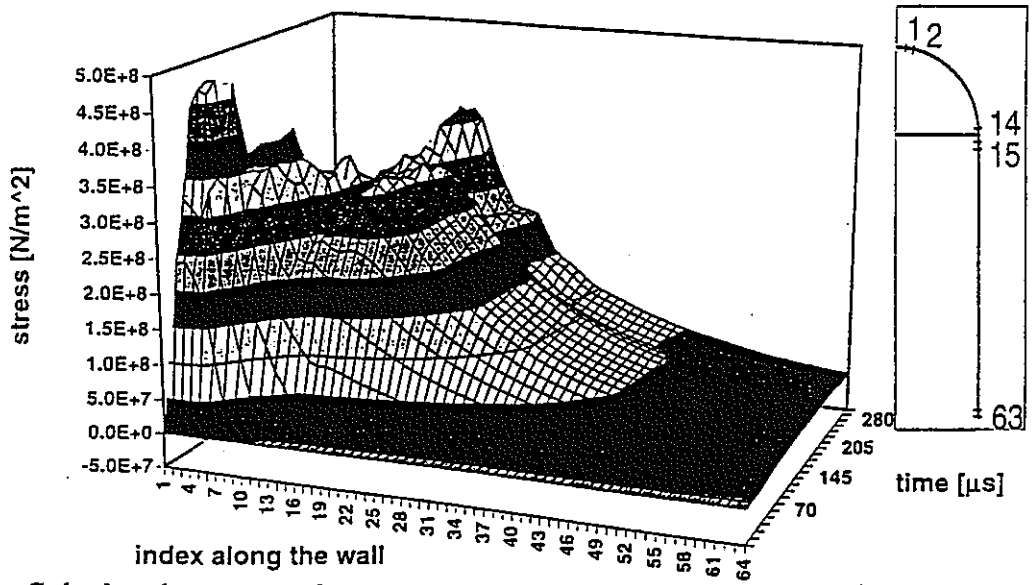


Figure 5. *Calculated stress on the target container wall for a cylindrical container of 20 cm diameter and with 3 cm thick walls, resulting from the deposition of 56 kJ of energy within 1 μs in the liquid. The insert shows the labelling used along the cylinder wall.*

Although this result seems to open up a way to eliminate almost completely the generation of pressure waves, it must be viewed with great caution:

(1) there is no quantitative experimental proof available so far;

(2) a method of obtaining a suitable distribution of Helium must still be developed and the effect of the gas on the flow and heat transfer must be investigated;

(3) the question whether small Helium bubbles can be compressed sufficiently fast is not clear.

While point (2) can be dealt with in the laboratory and is part of the program mentioned earlier, investigating points (1) and (3) is much more difficult. Fortunately, there is a proton accelerator available, the AGS at Brookhaven, which can deliver pulses of nearly 100 kJ, albeit at 7 GeV and with a duration of 2.4μs. These parameters can, however easily be used for theoretical calculations to be compared with measured data. Such comparison is

considered crucial for a final decision about the pressure wave mitigation strategy to be used in pulsed spallation neutron sources in the multi-megawatt range.

Figure 6 shows the recent improvements in beam intensity on the AGS [28]. With $7x10^{13}$ protons in one pulse and when extracting at 7 GeV, just before the transition energy of the AGS is crossed, the power per pulse is 78.4 kJ, which is enough to test the predicted effects both on the pressure waves in the liquids and on the window itself. Clearly such an installation would allow to perform a variety of other experiments ranging from verifications of predictions about energy- and geometry dependent total and differential neutron generation all the way to the test of new detector systems for high pulse intensity neutron counting.

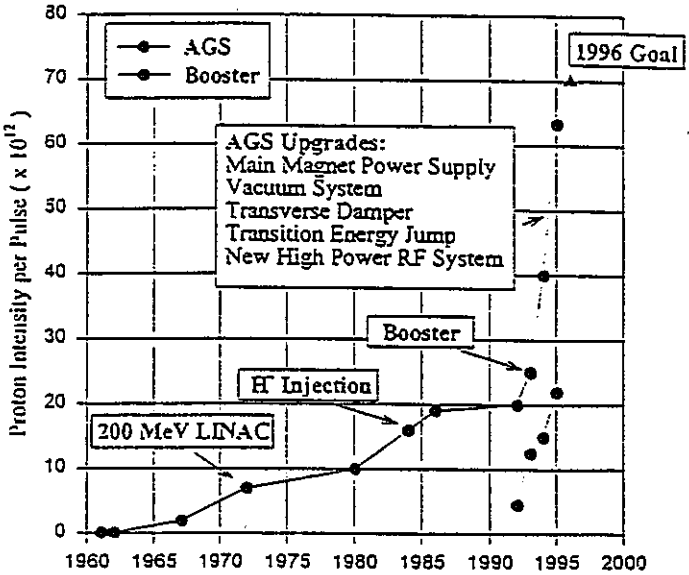


Figure 6. *The AGS proton intensity history*

A presently unused section of tunnel at the AGS could be reactivated to house this target test stand and, since the experiments would only be using one or a few pulses of beam at a time, no serious activation of the area or impact on other programs would have to be anticipated. Presently an evaluation of the total effort required to do these tests is being carried out.

## SUMMARY

Although much theoretical work has been carried out on the nuclear performance of spallation neutron devices for application in both, fundamental research and technical installations, very little information is available that would allow to assess the technology of such devices. This is true despite the fact that low power installations have been operating for a total of roughly 60 years now, and this experience and research done in conjunction with several proposal, in particular the one in Germany for a 5MW installation in the early 80ies [29], has been documented in the proceedings of up to now 13 meetings of the International Collaboration on Advanced Neutron Sources [30]. For this reason two workshops were recently organised [5], [6], aimed at establishing the needs and opportunities for research efforts to fill this gap. A variety of options have been identified. Several of them do, however, require significant level of funding. It is therefore clear that, in view of the widely spread and steadily growing interest in these questions an internationally co-ordinated and supported effort would be desirable to obtain the required information at optimum efficiency in utilising available resources.

## REFERENCES


[1] ESS-study report, part 2, to be published
[2] G.S. Bauer, "The New Swiss Spallation Neutron Source SINQ and its Planned Day-One Instruments" IAEA, Vienna, TECDOC-836 (1995), pp 97-114.
[3] B.R. Appleton in Proc. ICANS-XIII, PSI-Proceedings 95-02 (1995), pp 814- 818.
[4] G.S. Bauer, "The ESS-Project" this conference
[5] B. Appleton and G.S. Bauer, eds., Proc. Int. Workshop on the Technology and Thermal Hydraulics of Heavy Liquid Metals, Schruns, Austria March 24-29, 1996, ORNL-report CONF-9603171, to be published
[6] L.K. Mansur and H. Ullmaier, Proc. Int. Workshop on Spallation Materials Technology held at Oak Ridge, USA April 23-25, 1996, to be published.
[7] J.M. Carpenter and A.G. Hins "Experience with IPNS Targets" Proc. ICANS-XII, report RAL 94-025, (1994) pp T1-T11.
[8] T.A. Broome, private communication
[9] N. Bultman and W. Sommer, MLNSC-Upgrade Review, (Feb 1996), priv. com.
[10] W. Sommer, in Materials for Spallation Neutron Sources, report LA-13097-C (1995)
[11] G.S. Bauer " Workshop recommendations on materials selection " in [6]
[12] Y. Dai "Materials Selection for ESS Mercury Target Container" in Proc. ICANS-XIII, PSI-Proceedings 95-02 (1995)
[13] H. Ullmaier and F. Carsughi, NIM B101(1995)
[14] F. Garner, this conference
[15] M. Louthan, discussion contribution in [6], F. Garner, this conference
[16] E. Camus, N. Wanderka and H. Wollenberger Proc ICANS-XII and ESS-PM4, PSI-Proceedings 95-02, (1995) pp. 707-715
[17] M.B. Lewis, W.R. Allen, R.A. Buhl, N.H. Packan, S.W. Cook and L. Mansur: Nucl. Inst.Meth. in Physics Res. B 43 (1989) 243-253
[18] W.F. Sommer et al, this conference, paper M9.
[19] M. Victoria and D. Gavillet, Proc. 1st Int. Conf. ADTTA, Las Vegas AIP Cof Proc 346, (1994) pp 891-902.
[20] R.I. Klueh and D.J. Alexander in ASTM-STP 1125, (1992) p. 1256 and ICFRM-7, to be published in J. Nucl. Mat.
[21] H. Schaal, private communication (1996)
[22] B. Eichler and R. Dressler in ESS-Liquid Metal Target Studies, 2nd Status Report, G.S. Bauer, ed., report ESS 95-33-T, (Oct. 1995)
[23]A.K. Nissan, F.R. deBoer, R. Boom, P.F. deChatel, W.C.M. Mattens, F.A.R. Miedema : CALPHAD 7 / 1, (1983) 51
[24] Yu.Ya. Stavissky in Proc ICANS XI report KEK-90-25, (1990) pp. 87-99
[25] Y. Takeda, in Experimental Heat Transfer, Fluid Mechanics and Thermodynamics 1 (1993) pp 126-131.
[26] M.T. North, J.H. Rosenfeld, D.B. Sarraf, G.S. Bauer and Y.Takeda, in Proc. ICANS-XIII, PSI-Proceedings 95-02 (1995) pp 559-571
[27] K. Skala and G.S. Bauer, in Proc. ICANS-XIII, PSI-Proceedings 95-02 (1995) pp 559-576
[28] D. McWhan, private communication
[29] G.S. Bauer, H. Sebening, J.-E. Vetter, and H. Willax (eds.) "Realisierungsstudie zur Spallations-Neutronenquelle" report Jül-Spez-113 and KfK 3175 Kernforschungsanlage Jülich und Kernforschungszentrum Karlsruhe (1981) and G.S. Bauer, Atomkernenergie-Kerntechnik 41 (1982) p.234-242
[30] Information on ICANS is available on the World Wide Web under the URL: http://www.pns.anl.gov/icans/icansdescript.html.

# The European Spallation source Study, ESS

**G.S. Bauer**

*Paul Scherrer Institut,*
*CH-5232 Villigen-PSI, Switzerland*
*- for the project team -*

Paper prepared for

*Second International Conference on Accelerator Driven Transmutation Technologies and Applications*
**3-7 June 1996, Kalmar, Sweden**

# The European Spallation Source Study, ESS

G.S. Bauer
*Paul Scherrer Institut, CH-5232 Villigen PSI*
*- for the ESS-Study Team -*

**Abstract.** A Europe-wide effort to study a next generation pulsed spallation neutron source has been conducted over a period of 2 years. The work lead to a concept for a 5 MW beam power short pulse (1 μs) facility which is driven by a linac of 1.334 GeV of energy and 50 Hz repetition rate. In order to achieve the desired short pulses, the linac beam is accumulated in two compressor rings which are filled by charge-exchange multiturn injection and emptied over a single turn. Although this feature, as well as the resulting high power of 100 kJ per pulse, pose special requirements to the design, many of the main parameters of the project can be considered as prototypical for an ADTT-facility. This includes the 100 mA current requirement for the linac as well as the technology of the liquid metal target which was chosen to optimize neutron generation and make the high power density manageable.

## INTRODUCTION

Throughout the development of nuclear technologies research neutron sources have played an important role in providing essential data and experience for the design of technical and industrial facilities as well as in serving fundamental and applied science in a variety of ways. This was true for fission-based systems and it will also be true for future, technically even more demanding accelerator-based systems. Although, like in the case of advanced research reactors, advanced research spallation neutron sources will ultimately have to fulfil more demanding requirements than their technical counterparts, the technologies used and the problems that need to be solved are the same.

Much of our present knowledge about spallation and accelerator technology has in fact been acquired during the design, construction and operation of existing research facilities, among them the four operating spallation neutron sources in Japan, the US and the UK, although they are of relatively low power only.

While the ESS now under study in the European Union is clearly designed as a very high performance research facility, its pulse parameter are close to the upper limit of the beam parameters discussed for ADTT-facilities.

## THE BASIC CONCEPT OF ESS

ESS is designed as a short pulse spallation neutron source. This has deliberately been decided in this way because

(1) short pulse spallation sources have demonstrated excellent scientific potential in various fields of research using neutron scattering and have broadened substantially the range of application of neutrons to science, providing possibilities which are, to a large extent, complementary to high flux reactors and

(2) short pulse sources are technically more demanding than continuous or long pulse spallation neutron sources. So, by studying a short pulse source, implications of building a long pulse source would automatically become known.

Neutron sources to be used for neutron scattering must provide neutrons that were slowed down by several orders of magnitude from the energy with which they were released from their parent nucleus. A short pulse neutron source (SPNS) is then defined as a facility in which the duration of the neutron pulse is determined by the properties of the moderator, and not by the duration of the beam pulse generating the fast neutrons. So, the obvious design goal of an SPNS is to provide as many neutrons of a desired energy range as possible in a pulse as short as possible and at a suitable repetition rate to make optimum use of the neutrons.

The total number of neutrons generated scales roughly with beam power, which was chosen to be 5 MW for ESS, i.e. a factor of 30 higher than the present most powerful pulsed spallation source, ISIS [1] at Rutherford Appleton Laboratory in the UK (160 kW). A reasonable pulse repetition rate being 50 Hz, this means that, with an accelerator current of 100 mA as presently considered an achievable goal in a linac [2] pulses of 500 μs duration would result. On the other hand, slowing-down of neutrons in a moderator is much faster than this. A good estimate can be obtained from the rule-of thumb:

$$v \cdot \Delta t_s = C \qquad (1)$$

with v being the desired neutron velocity (20000 m/s and less) and $\Delta t_s$ the standard deviation of the time it takes to slow neutrons down to the velocity v. The constant $C$ depends on the slowing-down density of the moderator and is found to be of the order of 2 to 3 cm in a good moderator, like water. In order not to contribute significantly to the pulse width, the proton pulse should then be shorter than $10^{-6}$ sec or 1 μs.

In order to achieve this, the beam coming from the linac must be stored in an orbit into which it can be injected over many turns and then be extracted in a single turn. This is called pulse compression. Depending on the amount of current to be stored, this may require more than 1 ring, because the number of particles that can be stored in a single ring is estimated to be about $2 \cdot 10^{14}$. For ESS two rings have been chosen. After extraction from the compressor rings, the beam is directed onto the target which is designed to generate as many neutrons as possible in as small a volume as possible. This requires a maximum density of heavy metal, with as little dilution by cooling channels as possible. This is one reason, why a flowing liquid metal was chosen as target material for ESS. Other reasons are the absence of structural radiation damage in the target material, the high heat removal capability and the fact that no spallation products are generated in the cooling water circuit because the metal-to-water heat exchanger can be located in a region away from the beam-metal interaction region.

The neutrons generated in the target should be slowed down as efficiently as possible in small moderators to keep distance (flight-time) effects on the neutron pulse small. Depending on the desired use of the neutrons, either ambient temperature ($H_2O$) or cyrogenic temperature (liquid $H_2$) moderators are used. In order to moderate as many neutrons as possible, the small moderators are surrounded by reflector material which should scatter neutrons that would otherwise escape the moderator, and thus increase their probability of hitting the moderator. The reflector may also return slow neutrons back into the moderator which, in some cases may lead to undesired pulse broadening. In order to avoid this, the moderator are often „decoupled" from their surroundings by a material of high absorption cross section for slow neutrons, such as Boron or Cadmium. Similarly, to limit the depth from which neutrons can diffuse to the surface after thermalization, an absorber, called poison, is placed at a certain depth below the moderator surface.

Figure 1 shows the principal layout of a short pulse neutron source and Table 1 gives the parameters chosen for ESS.

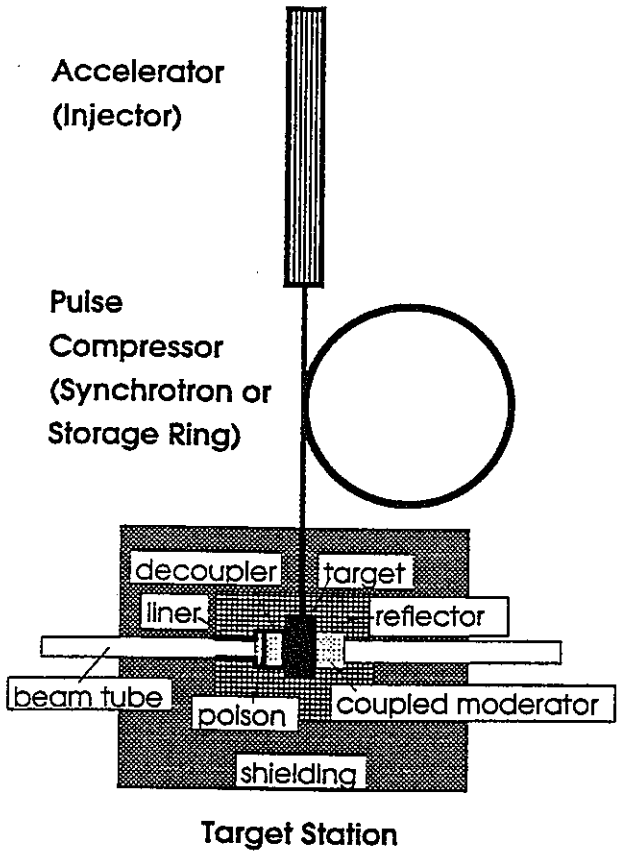


Fig. 1 *Schematic of a short pulse neutron source showing the linear accelerator, pulse compressor ring and the target and moderator with their surrounding reflector and shielding. Decoupling and poisoning is indicated for one of the moderators.*

Table 1 *ESS Parameters*

Baseline

| | |
|---|---|
| Power in the proton beam: | 5 MW |
| Pulse repetition rate | 50 Hz |
| Proton pulse duration: | < 1 μs |
| Two target stations, pulses shared | 4:1 ratio |

**Reference Concept**

Accelerator system:

Injection 70 keV $H^-$
Rf-linac 1.35 GeV
  pulse current 100 mA
  duty cycle 6%
Followed by two compressor rings
  pulse of 2x 400 ns (1 μs total) duration,
  74 μAs (4.63 E14 protons, 100 kJ)
Beam on target:
  2-dimensional parabolic,
  6 cm x 20 cm base width

Target system:

TH 5 MW beam power, 50 Hz, 1 μs, horizontal injection, Mercury target

TL 1 MW beam power, 10 Hz, 1 μs, horizontal injection, Mercury target

A large degree of flexibility exists in the layout of the moderator-reflector system to suit the users' needs best. Much of this does not need to be decided up front, because the moderators and reflectors, as well as the target, must be exchangeable for radiation damage anyhow.

As a reference, four different types of moderators, cryogenic and ambient, with and without decoupling and poisoning have been selected and their performance has been evaluated. Fig. 2 shows the pulses calculated for the coupled ambient temperature water moderator for different reflector configurations [3].

The overall layout of the facility is shown in Figure 3. After compression to a double pulse of 400 ns each, with a separation of 200 ns between them, the beam is directed onto the target stations via a switchyard which allows to deflect individual pulses onto one of two target stations. While differing in details of their utilization, the two target stations will employ the same technology because the requirement to withstand the full load of the

100 kJ pulses is the same for both and substantial savings are expected from using the same type of equipment and parts in both target stations. The standard mode of operation will be for one target station to receive 4 out of 5 pulses with a time separtation of 20 msec (50 Hz-station) and the second one to receive pulses at 10 Hz repetition rate (average power of 1 MW). The low repetition rate target station will be mainly used for cold (slow) neutron work which requires longer time frames.

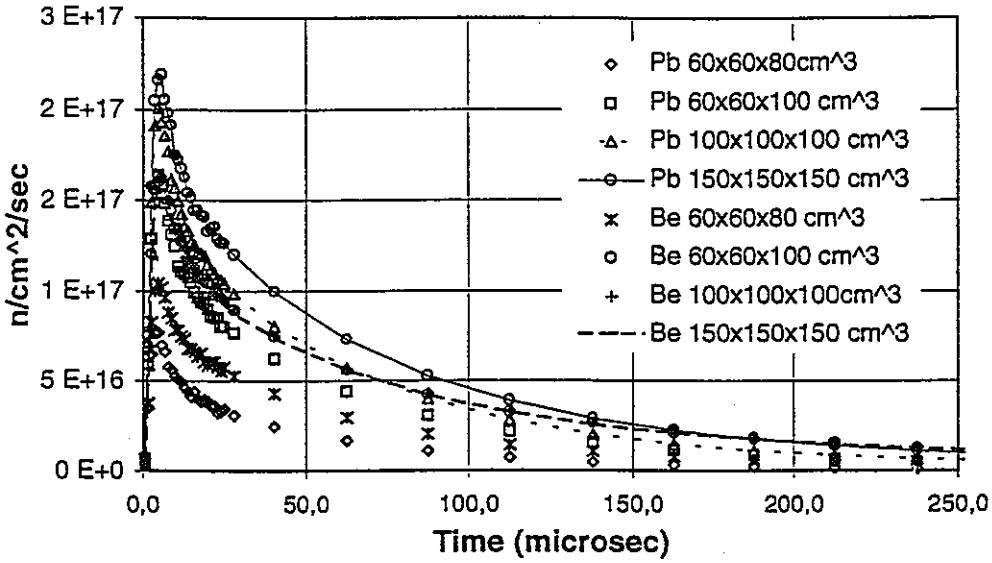


Fig. 2 *Pulse shapes for the thermal neutron pulse as calculated for a mercury target and a coupled ambient water moderator surrounded by reflectors of different materials (Be and Pb) and sizes [3].*

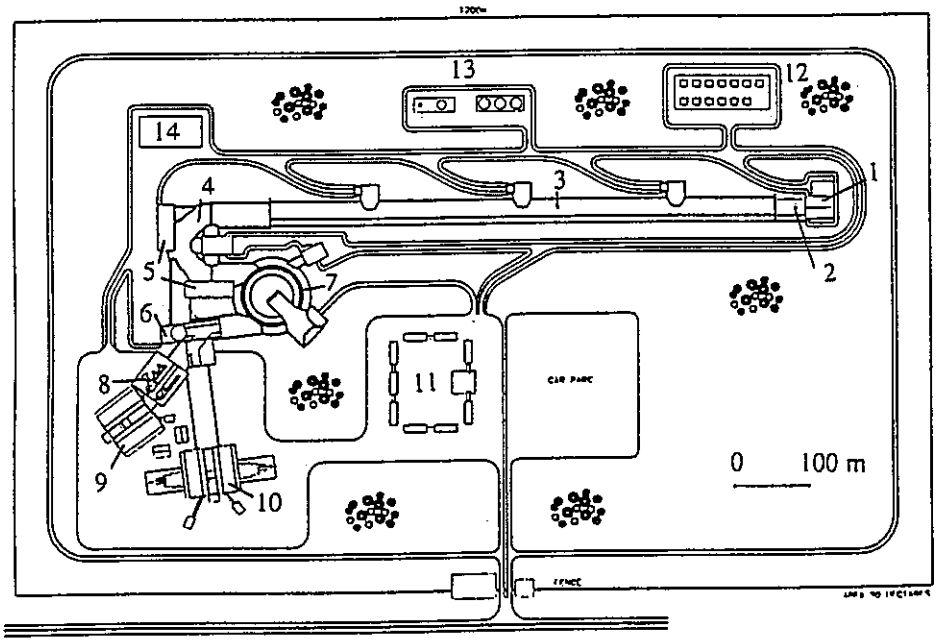


1 Injection Hall
2 Drift Tube Linac
3 Side Coupled Cavity Linac
4 Achromat Arc
5 Beam Dumps
6 EPB-Switchboard & Beam Dump Hall
7 Accumulator Rings Hall
8 Muon Hall
9 5MW Target Station
10 1MW Target Station
11 Faculty Building
12 Electricity Sub-Station
13 Cooling Plant
14 Waste Management Facility

Fig. 3 *Site plan of the ESS-facility showing the arrangement of the accelerator- and target buildings as well as user and support facilities.*

## THE ESS-ACCELERATOR SYSTEM

The choice of accelerator parameters is discussed in detail in ref [4]. Here we only outline the arguments that lead to the final decisions. Although optimization of neutron yield from the moderators, and hence neutronic coupling from the target to the moderators,

is a major concern in ESS, it turns out that, in the range from little under 1 GeV up to several GeV, proton energy is not a big issue in this context [5]. Neutronic performance depends, to a first approximation, on beam power only. In a second level of optimization, proton energy enters through

a) the cost of the accelerator system for a given power level

b) current limitations in the accelerator system

c) the fact, that only about $2 \cdot 10^{14}$ particles can be stored in one ring and the number of rings required thus depends on beam energy at a given power

d) radiation damage considerations in the window separating the proton beam vacuum from the target coolant.

e) beam losses associated with certain necessary manipulations; for ESS in particular the injection into the compressor rings.

It turned out that b) and e) were the most important aspects for ESS because injection into the compressor rings requires acceleration of $H^-$-ions in order to be able to use stripping to $H^+$ at injection for efficient and rapid filling of the phase space in the ring at optimum density. This affects strongly the design of the low energy end of the linac and also has an influence on the choice of its final energy.

Since $H^-$-ion sources of the required performance (approx. 200 mA current and 10% duty cycle) are presently not available - and may not be even after a reasonably high development effort, the decision was made to incorporate a funneling section in the low energy part of the linac which merges the beams from two ion sources and preaccelerators into one at twice the microbunch frequency (Fig. 4). This certainly complicates the system relative to acceleration of protons but it keeps the necessary R&D-effort on this issue at a reasonable level.

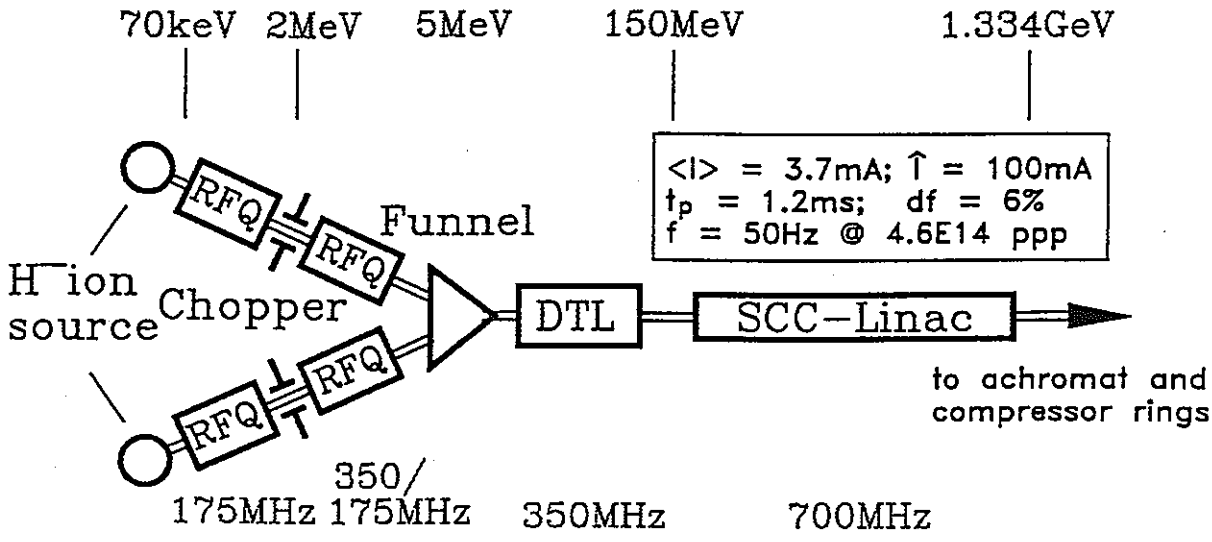


*Figure 4: Schematic representation of the ESS-linear accelerator showing the two low energy lines plus funnel and the intermediate and high energy sections with their respective energy limits and rf-frequencies.*

The low energy end thus consists of two ion sources with 70 keV preacceleration, followed by one 175 MHz RFQ each. A beam deflector (chopper) is installed behind each of these RFQs to be able to impose the necessary time structure on the beam (see below). The chopping energy of 2 MeV is chosen to have a sufficiently well defined beam on the one hand and not to cause severe activation on the other.

The chopped beams are then accelerated to 5MeV in two 350 MHz-RFQs with only every other bucket filled. After merging in the funneling section, the bunch frequency doubles and in the 350 MHz coupled cavity drift tube linac that accelerates the beam to 150 MeV, every bucket is filled. At 150 MeV a transition is made to the high-$\beta$ structure which is a 700 MHz side coupled cavity linac.

As explained in detail elsewhere [2], great care must be taken to match the lattice structure between the various sections of the linac, in order to minimize losses and activation along the accelerator. The goal set for ESS is no more than 1 nA/m loss in the high energy part of the linac, in order to ensure the long term possibility of hands-on maintenance.

Besides the normal-conducting side-coupled structure chosen for the reference design, a super-conducting, on axis-coupled structure is also being considered for the ESS-linac. The recent progress made in developing superconducting cavities even for pulsed operation may make this a very attractive option. It would allow an accelerating gradient of 8 MeV/m in the cavities and could result in a much shorter and more energy efficient linac than the normal conducting one would be. The total length of the superconducting linac is estimated to be about 300 m, as compared to 660 m for the normal conducting version.

As mentioned before, the decision on the final energy of the linac was also affected by the need to inject into the compressor rings, which is accomplished by passing the beam through a stripper foil (thin $Al_2O_3$-sheet) located inside a dipole magnet. Careful matching between the field strength of this dipole (0.177T), the thickness of the foil (345 $\mu g/cm^2$) and the energy of the protons (1.334 GeV) is expected to help minimize uncontrolled losses at injection. It is anticipated that 98.5% of the beam will be trapped. An incompletely stripped $H^0$-beam of about 75 kW power (ca. 60 $\mu A$) can be collected and used for example to feed a radioactive ion beam facility.

Low loss injection also requires careful phase-space matching and halo scraping which is accomplished by a 180° achromatic bend between the linac and the rings, which can, in addition, provide some energy ramping during the filling time of each ring.

Since it is necessary to keep part of the rings' circumference free of beam to be able to excite the extraction system, a rather sophisticated time structure must be imposed on the linac beam by the chopping system in the low energy end. For injection into 1 ring, this is shown in Fig. 5. The chopping results in a 60% fill factor of each linac macropulse only, making correspondingly longer pulses (1.2 ms) necessary to provide the desired pulse charge.

The two rings will be located on top of one another. After the first ring is filled, the beam will be stored until filling of the second one is complete. Both rings will then be emptied sequentially with a pulse duration of 400 ns from each ring and a 200 ns gap between them to be able to merge both pulses into the same beam line.

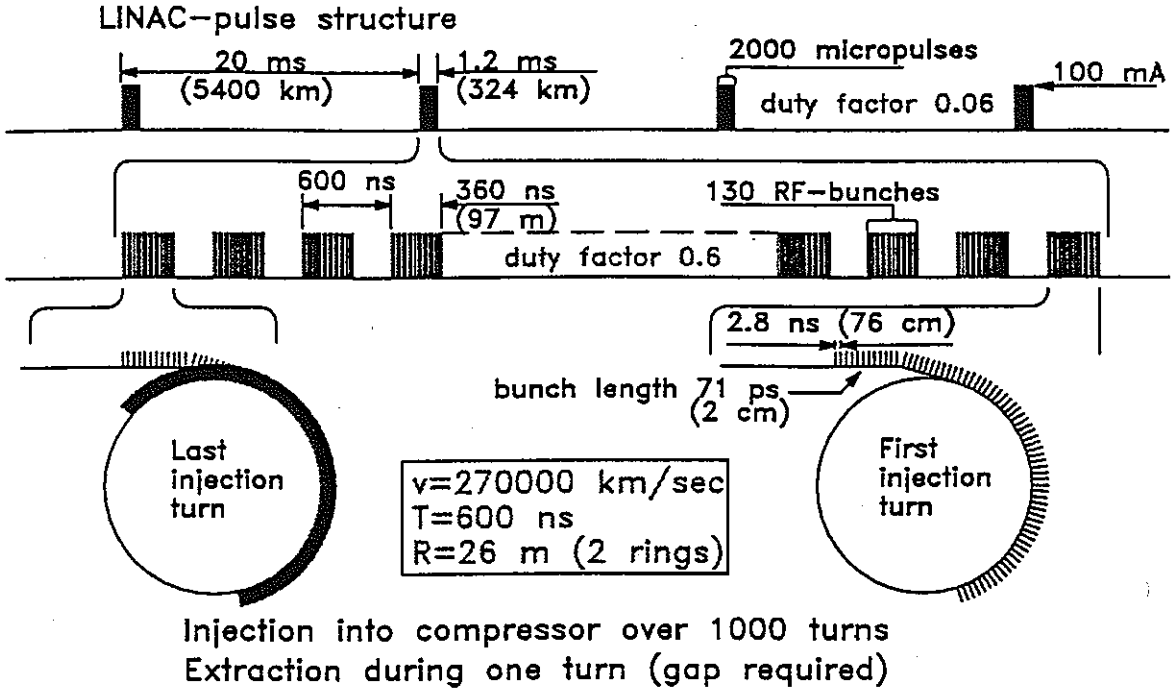


*Figure 5: Time structure manipulation for injection into a compressor ring at ESS.*

## THE ESS-TARGET SYSTEM

Although the proton pulses hitting the ESS-target will be double pulses of 400 ns each with 200 ns separation, for all practical purposes they will appear as 1 μs long single pulses. Each of these pulses contains 100 kJ of energy, about 60% of which will be deposited at a rate of 50 Hz in the target volume. The beam cross section has been defined as elliptical with major axes of 20 and 6 cm and a 2-dimensionally parabolic intensity distribution leading to a maximum current density of 80 $\mu A/cm^2$ on the beam entry window. Mercury was chosen as target material for a variety of reasons [6], mainly because it does not require auxiliary heating and has the highest density of all candidate liquid metals. Also, in contrast to Lead and, in particular, Bismuth no α-active Polonium is generated in Mercury. The high thermal neutron absorption cross section of Mercury is not a disadvantage for a pulsed source, because the target material is expected to act as its own decoupler from the moderators.

Fig. 6 shows the calculated power density in the innermost cylinder of 1 cm radius along the beam axis [7], and Fig. 7 gives the calculated neutron leakage from a slab-type target which is surrounded by a lead reflector [8], showing that the neutron yield of a Mercury target is superior to that from its solid competitors Tungsten and Tantalum, which must always contain a certain fraction of cooling water ($D_2O$, varying from 22% at the high heat load region to 8% at the downstream end). This cooling water not only dilutes the target density, it also moderates neutrons and makes them susceptible to resonant absorption.

A schematic representation of the Mercury target system and its surroundings is shown in Fig. 8. In the beam interaction zone the shell containing the Mercury is surrounded by a double-walled, water cooled hull which serves to return the Mercury to its storage tank in case of a leak in the inner shell. Since the inner shell beam window must be cooled by the

Mercury, a configuration of baffles was developed, which generates sufficient directed flow across the window to cool it on the one hand and reduces recirculation behind the window to a level where no unallowably high temperatures occur in the liquid on the other. In order to optimize window cooling and to move the hot spot as far down into the target as possible, the forward flow is in the peripheral parts of the target volume (bottom and side channels) and the return flow is in the central part of the target. In this way the target material is hit (and heated) by several pulses as it moves away from the beam window and the hot spot is generated at a distance of about 42 cm downstream from the window (Fig. 9).

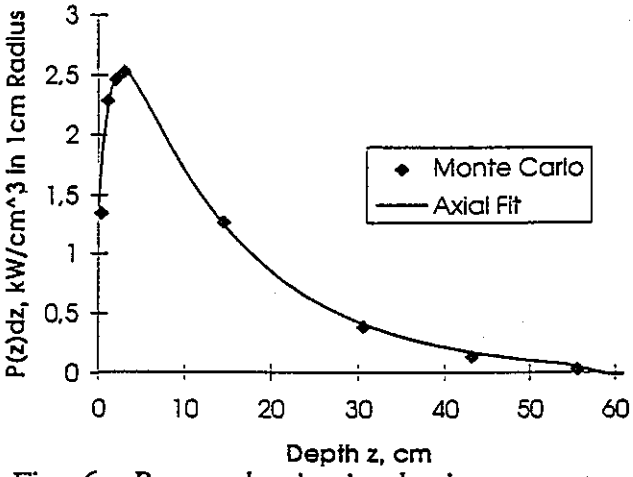


Fig. 6 *Power density in the inner most cylinder of 1 cm radius of the target as obtained from Monte Carlo calculations.*

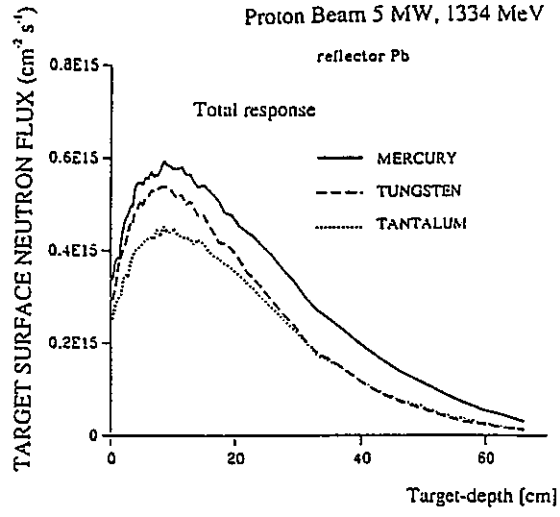


Fig. 7 *Calculated neutron leakage for targets of Mercury, Tantalum and Tungsten (the latter ones containing $D_2O$ for coolant) for 3.75 mA of 1.334 GeV protons and embedded in a lead reflector.*

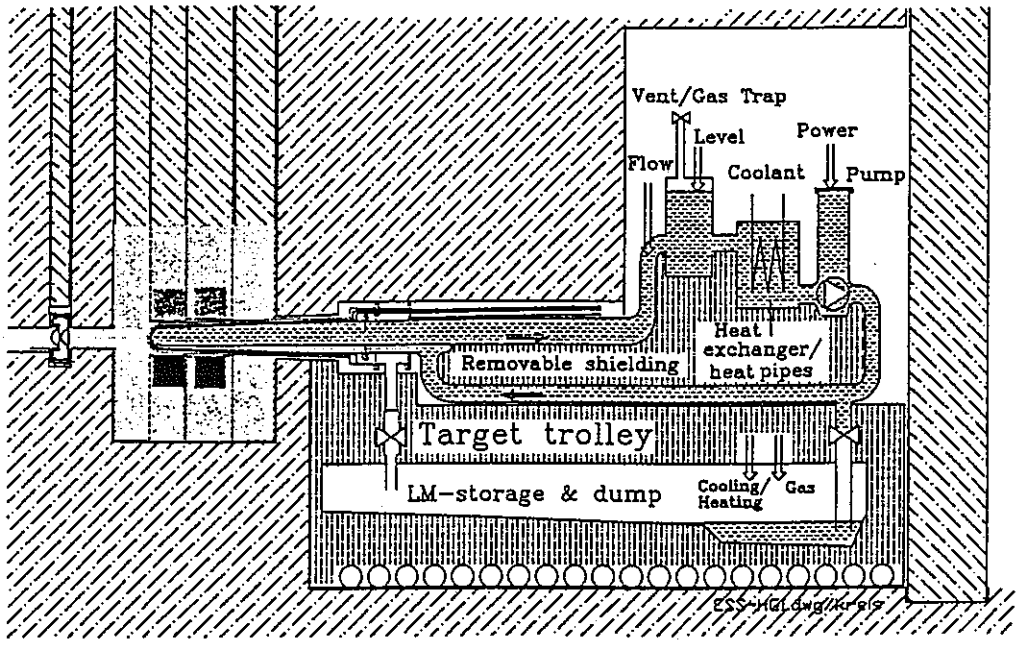


Fig. 8 *Schematic representation of the ESS-liquid mercury target circuit and its surroundings. Only the shell containing the Mercury in the beam interaction region and the surrounding Mercury return hull will have to be exchanged at regular intervals for radiation damage.*

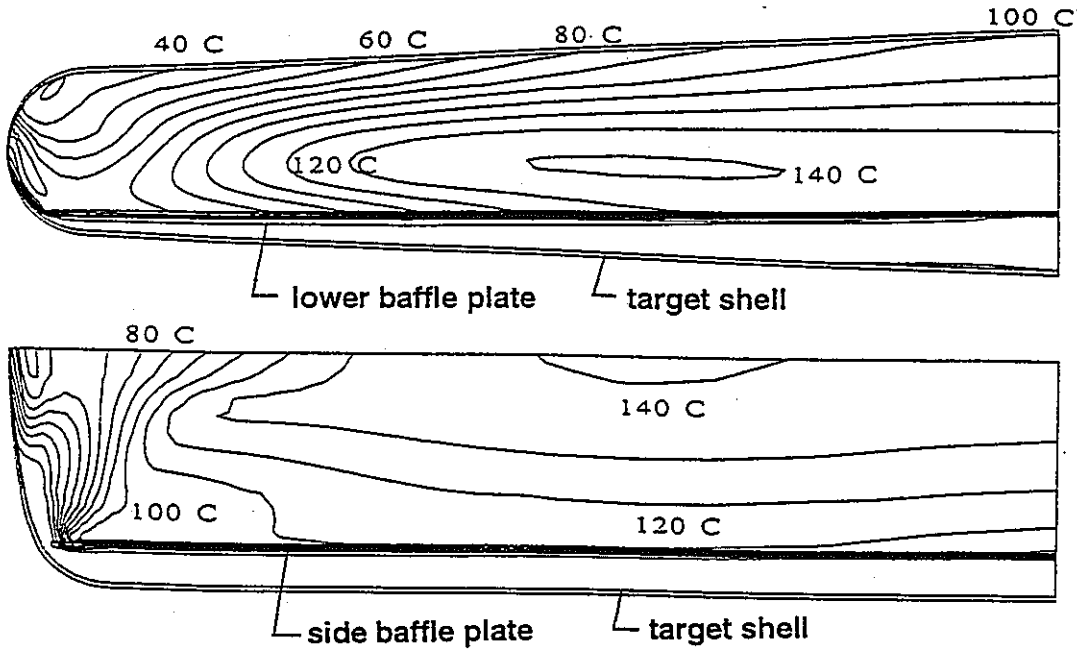


Fig. 9: *Temperature distribution in the vertical (top) and the horizontal plane (bottom, only one half of the target shown) of the active target region of the ESS-Mercury Target containing the point of maximum temperature.*

Several details of the liquid metal target concept have yet to be worked out. This includes the liquid metal-solid metal chemistry as affected by the spallation products generated, the choice of the most suitable container material, as well as the decision about pumping, heat removal and diagnostics. All these are not real feasibility questions but will affect the maintenance intervals and concept and thus the overall availability and cost of the facility. Current experience is that steel (Inconel 718) can survive at least $7 \cdot 10^{21}$ protons/cm$^2$ [9], when used for water cooled beam windows. Accounting for the fact that, at the ESS-target, fast neutrons will generate almost the same radiation load as the proton beam and that the peak current density at the beam window is about 80 μA/cm$^2$, this would lead to an expected service time of the outer (water cooled) hull of roughly 1600 hours which is about 1/3 of the anticipated annual operating time.

As for the target container, nickel-containing materials may be susceptible to liquid-metal corrosion and/or embrittlement. Little information is available on this problem, but a research program has been initiated [10] to investigate these questions and also the effect of simultaneous stress and irradiation on the evolution of the mechanical properties of candidate materials, in particular 316 austenitic stainless steel and some types of nickel-free ferritic-martensitic steels. This program will also include research into the effects of the pulsed power input which might have rather severe consequences in terms of stress on the container walls, as first calculations have shown [11]. The assumptions made in these calculations (e.g. zero tensile strength of the liquid even for short times) and possible ways to mitigate the effect of pressure waves proposed will also be subject to further study in the upcoming R+D-phase.

## CONCLUSIONS

The present study has demonstrated that a spallation facility with 5 MW beam power is feasible with existing technology. The special feature of short pulsing required in order to achieve the goals set for ESS as a scientific tool make the facility more demanding that an ADTT-device in some respects and, while solutions for the resulting problems have been proposed, important R+D work is still required to prove their viability. In other respects, such as high current accelerator and liquid metal target technolgy, ESS can well be considered as prototypical for an ADTT-device. Its further development, construction and operation will therefore not only provide condensed matter science with an unprecedented tool, it will also mark an important milestone in the endeavors to develop the new technology of accelerator driven transmutation devices and power generation facilities.

## REFERENCES

[1] see e.g. ISIS annual report 1994-95, Council for the *Central Laboratory of the Research Councils*, RAL-95-050 (1995)

[2] S. Schriber, this conference

[3] A. Tietze, Diploma Thesis, KFA Jülich (1996)

[4] H. Lengeler, in Proc. ICANS-XIII and ESS PM4, *Paul Scherrer Institut*, report PSI-Proc. 95-02 (1995) pp. 819-830

[5] D.W. Jerng and J.M. Carpenter, Proc. ICANS-XII, *Rutherford Appleton Laboratory*, report RAL 94-025 (1994) pp. T105-T114

[6] G.S. Bauer, Proc. ICANS-XIII and ESS-PM4, *Paul Scherrer Insitut*, -report PSI-Proc. 95-02 (1995) pp. 547-558

[7] R. Neef, private comm.

[8] D. Filges, R.D. Neef and H. Schaal, Proc. ICANS-XIII and ESS PM4, *Paul Scherrer Institut*, report PSI-Proc. 95-02 (1995) pp. 537-546

[9] W.F. Sommer, private comm. (Feb. 1996)

[10] G.S. Bauer, this conference

[11] K. Skala and G.S. Bauer, in Proc. ICANS-XIII and ESS-PM4, *Paul Scherrer Insitut*, report PSI-Proc. 95-02 (1995) pp. 559-576

付録-13

**Thermohydraulic behavior of the liquid-metal natural-circulation target of the spallation neutron source at Paul Scherrer Institute**

NUCLEAR SCIENCE AND ENGINEERING: 113, 287–299 (1993)

# Thermohydraulic Behavior of the Liquid-Metal Natural-Circulation Target of the Spallation Neutron Source at Paul Scherrer Institute

Y. Takeda and W. E. Fischer

*Paul Scherrer Institute, CH-5232, Villigen PSI, Switzerland*

*Received April 14, 1992*
*Accepted July 2, 1992*

**Abstract**—*The thermohydraulic behavior of the liquid-metal target of the spallation neutron source at Paul Scherrer Institute has been investigated. The configuration is a natural-circulation loop in a concentric double-tube-type container. The model is based on a one-dimensional loop analysis, and the thermohydraulic behavior of the target liquid, as well as the total performance of the target, are studied analytically and numerically. These results are verified by two experiments using liquid metal. The results show that the natural-circulation loop concept is valid for the design phase of the target construction, and the current specified design criteria will be fulfilled with the proposed parameter values.*

## I. INTRODUCTION

The SINQ project at Paul Scherrer Institute (PSI) is to construct a spallation neutron source at the physical end of a proton cyclotron beamline[1] (590 MeV, 1.5 mA) (Fig. 1). Heavy nuclei in a target are bombarded by the proton beam in order to generate neutrons by a spallation nuclear reaction. For efficient neutron generation in the target, either lead-bismuth eutectic (LBE) or pure lead will be used as a target material, and one of these will be contained in a long, vertical, cylindrical container. The design is intended for effective coupling between the target and a heavy water moderator. Since specific heat generation in the target is nonuniform and fairly large (~1 MW/ℓ), the target is used in the liquid phase. Historically, with the proton beam directed vertically upward from the bottom into a liquid target, natural-convection heat transfer of the target material itself has been used as the primary cooling mechanism. However, it has been found experimentally[2] and numerically[3] that with this configuration, there are difficulties in the control of the facility due to a hydrodynamic instability. Subsequently, the configuration was modified by adding a coaxial tube inside so that the cooling mechanism is a natural-circulation loop of the coaxial tube type (Fig. 2). We call this inner cylinder the guide tube. This configuration is attractive from the standpoint of maintaining the dimensions of the outer containment of the target, providing efficient transport of the heat deposited by the proton beam from the reaction zone to the cooling zone, enabling a higher liquid velocity than that by natural convection and thereby lowering the maximum temperature in the system, and not necessitating the placement of a cooling water circuit down in the reaction zone.

The natural-circulation loop is simple in configuration and efficient in generating flow circulation. Its mechanisms are relatively well understood and extensively used in industry. Recent studies, as reviewed by Mertol and Greif[4] and by Greif,[5] show that a wide range of applications is possible. It is also of consequence that a one-dimensional analytical model can successfully predict the overall behavior of the steady-state temperature distribution and average velocity. Most of the early works, however, except for a toroidal loop, were done in a configuration of a closed loop that consists of two vertical legs. For a concentric two-tube geometry, Seki et al.[6] performed experiments using water, and their results were analyzed by Steimke[7] using a one-dimensional model. These studies were, however, for high-Prandtl-number liquid and directed

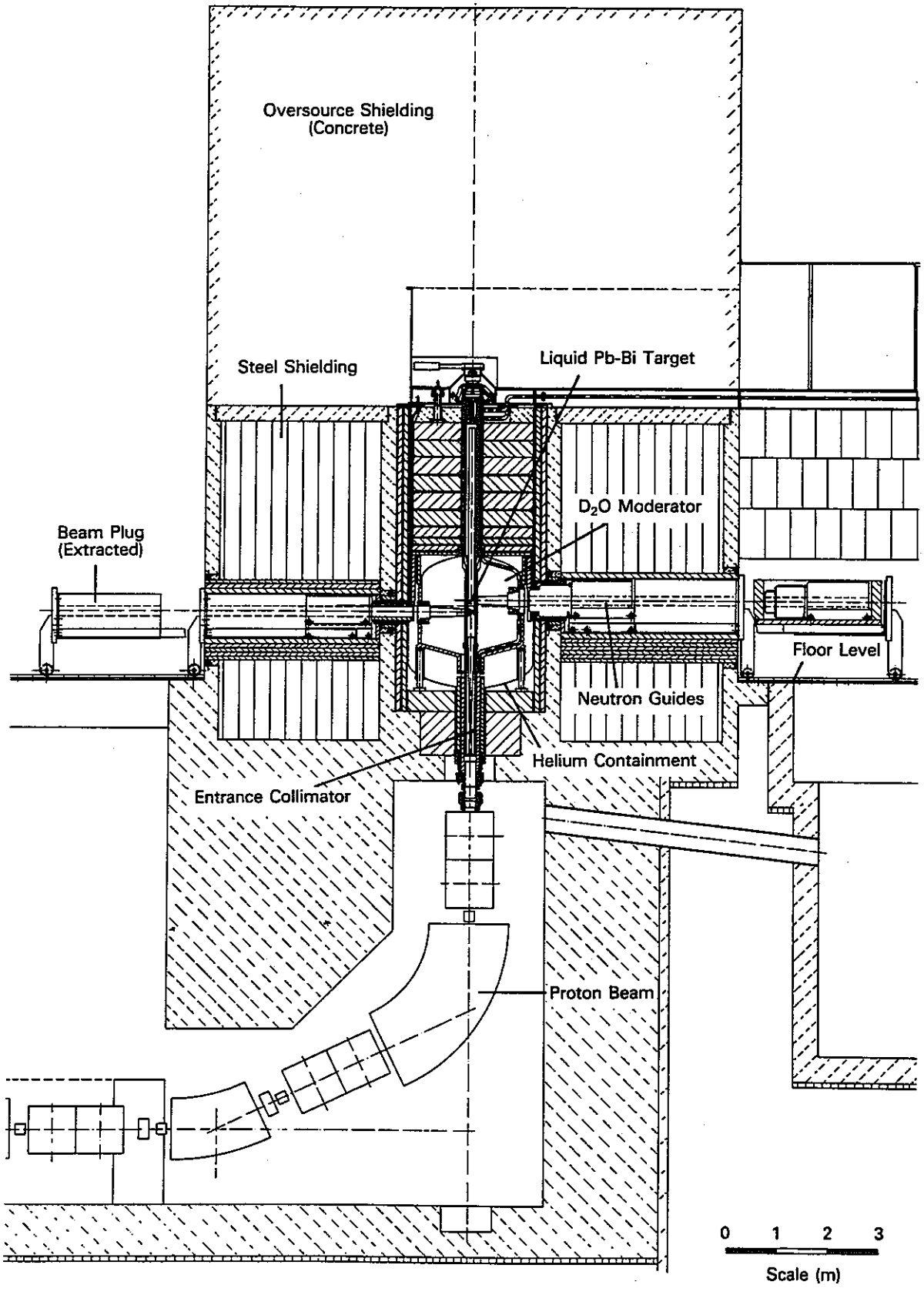


Fig. 1. Vertical cross section of the SINQ neutron source.

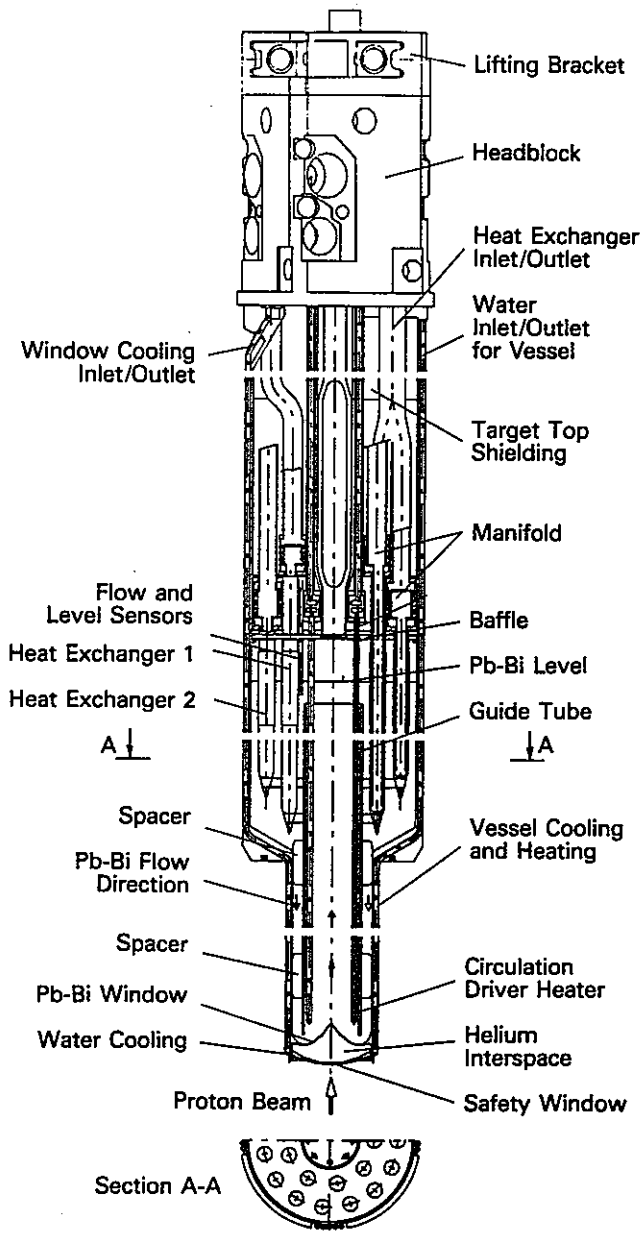


Fig. 2. Vertical cross section of the SINQ target.

toward investigating the heat transfer characteristics only. To the authors' best knowledge, only a group in Israel is constructing a natural-circulation loop using liquid metal[8] (LBE). It is a closed-loop-type configuration, and flow is driven by gas injection instead of a thermally generated density gradient.

The objective of this paper is to present the concept of a liquid-metal natural-circulation loop in a concentric tube configuration as the primary cooling mechanism of the spallation neutron source target. We applied a one-dimensional model to this configuration, and its thermohydraulic behavior was analytically and numerically studied. The results are given in Sec. II. We also performed two experiments using LBE, one small-scale and the second at half-scale. These results are presented in Sec. III. The feasibility of this concept, considering the overall performance of the target, is also discussed.

## II. ANALYSIS

### *II.A. Analytical Model and Formulation*

The analytical model[9] is illustrated in Fig. 3. The loop consists of two long vertical legs of the same diameter as the guide tube and the height of the target. One leg corresponds to the inside flow channel of the guide tube (inner channel) and the other to the outside annular channel (outer or annular channel). An internally heated region is located at the bottom of one leg, and a heat exchanger is at the top of the other leg. The heat exchanger is simulated by a volumetric heat sink. By assuming a constant flow area over the loop and by neglecting the effects arising from the turns at both ends, the problem becomes one-dimensional with only one velocity component (see Nomenclature on p. 298):

$$V = (0,0,v) \ . \tag{1}$$

The basic equations are the conservation equations of mass, momentum, and energy. Substituting Eq. (1) into the mass conservation equation gives

$$v = v(t) \ . \tag{2}$$

With the Boussinesq approximation, the momentum equation is expressed as

$$\partial v/\partial t + v(\partial v/\partial z) = -1/\rho(\partial p/\partial z) + \nu(\partial^2 v/\partial z^2) + 1/\rho F_z \ , \tag{3}$$

where $F_z$ is the external force or the buoyancy force in this case.

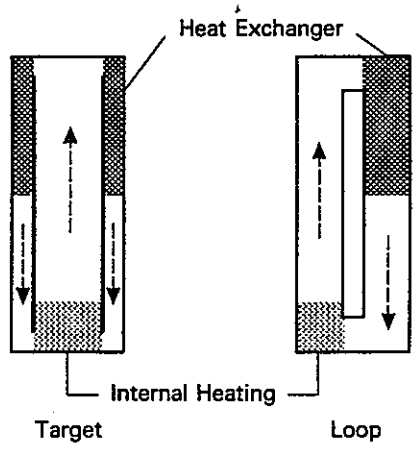


Fig. 3. The analytical model.

From Eq. (2), this is reduced to

$$\partial v/\partial t = -1/\rho(\partial p/\partial z) + 1/\rho F_z \ . \quad (4)$$

The energy equation is

$$\partial T/\partial t + v(\partial T/\partial z) = \alpha(\partial^2 T/\partial z^2) + q \ , \quad (5)$$

where

$$q = \begin{cases} Q & \text{for } 0 < z < h \\ 0 & \text{for } h < z < L \\ -DT & \text{for } L < z < L + l \\ 0 & \text{for } L + l < z < 2L \ . \end{cases}$$

Internal heat generation was assumed to be uniform inside the heated region. The parameter $h$ corresponds to the range of the proton beam rated at 590 MeV (~30 cm), and $D$ is the volumetric heat sink rate, which is described later.

Since the model is a closed loop, a continuity condition has to be satisfied, giving

$$T(0) = T(2L) \ . \quad (6)$$

The initial conditions are

$$T(z,0) = T_s$$

and

$$v(0) = 0 \ . \quad (7)$$

The buoyancy term is expressed as usual:

$$F_z = -\rho g(1 - \beta\Delta T) \ . \quad (8)$$

For the first term on the right side of Eq. (4), a normal pressure drop correlation was used. Thus,

$$dp/dz = -\lambda\rho v^2/2d \ , \quad (9)$$

where $\lambda$ is the frictional coefficient in a smooth tube, and the formulas used are[10]

$$\lambda = \begin{cases} 64/\mathrm{Re} & \text{for Re} < 2000 \text{ (laminar)} \\ 0.3164/\mathrm{Re}^{0.25} & \text{for Re} > 2000 \text{ (turbulent)} \ . \end{cases} \quad (10)$$

To eliminate the static pressure in Eq. (3), the equation was integrated around the loop to give

$$\partial v/\partial t = -\lambda v^2/2d + g\beta/2L \int_0^{2L} (\Delta T)\, dz \ . \quad (11)$$

Therefore, the governing equations are Eqs. (2), (5), and (11). These equations are normalized by using the following normalization scheme:

$$\Theta = (T - T_s)D/Q \ ,$$

$$\tau = tV_s/2L \ ,$$

$$w = v/V_s \ ,$$

$$Z = z/2L \ ,$$

$$\delta = h/2L \ ,$$

and

$$\gamma = l/2L \ , \quad (12)$$

where $V_s = 2DL$ is the characteristic velocity.

Finally, the governing equations in nondimensional form appear as

$$\partial\Theta/\partial\tau + w(\partial\Theta/\partial Z) = \alpha/(2DL^2)\partial^2\Theta/\partial Z^2 + q' \ , \quad (13)$$

where

$$q' = \begin{cases} 1 & \text{for } 0 < Z < \delta \\ 0 & \text{for } \delta < Z < \frac{1}{2} \\ -\Theta & \text{for } \frac{1}{2} < Z < \frac{1}{2} + \gamma \\ 0 & \text{for } \frac{1}{2} + \gamma < Z < 1 \end{cases}$$

and

$$\partial w/\partial\tau = -\lambda L w^2/d + Qg\beta/2D^3L \int_0^1 \Theta\, dZ \ . \quad (14)$$

### *II.B. Theoretical Analysis*

A closed-form solution for the steady state can be obtained when the axial heat conduction term in Eq. (13) is neglected. The equations then become

$$w(d\Theta/dZ) = q' \quad (15)$$

and

$$-\lambda L w^2/\delta + Qg\beta/2D^3L \int_0^1 \Theta\, dZ = 0 \ . \quad (16)$$

With a boundary condition of continuity in temperature at every boundary of the regions in a loop, solutions of Eq. (15) are obtained as follows:

$$\Theta = Z/w + C_1$$
$$= Z/w + d\exp(-\gamma/w)/w[1 - \exp(-\gamma/w)] \ , \quad 0 < Z < \delta \ ;$$
$$C_2 = \delta/w[1 - \exp(-\gamma/w)] \ , \quad \delta < Z < \tfrac{1}{2} \ ;$$
$$C_3\exp(-Z/w) = \delta/w\exp(-\tfrac{1}{2}w)[1 - \exp(-\gamma/w)] \ , \quad \tfrac{1}{2} < Z < \tfrac{1}{2} + \gamma \ ;$$

and

$$C_4 = \delta\exp(-\gamma/w)/w[1 - \exp(-\gamma/w)] \ , \quad \tfrac{1}{2} + \gamma < Z < 1 \ . \quad (17)$$

The temperature increases linearly in the heated region, decreases exponentially in the cooling region, and is constant in other regions. Figure 4 illustrates the temperature distribution of Eq. (17).

By substituting these temperature results into Eq. (16), one obtains

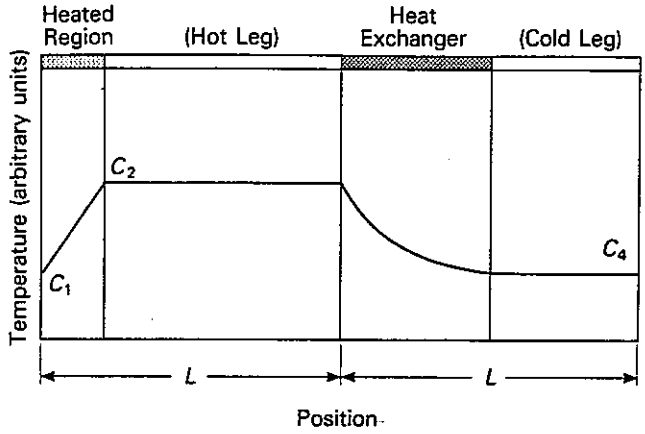


Fig. 4. Analytical temperature distribution: Eq. (17).

$$-\lambda L w^2/\delta = Qg\beta/2D^3L\{\delta(1-\delta)/2w - \delta + \delta\gamma\exp(-\gamma/w)/ w[1-\exp(-\gamma/w)]\} \ . \quad (18)$$

The steady-state velocity value can be evaluated by solving this nonlinear algebraic equation.

We examined extreme cases as examples. If $\gamma/w < 1$ (the target is sufficiently long), the following relationship is obtained for the steady-state velocity:

$$w^3 \to Qg\beta\delta(1-\gamma)/4D^3L \ ; \quad v \to Q^{1/3} \ . \quad (19)$$

This tells us that the steady-state velocity is roughly proportional to the $\frac{1}{3}$ power of the beam power. The maximum temperature in the system is

$$\Theta_{max} = C_2 \to \delta/\gamma \ ; \quad T_{max} \to Qh/DL \ . \quad (20)$$

We see that this is linearly proportional to the input power but inversely proportional to $D$ and $L$.

The temperature difference in the system is

$$\Delta\Theta_{max} = C_2 - C_4 \to Q^{-1/3} \ ; \quad \Delta T_{max} \to Q^{2/3} \ . \quad (21)$$

This agrees with the results of the preliminary analysis.[11]

The volumetric heat sink rate is obtained from the heat exchanger characteristics based on the total amount of heat transfer:

$$UST/\rho C_p V = DT \ , \quad (22)$$

where

$U$ = average overall heat transfer coefficient

$S$ = total heat transfer area

$\rho$ = density of LBE

$C_p$ = specific heat of LBE

$V$ = volume of the shell of heat exchanger.

From this, we estimate $D$ to be

$$D = 2Urn/\rho C_p R_b^2 \ , \quad (23)$$

where

$r$ = radius of the heat exchanger tube

$n$ = number of tubes

$R_b$ = radius of the loop.

For a set of representative numerical values of the actual target ($U = 0.1$ W/cm$^2$·K, $r = 1.5$ cm, $R_b = 5.5$ cm, $n = 30$, $\rho = 10.5$ g/cm$^3$, $C_p = 0.15$ W·s/g·K), we calculated $D$ to be 0.19/s.

The solution of Eq. (18) is shown in Fig. 5 with dimensions of $L = 350$ cm, $h = 30$ cm, and $l = 200$ cm. The maximum temperature was calculated as $C_2$ with corresponding velocity values. It shows the $\frac{1}{3}$ power law dependence of velocity $V_{sta}$ as in Eq. (19) and a linear proportionality for the maximum temperature $T_{max}$ as Eq. (20).

### *II.C. Numerical Calculations*

#### II.C.1. Simple Tube Loop

The governing equations, Eqs. (13) and (14), were solved numerically in order to study the time-dependent behavior of the loop and the effect of axial heat conduction. A backward differencing formula was used for the space derivatives and forward differencing for the time derivative. Simpson's formula was employed to evaluate the integral in Eq. (14). The mesh number was taken as 100, and the time step was 0.01 (in dimensionless units) for all computations.

Figure 6 shows calculated time-dependent temperature distributions. After a sudden heat addition (as seen in Fig. 6a), the heated region shows a temperature increase with a flat distribution because the velocity is

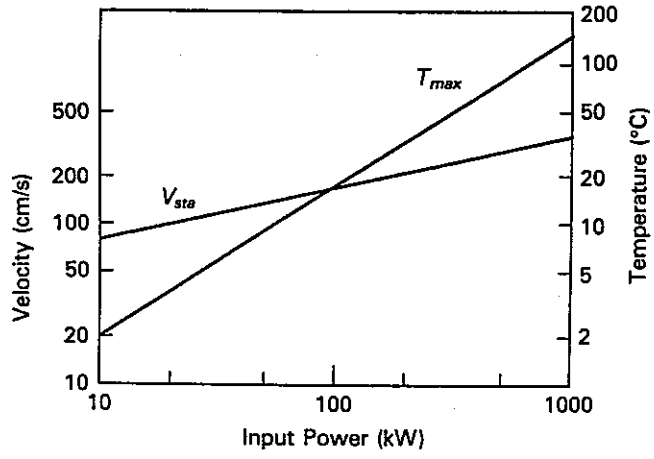


Fig. 5. Dependence of the steady-state maximum temperature difference $T_{max}$ and velocity $V_{sta}$ on input power.

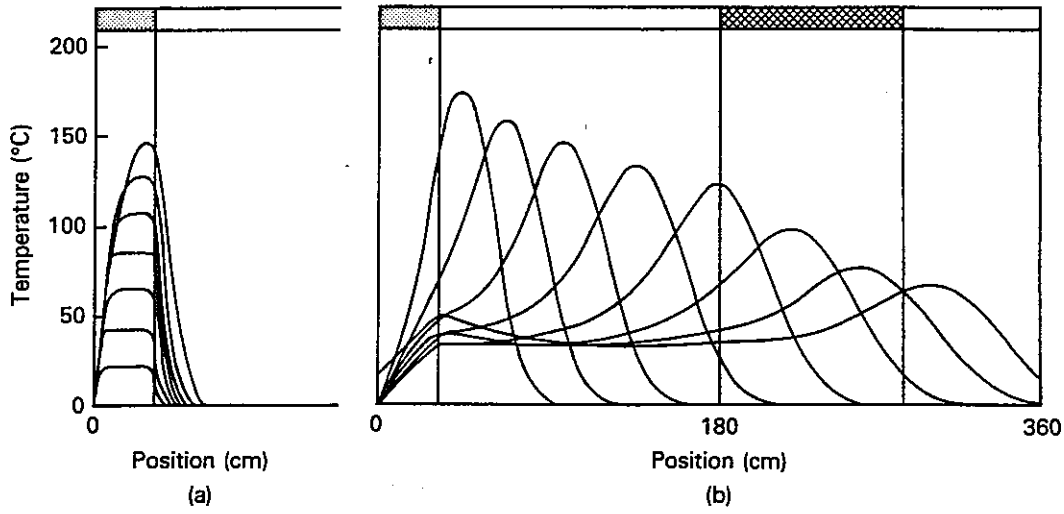


Fig. 6. Time change of temperature distribution ($L = 180$ cm, $l = 100$ cm, 100 kW): (a) $0.25 < t < 1.75$ s and (b) $2.5 < t < 6$ s.

still small. However, it can be seen that this distribution moves slowly upward, and deformation of the flat distribution begins because of the increasing velocity. During this period, the maximum temperature in the system lies in the heated region. In Fig. 6b, the velocity becomes relatively large, and the heated liquid is transported rather efficiently. At the same time, in the region without heating, deformation of the distribution continues only slowly because of the heat conduction. The velocity value increases during this time, and this might be called the accelerating phase. When the heated liquid enters the heat exchanger region, the deformation is accelerated, and maximum temperature drops faster. At this time, the distribution in the heated region shows a nearly linear increase, while it is approximately constant in the nonheated region. The liquid initially heated cannot be completely cooled down, and it returns to the heated region at a higher temperature. The velocity value decreases up to this point, and this is called the decelerating phase. These are the characteristic trends of the time-dependent temperature distribution during the first cycle of circulation. In the second cycle, a similar behavior is observed. However, since the velocity is already developed, the temperature increase in the heating region is not as large, and this results in a smaller increase in the velocity.

This circulation pattern is one of an oscillating nature in both velocity and the maximum temperature, as shown in Fig. 7. In the temperature history, there is a very large and sharp overshoot during the first cycle. After this overshoot, a drop occurs when the cold liquid flows in from the outer leg. The central value of this oscillation increases gradually, and the oscillation damps out, leading to the steady state. The velocity also shows a similar oscillatory behavior but does not show a sharp overshoot. The difference between the two during one cycle is that the temperature has some flat but slightly decreasing period on its upper envelope, while the velocity changes continuously. This is because the maximum temperature lies in the nonheated region above the heated region, where the small temperature change is mainly due to the heat conduction. However, the liquid is continuously accelerated.

The temperature distribution for the steady state is shown in Fig. 8. It shows a linear increase in the heated region, an exponential decrease in the heat exchanger region, and a nearly flat distribution in the two regions between them. This distribution coincides with the analytical results for the extreme case without heat conduction in the previous section. The maximum temperature is at the outlet of the heated region, and the minimum temperature, as expected, is at the outlet of the heat exchanger. A slight decrease is seen in the upper part of the inner channel (above the heated region)

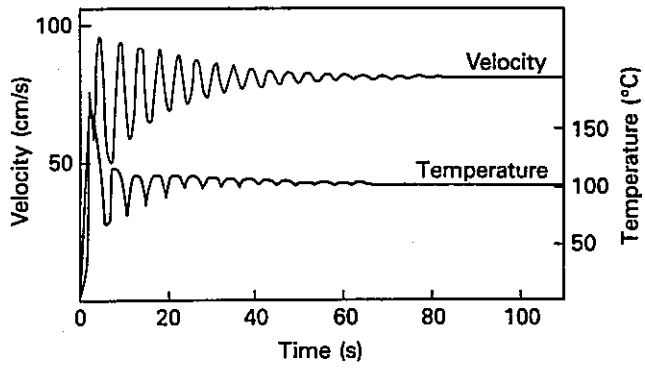


Fig. 7. Time histories for the highest temperature and the average velocity.

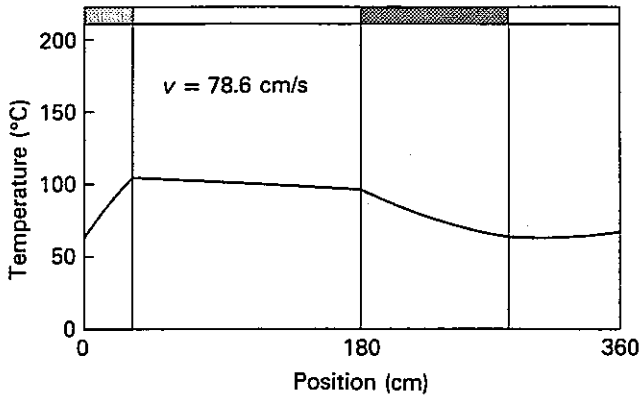


Fig. 8. The steady-state temperature distribution ($L$ = 180 cm, $l$ = 100 cm, 100 kW) at 46 s.

and an increase in the lower part of the outer channel (below the heat exchanger). They are due to axial heat conduction and account for the difference from the analytical results given in Fig. 4.

A series of computations was made for the actual target size for input powers of 100, 200, 500, and 1000 kW. Temperature distributions and oscillatory behavior similar to what was described earlier were observed. The results lie on the curves given in Fig. 5. The maximum temperature shows a linear proportionality and the velocity shows a power dependence to $\sim\frac{1}{3}$ power on the input power. This result indicates that the effect of the axial heat conduction is small.

### II.C.2. The Effect of the Pressure Loss at the End Turns

It may be expected that the pressure drop from the U-bend at the bottom of the target will have a large effect on the flow characteristic. To see this effect, the governing equation, Eq. (14), was modified to

$$\partial w/\partial \tau = -(K + 2\lambda L/d)\, w^2/2 + 2Qg\beta/D^3 L \times \int_0^1 \Theta \, dZ \ , \qquad (24)$$

where $K$ is an empirical coefficient of the pressure loss produced by geometry variations such as sudden enlargement, contraction, and bends.[12] Here, it is taken as $K = 2.86$. This value is several times larger than that for the smooth tube pressure loss (the second term in the parentheses) for the dimensions of the actual target.

Numerical calculation including this effect [solution of Eq. (24)] showed that the general oscillatory behavior in the time-dependent variation of the velocity and the maximum temperature is similar to that without this effect. However, the period of oscillation became longer because the development of velocity is slowed by a larger pressure loss. Figure 9 shows the steady-state velocity and maximum temperature with respect to the input power. Compared with the case without the U-bend pressure loss, the steady-state velocity $V_{sta}$ is lower, and this results in a higher maximum temperature. In the case of the full target with 1-MW power input, the differences in comparison are ~44 cm/s smaller in velocity and 11°C higher in maximum temperature without turning loss.

## III. EXPERIMENT

### *III.A. Experimental Facility*

Figure 10 shows an illustration of the experimental facility prepared for the liquid-metal experiments. It consists of test sections for the Small-Scale Experiment (SSE), the scaled-down mockup (MUP) experiment, and a water loop common to both the SSE and MUP. The SSE has two identical test sections; one is for thermohydraulic testing and the other for corrosion testing. The dimensions of the test sections are given in Table I together with those of the actual SINQ target. The water loop used for cooling maintains an outlet (supplying) temperature of 130°C and a maximum inlet (returning) temperature of 200°C (16 bars). The maximum cooling capacity is designed to be 200 kW. Each test section has its own LBE reservoir tank, and LBE is always stored and frozen in this tank. The LBE is transported to the test sections by pressurization of the reservoir tank.

#### III.A.1. Small-Scale Experiment

The SSE was intended for gaining experience in handling liquid metal, and as such, the configuration and instrumentation were assembled in a one-dimensional sense. That is, the heat was added from outside the container at the bottom, and the heat exchanger was set inside the guide tube at the top. Although this configuration is topologically opposite to the real

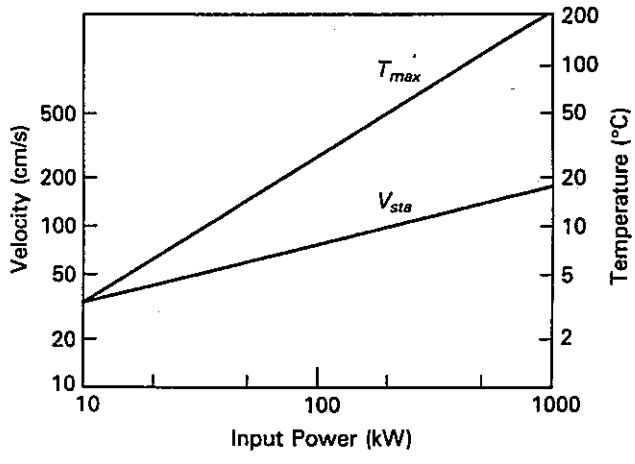


Fig. 9. Performance of the SINQ target: highest temperature and average velocity at steady state.

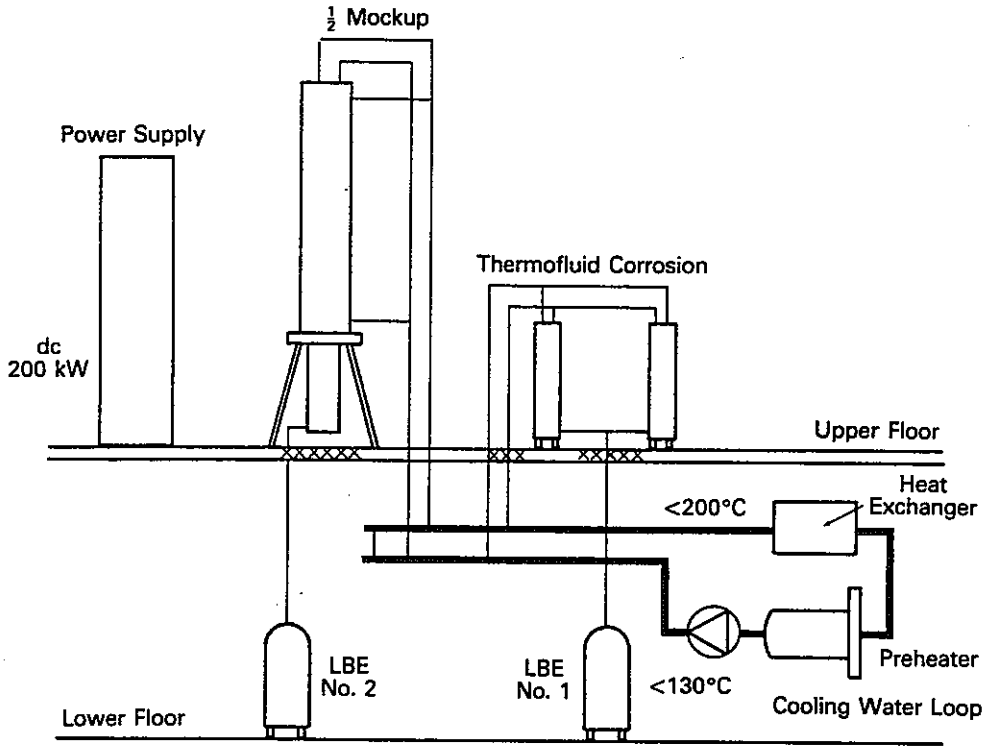


Fig. 10. Schematic of the SSE facility for thermohydraulic dynamics of liquid LBE.

target situation, the expected one-dimensional thermohydraulic behavior is expected to be identical. The container and other structural materials were made of a high-temperature steel, DIN 1.7335. The guide tube is quartz glass of 2-mm wall thickness. The heating block consists of 16 heater pins (900 W for each) embedded in a copper block that surrounds the outer container. The maximum heating power available is 14.4 kW. The heat exchanger is a coaxial tube type where inlet water flows inside the inner tube and flows out in an annular gap. The outside tube is made of the same material as that of the container, and the inner tube is of stainless steel. It has an 18-mm outer diameter and is 37 cm long. Four of these heat exchanger tubes are positioned at the upper part of the container on the top flange and inside the guide tube. The system was monitored at 16 points for temperature, 2 for pressure, 2 for LBE levels, and 1 for mass flow rate of cooling water. As for experimental measurements, 46 thermocouples were installed to measure the vertical temperature distribution.

### III.A.2. Mockup Experiment

This facility is a scaled-down mockup geometry for two-dimensional temperature distribution measurements, as shown in Fig. 11. The scaling factor is ½. The

TABLE I

Dimensions of Scaled Test Sections and Actual Target

| | SSE | MUP | SINQ |
|---|---|---|---|
| Diameter | | | |
| Lower | 133.3 | 96 | 180 |
| Upper | | 134.5 | 370 |
| Height | 885 | 1701 | 3340 |
| Guide tube diameter | 100 | 64 | 123 |
| LBE inventory (ℓ) | 11 | 12 | 160 |
| Maximum power (kW) | 20 | 200 | 650 |
| Heating method | Heaters outside container | Heaters inside guide tube | Proton beam |

outer container has different diameters for the lower and the upper portions, and the inner heat exchanger is placed at the upper location, while the inner diameter of the guide tube is constant. All structural materials were the same as that used for the SSE. Heat was supplied at the bottom of the inner channel with 12 specially fabricated heater pins affixed to a bottom flange. The maximum heat input with all pins was designed to be 200 kW. The heat exchangers are of the annular shell type for both the inner and the outer cooler. The lower part of the test section is insulated to approximate an adiabatic condition for heat transfer. For measuring temperature distributions, 196 thermocouples are installed in the test section. The system is monitored with a separate system that measures temperatures with 28 thermocouples, pressure at the upper open space, LBE levels, and mass flow rate of cooling water.

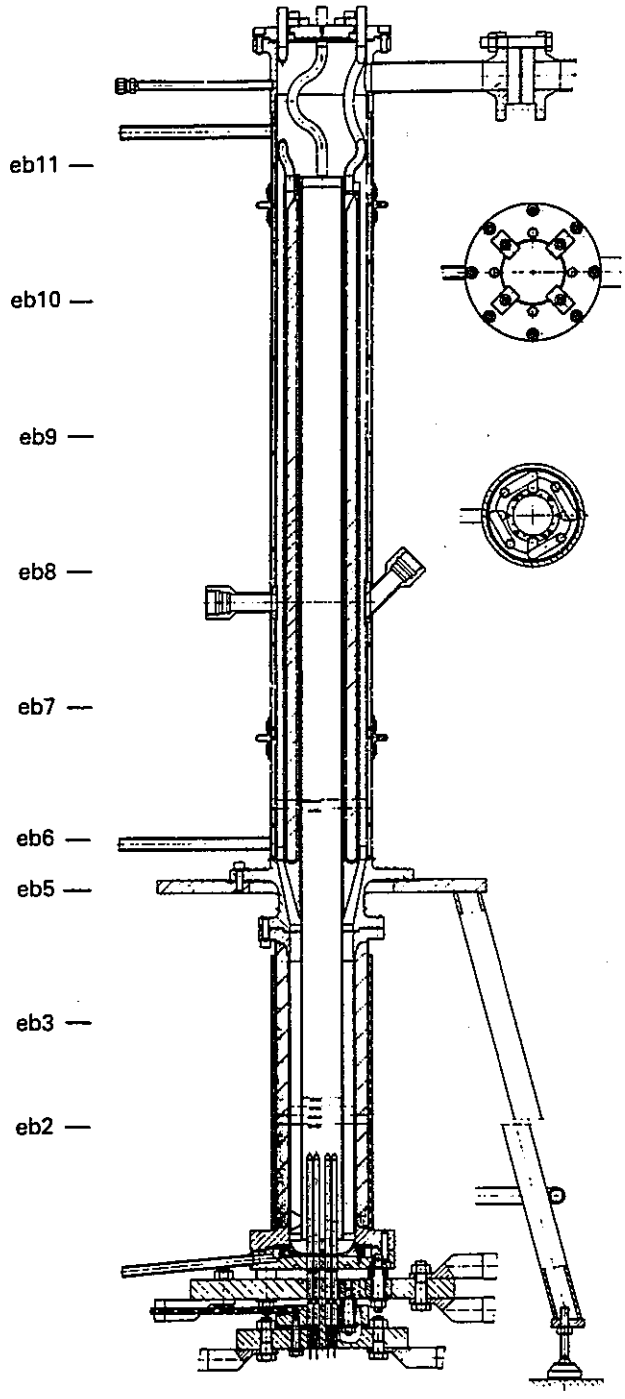


Fig. 11. Detailed schematics of the MUP. The eb numbers show the approximate heights of the temperature measurement. See Fig. 14 for the exact positions.

### III.A.3. Operation and Experimental Runs

In both experiments, after the LBE was transported into the test section from the reservoir tank, it was left for several hours without heating in order to establish a stagnant state as the initial condition. Sudden heating was possible only for small heat input into the MUP. This restriction was dictated by the initial sharp temperature rise inside the heater pins. Thus, the transient measurement of the temperature distribution was available only up to 25 kW. For larger power, the input power was gradually increased in small steps. This was also the case for the terminating transient. An abrupt power cut can destroy the heater structure.

Experimental runs were made in the SSE with a fixed input power of 13.8 kW and in MUP by varying the power from 3 to 80 kW. Steady-state measurements were made over 1 to 2 h.

## *III.B. Experimental Results and Discussion*

### III.B.1. Temperature Distribution

#### *III.B.1.a. Vertical Temperature Distribution in SSE*

The average vertical temperature distribution under steady-state conditions in the SSE is plotted in Fig. 12. The general behavior is in good agreement with the one-dimensional prediction. There is a sharp temperature increase in the heated region, a flat distribution above this region, a large temperature decrease in the cooled region, and again a flat distribution below. A very slight discrepancy is observed in the adiabatic region. This is due to the heat conduction in the liquid as verified by a parallel numerical calculation including this effect. In the top region, the distribution is considerably distorted, supposedly because of the existence of the guide tube supporter and some three-dimensional effects.

#### *III.B.1.b. Vertical Temperature Distribution in MUP*

Figure 13 shows the vertical temperature distribution in the MUP at steady state and averaged over radius, angle, and time. The general trend of the distribution

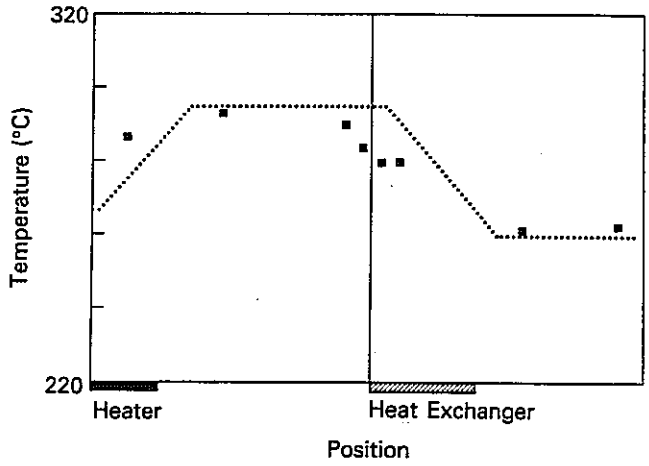


Fig. 12. Measured and calculated temperature distributions in SSE (13.8 kW). For numerical calculations, see Ref. 2.

is in agreement with the analytical prediction, as can also be seen in the SSE. However, several discrepancies have been found. There is a large temperature decrease in the inner channel toward the top. This is considered to be mainly due to the cooling by the internal heat exchanger. A large temperature increase can be seen in the annular channel at the bottom near the heated region. Although a slight temperature increase was seen in the SSE, this increase is much larger in the MUP in this region. The reason for this large temperature increase is the heat transfer through the guide tube wall from the inside to outside. The guide tube material of the MUP has greater thermal conductivity. The heat transfer through the guide tube wall may correspond to the heat deposition in an annular channel due to widening of the beam (see Appendix). It is known from a one-dimensional analysis that this does not affect the bulk velocity of LBE but that it elevates the maximum temperature of the system. These results suggest that further investigation of the effect of the thermal conductivity of the guide tube materials and its structure should be made.

Fairly large temperature fluctuations, which caused a scattering of data points in Fig. 13, were observed at the position just above the heater pins and at the top of the LBE layer. This is likely due to a three-dimensional effect arising from the existence of supporting structures for the heaters and coolers.

### *III.B.1.c. Horizontal Temperature Distribution in the MUP*

Figure 14 shows horizontal temperature distributions at various heights of the test section under steady-state conditions and averaged over angle and time. There is a clear temperature difference between the inner and outer channels at all positions, which is the driving force for the natural circulation. In the lower region below the heat exchanger (eb2 and eb3), the temperature decreases monotonically outward, while in the upper region (eb6 through eb11), it shows a small dip at the wall of the inner heat exchanger. The former clearly indicates heat transfer through the guide tube, and the latter is due to cooling by the internal heat exchanger. The temperature difference between the inner and the outer channels becomes smaller, and the temperature distribution is flatter for the higher positions, which reflects an aspect of the vertical temperature decrease shown in Fig. 13.

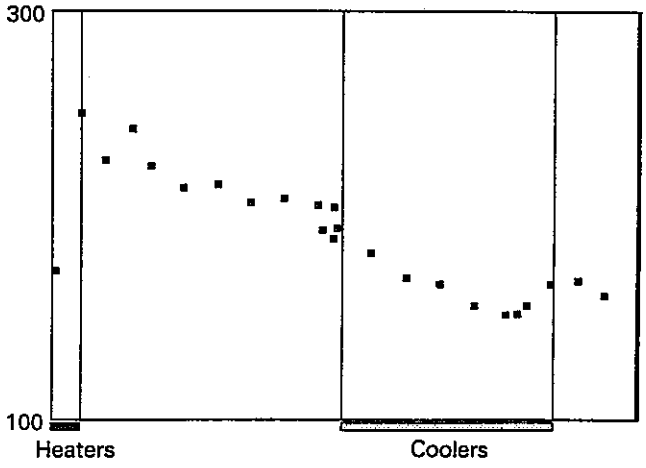


Fig. 13. Vertical temperature distribution in the MUP at 60.5 kW averaged over radius, angle, and time.

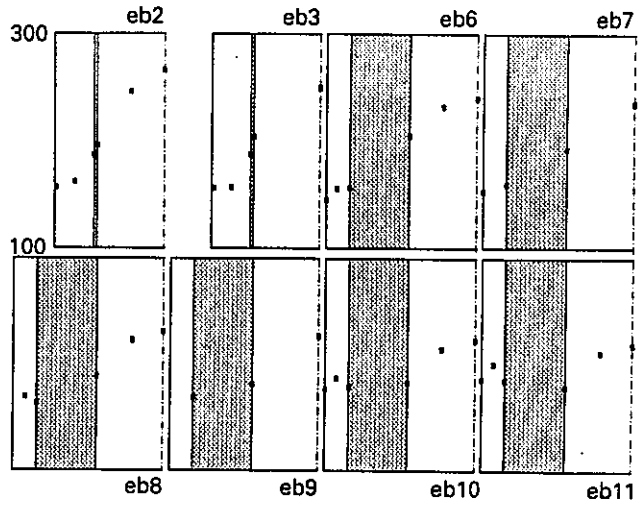


Fig. 14. Horizontal temperature distributions for the same conditions as in Fig. 13. The heights are as follows: eb2 = 18.0 cm, eb3 = 33.5 cm, eb5 = 53.2 cm, eb6 = 60.2 cm, eb7 = 80.2 cm, eb8 = 100.2 cm, eb9 = 120.2 cm, eb10 = 140.2 cm, and eb11 = 160.2 cm from the bottom.

III.B.2. Thermohydraulic Performances of Target

The thermohydraulic performance was evaluated using the results of the MUP experiment. The maximum temperature difference in the system was estimated from temperatures at 30 cm above the heated region and at a point exiting the cooling region at the outer annular channel. This temperature difference is plotted with respect to the input power in Fig. 15. It shows clearly a power law relationship as predicted by the analysis. The power coefficient is 0.56 ± 0.003, which agrees with the prediction of Eq. (21).

The bulk velocity of the circulating LBE has been estimated from an energy balance of liquid temperature flowing through the heated region and plotted against the input power in Fig. 16. This also shows a very good power law relationship with a power coefficient of 0.32 ± 0.03, while the predicted value is $\frac{1}{3}$ [Eq. (19)].

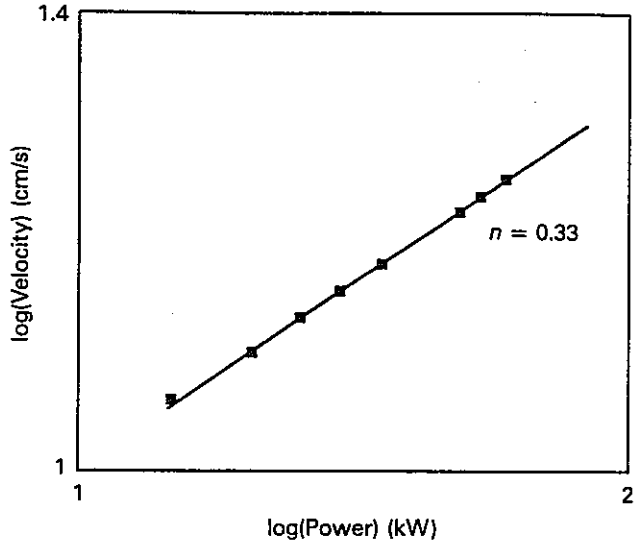


Fig. 16. Target performance: bulk velocity of LBE compared with input power.

## IV. SUMMARY

The SINQ target consists of a natural-circulation loop of liquid lead-bismuth eutectic in a concentric double-tube configuration. The thermohydraulic behavior of this target system has been investigated analytically and experimentally. The analytical model is based on a one-dimensional natural-circulation loop with uniform heat deposition at the bottom and a volumetric heat sink for the heat exchanger at the top. The results of the theoretical and numerical analyses have been experimentally confirmed in two different experiments. The following conclusions were drawn:

1. Analytically, the steady-state velocity is proportional to the $\frac{1}{3}$ power of the beam power, whereas the maximum temperature is linearly proportional to the input power. Numerical calculations and experimental results showed the same proportionalities and confirm the analysis.

2. The effect of the axial heat conduction is small for the steady-state velocity and for the maximum temperature in LBE.

3. A well-established flow was observed at higher velocity levels. For the full-power condition of the actual target, it would be ~160 cm/s.

4. The maximum temperature increase at steady state is ~206°C and below a specified design value of 250°C.

5. The effect of the pressure loss due to the U-bend at the bottom of the loop was studied and found to show a fairly large effect. However, the velocity value is still within a reasonable range, and the maximum temperature is lower than the specified limiting value.

6. The temperature difference in the system at full-power operation is extrapolated to be 244°C. Using another scaling law approach [Eq. (20)], this gives a maximum temperature of ~250°C. Both are below the specified operating temperature of 350 to 400°C.

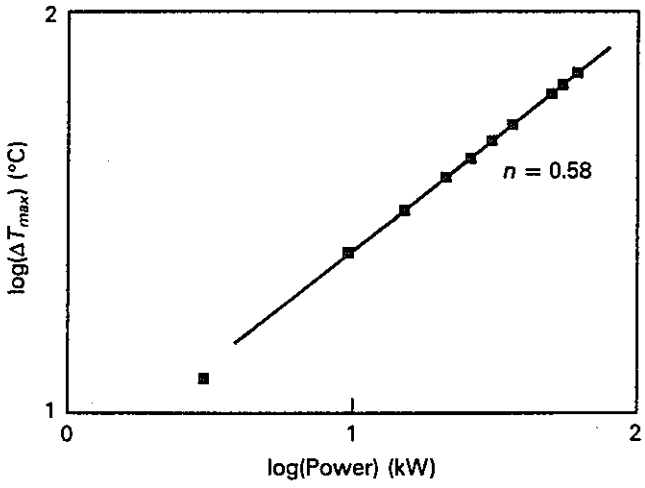


Fig. 15. Target performance: maximum temperature difference in the system compared with input power.

## APPENDIX

### FRACTIONAL ENERGY DEPOSITION OUTSIDE GUIDE TUBE (BEAM SPILL)

Beam size or position may vary slightly because of some instabilities of the operational conditions. Since the proton beam with its heat deposition is the driving force for natural circulation, these variations might

have an influence on the flow behavior. This effect has been studied by assuming that some fraction of energy is deposited outside the guide tube and by modifying the source condition of the basic energy equation.

The dimensionless form of the modified energy equation is

$$\partial\Theta/\partial\tau + w(\partial\Theta/\partial Z) = \alpha/(2DL^2)\partial^2\Theta/\partial Z^2 + q' \ , \tag{A.1}$$

where

$$q' = \begin{cases} f & \text{for } 0 < Z < \delta \\ 0 & \text{for } \delta < Z < \frac{1}{2} \\ -T & \text{for } \frac{1}{2} < Z < \frac{1}{2} + \gamma \\ 0 & \text{for } \frac{1}{2} + \gamma < Z < 1- \\ (1-f) & \text{for } 1 - \delta < Z < 1 \end{cases}$$

and where $f$ is the fraction of the energy deposited inside the guide tube. Here, again by neglecting the heat conduction, a solution in closed form is obtained:

$$\Theta = fZ/w + C_1$$
$$= fZ/w + \delta \exp(-\gamma/w)/ w[1 - \exp(-\gamma/w) - f] \ , \quad 0 < Z < \delta \ ;$$
$$C_2 = \delta/w[1 - \exp(-\gamma/w)] \ , \quad \delta < Z < \tfrac{1}{2} \ ;$$
$$C_3 \exp(-Z/w) = \delta/w \exp(-\tfrac{1}{2}w)\,[1 - \exp(-\gamma/w)] \ , \quad \tfrac{1}{2} < Z < \tfrac{1}{2} + g \ ;$$
$$C_4 = \delta \exp(-\gamma/w)/w[1 - \exp(-\gamma/w)] \ , \quad \tfrac{1}{2} + \gamma < Z < 1 \ ;$$

and

$$(1-f)Z/w + C_5 = (1-f)Z/w + \{\delta/[1 - \exp(-\gamma/w)] - 1 + f(1-\delta)\} \ , \quad 1 - \delta < Z < 1 \ . \tag{A.2}$$

Substituting this temperature distribution into Eq. (16), one obtains

$$-\lambda L w^2/\delta = Qg\beta/2D^3L\{\delta(1-\delta)/2w - \delta + \delta\gamma \exp(-\gamma/w)/w[1 - \exp(-\gamma/w)]\} \ , \tag{A.3}$$

giving a steady-state velocity value. This equation does not include $f$ as a parameter and is exactly the same as Eq. (18) for the ideal case. This shows that the steady-state velocity is determined only by the total amount of energy deposition and not by its distribution. This may be understood as follows: The total buoyancy force to generate the flow that is balanced by the pressure loss is the difference of the two integrals over the temperature distributions of the inner and the outer regions. Although both integrals become larger because of the higher temperatures, their difference remains the same.

Moreover, the highest and the lowest temperatures in the target, $C_1$ and $C_4$, are also the same. They are determined by the total power and the heat exchanger performance. Only the inlet temperature of the LBE at the bottom window, $C_1$, will be higher, but it results in an increase in the stored heat in the target.

## NOMENCLATURE

$C_p$ = specific heat of LBE
$D$ = volumetric heat sink rate
$d$ = effective channel diameter
$g$ = gravity
$h$ = length of heated region
$K$ = geometrical correction factor for pressure drop
$L$ = target height
$l$ = length of heat exchanger
$p$ = pressure
$Q, q$ = uniform volumetric heat deposition
Re = Reynolds number
$S$ = total heat transfer area of heat exchanger
$T$ = temperature
$T_s$ = initial temperature
$t$ = time
$U$ = average overall heat transfer coefficient of heat exchanger
$V, v$ = velocity
$V_s$ = characteristic velocity
$w$ = dimensionless velocity
$Z, z$ = space coordinates

*Greek*

$\alpha$ = thermal diffusivity
$\beta$ = thermal expansion coefficient
$\delta$ = dimensionless length of heated region
$\gamma$ = dimensionless length of heat exchanger
$\lambda$ = pressure loss friction coefficient
$\nu$ = dynamic viscosity

$\rho$ = density

$\tau$ = dimensionless time

$\Theta$ = dimensionless temperature

ACKNOWLEDGMENTS

The authors express gratitude to R. Greif of the University of California-Berkeley for helpful discussions on the analysis. The experimental work was prepared and carried out by E. Hofer, U. Bugmann, and M. Haefeli. Their support is deeply appreciated and acknowledged.

REFERENCES

1. W. E. FISCHER, "Status Report of SINQ: A Continuous Spallation Neutron Source," *Advanced Neutron Sources 1988*, D. K. HYER, Ed., AIP Conference Series No. 97, American Institute of Physics (1989).

2. Y. TAKEDA, "Thermofluid Behaviour of the Lead Bismuth Eutectic Target for the Spallation Neutron Source at SIN," *Nucl. Instrum. Methods*, **A237**, 455 (1985).

3. Y. TAKEDA, "The Development Work of the Liquid Lead-Bismuth Target for SINQ," *Proc. 8th Mtg. Int. Collaboration on Advanced Neutron Sources*, July 8-12, 1985, RAL-85-110, Vol. 1, p. 220, Rutherford Appleton Laboratory.

4. A. MERTOL and R. GREIF, "A Review of Natural Circulation Loops," *Natural Convection*, p. 699, S. KAKAC, Ed., Hemisphere Publishers, New York (1985).

5. R. GREIF, "Natural Circulation Loops," *J. Heat Transfer*, **110**, 1243 (1988).

6. N. SEKI et al., "Single Phase Heat Transfer Characteristics of Concentric Tube Thermosyphon," *Wärme- und Stoffübertragung*, **14**, 189 (1980).

7. J. L. STEIMKE, "Natural Convection Heat Transfer for a Concentric Tube Thermosiphon," *J. Heat Transfer*, **107**, 583 (1985).

8. S. LESIN, Ben-Gurion University of Negev, Private Communication (1989).

9. Y. TAKEDA and W. E. FISCHER, "Thermohydraulic Behavior of the SINQ Target," presented at Int. Symp. Natural Circulation, Boston, Massachusetts, December 13-18, 1987.

10. E. N. PEARSON and H. MOORE, "Intermediate Heat Exchangers," *Sodium-NaK Engineering Handbook*, Vol. II, O. J. FOUSTER, Ed., Gordon and Beach (1976).

11. C. TSCHALAER, "Vertical, Convective Spallation Target at SIN," *Proc. 5th Int. Mtg. Collaboration on Advanced Neutron Sources*, June 22-26, 1981, p. 575, Kernforschungsanlage Jülich (1981).

12. Y. TAKEDA, "A Natural Circulation Loop as a Target," *Proc. 9th Int. Mtg. Collaboration on Advanced Neutron Sources*, September 22-26, 1986, p. 259, Swiss Institute of Nuclear Research.

付録-14

**Thermofluid behavior of the lead bismuth eutectic target forthe spallation neutron source at SIN**

Nuclear Instruments and Methods in Physics Research A237 (1985) 455–463
North-Holland, Amsterdam



# THERMOFLUID BEHAVIOUR OF THE LEAD BISMUTH EUTECTIC TARGET FOR THE SPALLATION NEUTRON SOURCE AT SIN

Yasushi TAKEDA

*Schweizerisches Institut für Nuklearforschung, CH-5234 Villigen, Switzerland*

Received 30 August 1984 and in revised form 7 January 1985

The thermofluid behaviour of a Pb–Bi eutectic (LBE) target for a spallation neutron source have been studied numerically, in order to investigate the effects of (1) target height, (2) beam power, (3) beam radius and (4) adiabatic side walls on the behaviour of natural convection. The results show that within the parameter values studied, the natural convection of target fluid is stabilized and the temperature distribution is not complicated. There is a steep temperature gradient only in a boundary layer region. In the core region the temperature distribution is relatively smooth. It can be expected that the cooling mechanism using natural convection in a vertical target with proton beam entering from below is feasible.

## 1. Introduction

The spallation neutron source under design at SIN is to use 1–2 mA of 590 MeV protons; this leads to a target power of the order of 1 MW and a power density in the region of 1–2 kW/cm$^3$. In order to avoid sophisticated engineering to process such a high power density, the design concept for the target is to use a vertical cylinder of liquid LBE with the proton beam entering from the bottom, and exploit natural convection as the primary heat transfer mechanism inside the target. From a mechanical point of view, this has several advantages such as:

a) no radiation damage and corrosion of the target metal,
b) minimal structural material in the beam region,
c) low operating temperature,
d) remote location of the first heat exchanger from the beam region.

Since natural convection is used as a primary heat transfer mechanism in the target, the thermofluid dynamics of the target LBE is one of the most important study subjects for a practical design. The thermofluid behaviour should exhibit the following characteristics; a simple profile of temperature distribution and of a stable flow effective to heat transportation at the stationary state from the viewpoint of monitoring and control, and a weak transient behaviour for any changes of beam conditions from the viewpoint of operation and safety.

For natural convection in enclosure, generally, it is emphasized [1] that the temperature field is divided into two regions of "core" and "boundary layer" which entirely surround the core. In a vertical cylindrical system like the SIN target, this "core" is an annular region which is surrounded by the "boundary layers" on wall, bottom, ceiling and a center line. As these two regions interact strongly with each other, the boundary layer theory cannot be applied to the problem and solving the basic equations requires more careful treatment than for the problems in other configurations than in enclosure.

The purpose of this work is to clarify the effects of several difficulties which are intrinsic in our problem such as high aspect ratio or distributed internal heat generation on the thermofluid behaviour of the target liquid.

## 2. Calculations

### *2.1. Assumptions*

In formulating the problem, the following assumptions were adopted:

1) All the physical phenomena are axisymmetric and the beam profile does not change during irradiation, so that the problem is treated as a two-dimensional system.
2) The flow is laminar.
3) The Boussinesq approximation is valid, that is, all the physical properties are constant except for the density affecting the buoyancy force.
4) The LBE is always molten so as to avoid the moving boundary problem.

The coordinate system adopted here is shown in fig. 1. Only the half plane of the vertical cross section is shown.

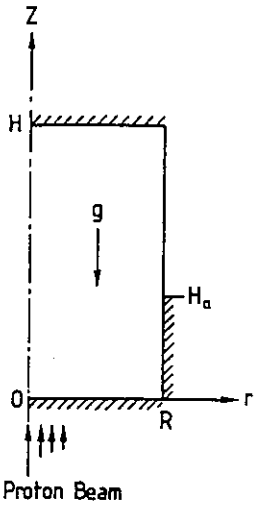


Fig. 1. Schematic of target and coordinate system.

### 2.2. Basic equations

The basic equations are the coupled partial differential equations of continuity, momentum and energy conservation. These are transformed into terms of vorticity by applying the rot-operation and introducing the stream function, and then expressed in dimensionless form by normalization (see appendix) to give:

$$\frac{\partial \Omega}{\partial t} + rV_r\frac{\partial \Omega}{\partial r} + \gamma V_z\frac{\partial \Omega}{\partial z} - \gamma V_r\frac{\Omega}{r} = \mathrm{Pr}\left[-\frac{\gamma\Omega}{r^2} + \frac{\gamma}{r}\frac{\partial \Omega}{\partial r} + \gamma\frac{\partial^2\Omega}{\partial r^2} + \frac{1}{r}\frac{\partial^2\Omega}{\partial z^2}\right] - \mathrm{Pr}^2\,\mathrm{Gr}\frac{\partial T}{\partial r}; \tag{1}$$

$$\frac{\partial T}{\partial t} + \gamma V_r\frac{\partial T}{\partial r} + \gamma V_z\frac{\partial T}{\partial z} = \frac{\gamma}{r}\frac{\partial T}{\partial r} + \gamma\frac{\partial^2 T}{\partial r^2} + \frac{1}{\gamma}\frac{\partial^2 T}{\partial z^2} + \Phi; \tag{2}$$

$$\Omega = \frac{\gamma^2}{r^2}\frac{\partial \Psi}{\partial r} - \frac{\gamma^2}{r}\frac{\partial^2\Psi}{\partial r^2} - \frac{1}{r}\frac{\partial^2\Psi}{\partial z^2}. \tag{3}$$

where Pr is the Prandtl number and Gr the Grashof number. The stream function is related to the fluid velocities by

$$V_z = \frac{1}{r}\frac{\partial \Psi}{\partial r}, \qquad V_r = -\frac{1}{r}\frac{\partial \Psi}{\partial z}. \tag{4}$$

Through this relationship the continuity equation is automatically satisfied.

### 2.3. Boundary and initial conditions

Boundary conditions for the stream function are given as

$$\Psi = \frac{\partial \Psi}{\partial z} = 0; \quad z = 0, 1 \quad 0 < r < 1; \tag{5}$$

$$\Psi = \frac{\partial \Psi}{\partial r} = 0; \quad r = 0, 1 \quad 0 < z < 1, \tag{6}$$

while the thermal boundary conditions are

$$\frac{\partial T}{\partial r} = 0; \quad r = 0 \quad 0 < z < 1,$$

$$r = 1 \quad 0 < z < H_a; \tag{7}$$

$$T = 0; \quad r = 1 \quad H_a < z < 1; \tag{8}$$

$$\frac{\partial T}{\partial z} = 0; \quad z = 0, 1 \quad 0 < r < 1, \tag{9}$$

where $H_a$ is the length of the adiabatic surface (uncooled part of the boundary) as defined in fig. 1.
Since vorticity boundary conditions cannot be given, they are approximated with the values at the next inside grid points and corrected by iteration.

Initial conditions were determined from the assumption of having a quiescent liquid with a uniform temperature

$$V_r = V_z = \Psi = \Omega = T = 0 \quad \text{at } t = 0. \tag{10}$$

Most of the calculations were carried out with the boundary condition of constant temperature on the full length of the side wall (conducting wall, $H_a = 0$).

### 2.4. Profile of heat generation

As the only driving force for the fluid motion of the target liquid is the buoyancy force due to the internal heat generation, and no external temperature difference is applied to the system, the profile of heat generation needs to be approximated fairly well. For these calculations an empirical formula for the volumetric energy deposition [2] was used. The formula is expressed as

$$q(r, z) = \frac{5.7\times 10^6 I}{(\sigma_0 + 0.04z)^2}\, e^{-(r/(\sigma_0+0.04z))^2}\, e^{-z/30}, \tag{11}$$

where $r$ and $z$ are the position variables in cm units, $I$ the beam current in A and $\sigma_0$ is the width parameter which was determined experimentally as 1.6 cm.

### 2.5. Numerical calculation

For solving the time dependent equations, eqs. (1)–(3) above, the finite difference technique was used. The normal centred differencing formula was mainly used, but the so-called upwind difference scheme was used for the inertial terms in eqs. (1) and (2). The vorticity and temperature equations were solved by the alternating directional implicit (ADI) method and the stream function equation by the successive overrelaxation method (SOR). Since all the boundary values cannot be given at a certain time level simultaneously, the values of the preceding time level were used and for correcting this approximation, some internal iterations were carried out. Furthermore, to take account of the nonlinearity of the basic equations, another iteration was performed.

These internal iterations were terminated when maximum changes of the values decreased to 0.1%. The total iteration with respect to time was terminated when the maximum change of the stream function decreased to 0.1% of the value at the preceding time level.

From the preliminary runs to determine the optimal time step, numerical stability of the ADI method was found to depend on the beam power; the higher the beam power, the smaller the time mesh required. The time step was kept constant in any one computational run. For the different beam powers, however, it had to be varied from $1 \times 10^{-5}$ to $1 \times 10^{-6}$ (dimensionless) as for the beam power.

In order to determine the number of grid points, several trial computations were also performed for the highest beam power and the largest aspect ratio, using grid points of $20 \times 20$, $40 \times 40$ and $80 \times 80$. The results showed sufficiently similar profiles of transient temperature field and stream lines for $40 \times 40$ and $80 \times 80$. Hence $40 \times 40$ grid points were used in the series of computations.

### 2.6. Calculations

A series of calculations has been performed in order to investigate the effects of target height, beam power, beam radius and adiabatic side walls. For the adiabatic side walls, two sets of calculations were carried out, one with constant height of target but changing the height of the adiabatic wall, the other with a constant height of the adiabatic wall but changing the target height. The parameters of this series of calculations are tabulated in table 1. The run of 150 cm height and 0.1 mA current without adiabatic side wall is referred to as the standard case.

The results are presented as two-dimensional contour maps of stream function and temperature in the same frame as fig. 1. Since the figures are drawn with the same aspect ratio, the radial components of distributions are exagerated. The outermost contours for both temperature and stream function correspond to the lowest values ($= dT$ and $d\Psi$) for the maps. These values are also used as the interval between the lines. Explicit values of $dT$ and $d\Psi$ are given in figure captions.

## 3. Results and discussion

### 3.1. Development of circulation

Fig. 2 shows the transient temperature distributions and stream line fields for the standard case. It shows clearly the process of generation and growth of circulation (a–m). At (a), a clockwise circulation starts in the lower portion of the liquid where most of the energy is deposited. As time proceeds, the circulation grows (the number of contour lines increases) and the center of the roll rises (a–g). When this roll reaches the top, it grows rapidly (h). A second roll appears (k), grows and moves downwards elongating the total circulation (k–p). The coexistence of these two rolls lasts until the second reaches the bottom, when they both merge into the total circulation (p–t), giving a stable laminar flow by time step (x). The distributions of temperature follow these changes of stream line fields. At first the flow is so small that the temperature distribution is similar to the profile of internal heat generation, but at the bottom part of the distribution a small distortion can be seen since cold liquid flows inward due to the circulation. As time proceeds, this shrinkage spreads upwards, following the rise of the roll, resulting in a vertical hot column around the center line (vertical and parallel contour lines). The presence of a weak secondary roll leads to a slight distortion of the temperature distribution (c–g). A stronger effect can be seen from the first roll in figures (i)–(m). At the top of the container the strong local circulation transports heat horizontally from the central region to the periphery. Following the downward motion of the second roll, the hot liquid column (which is partially cooled at the surface) flows downward, leaving the intermediate region (core) between the central hot column and surface at low temperature (k–p). When the second roll reaches the bottom (q), this core becomes an

Table 1
Parameters for calculations performed in this study

| | Height (cm) | Radius (cm) | Height of adiabatic wall (cm) | Beam profile (cm) | Current (mA) | Effects investigated |
|---|---|---|---|---|---|---|
| A | 75, 150, 300, 450 | 15 | 0 | 5 | 0.1 | Height |
| B | 150 | 15 | 0 | 5 | 0.1, 0.5, 1 | Beam power |
| C | 150 | 15 | 0 | 2.5, 5, 10 | 0.1 | Beam profile |
| D | 150 | 15 | 50, 75, 100 | 5 | 0.1 | Adiabatic side wall |
| E | 150, 225, 300 375, 450 | 15 | 100 | 5 | 0.1 | Adiabatic side wall |

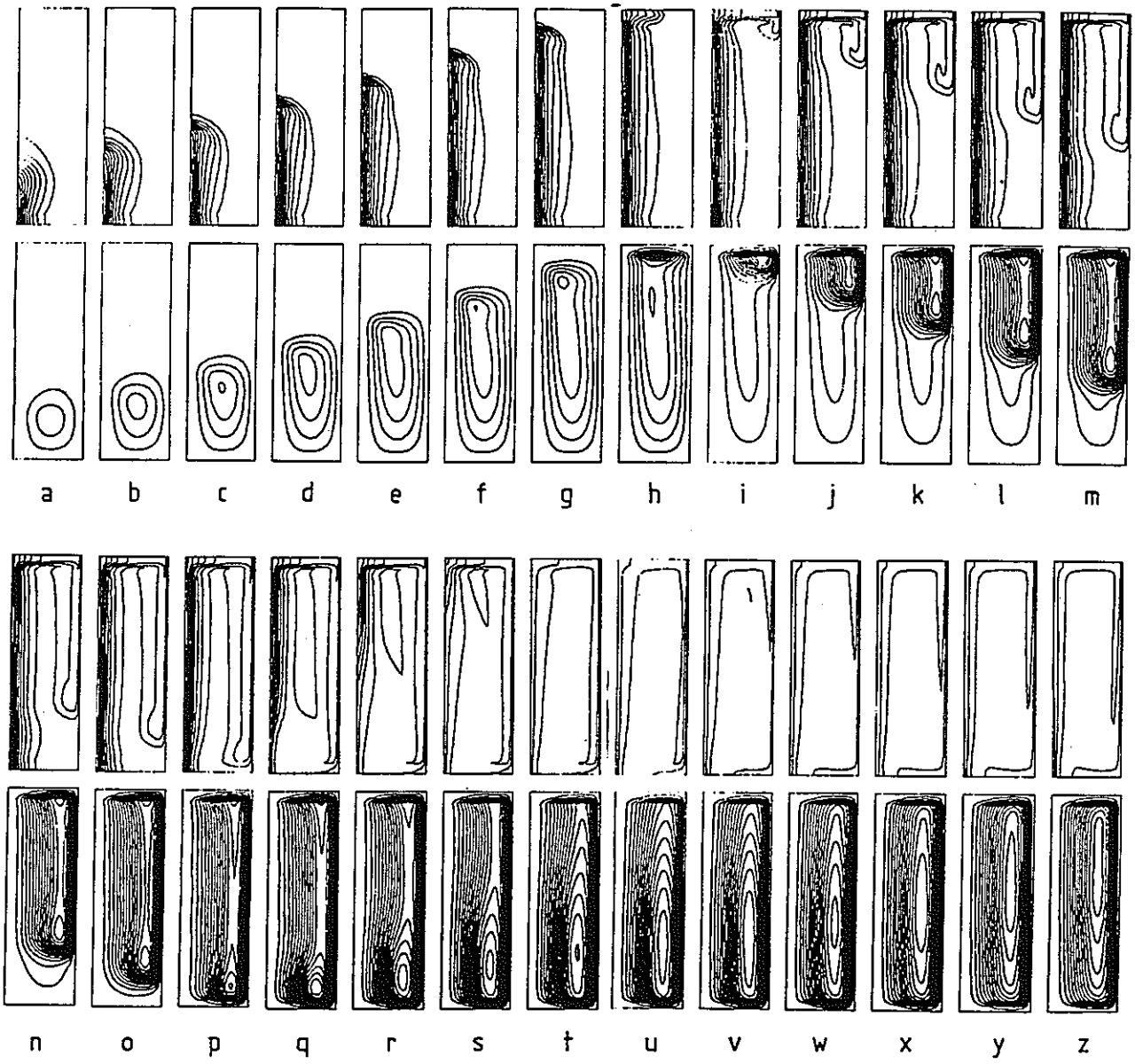


Fig. 2. Transient behaviour for a 150 cm high target. Beam current is 0.1 mA. Contour lines are for $dT = 0.05$ (6.3°C) for all temperature distributions and with $d\Psi = 5$ for stream lines in (a)–(h), 10 in (i)–(z). (a) is at $1.6 \times 10^{-4}$ (5.1 s) and the time interval is $4 \times 10^{-5}$ (1.25 s).

island of lower temperature. During this time when the two rolls are merging and the total circulation is growing, the central hot column is washed away and the position of the maximum temperature moves from the bottom center to the top center (q–t), and a relatively uniform temperature distribution is formed (t–v). However, once the total circulation is established, the heat is accumulated around the center line and forms the central hot column again (x–z). The maximum temperature is also at the bottom center. The high temperature gradient due to the side wall cooling can also be seen. Fig. 3 shows the time behaviour of the maximum temperature in a system (not always located at the same place). The curve can be divided into four sections typical for each stage of the development of circulation mentioned above. They also are illustrated in the figure.

This general aspect of temperature profile and stream line field during transients as well as at the stationary state agrees well with the experimental and numerical investigation by Torrance et al. [3]. Their work was done for natural convection of air in a cylindrical container of unit aspect ratio (but with local heating at the bottom surface) and, in particular, showed the vortex shedding during the transient phase for a high Grashof number system.

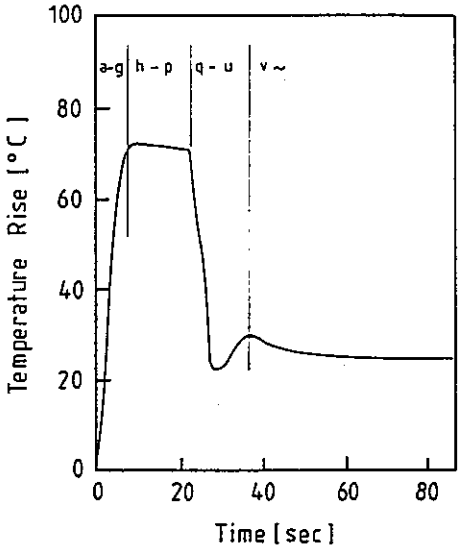


Fig. 3. Time behaviour of maximum temperature in the system. Its position can move from time to time.

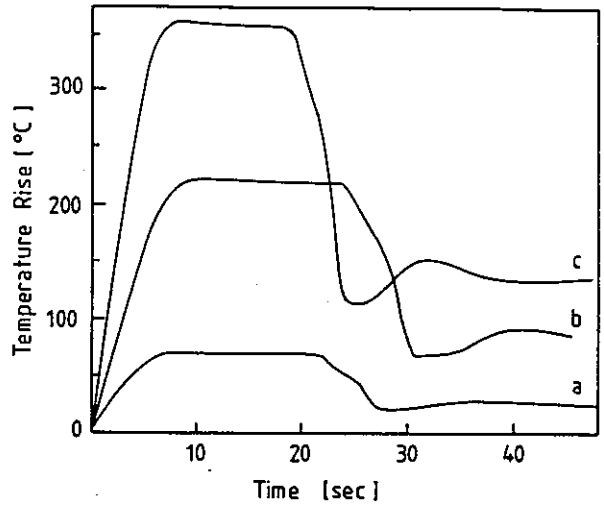


Fig. 5. Time behaviour of the maximum temperature for various beam powers: (a) 0.1 mA, (b) 0.5 mA, (c) 1 mA.

### *3.2. Height*

The effects of target height on the behaviour of temperature distributions and flow patterns have been studied by changing the target height from 75 cm to 450 cm. For all cases calculated, the flow patterns show a single circulation totally inside the target at stationary states, (similar to Fig. 2(z) and referred as a "total circulation") although their centres are not at the same vertical position.

The time behaviour of the maximum temperature is similar to that in fig. 2. The maximum temperature rise above initial temperature (melting temperature, here) for the stationary states is the same for all four cases and about 25°C. The duration of the initial transient is plotted as a function of height in fig. 4 and shows a linear relationship; this is expected since the transient time is proportional to $L/U$ and the characteristic thermal velocity $U(=g\beta R^2\Delta T/\nu)$ does not depend on the target height.

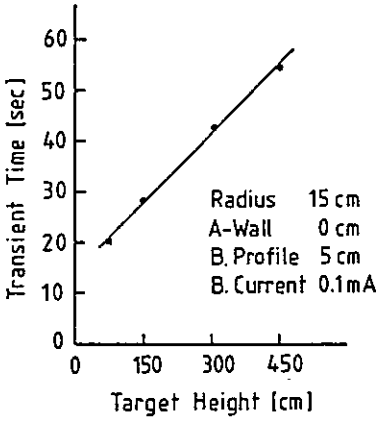


Fig. 4. Transient time vs target height.

### *3.3. Beam power*

The effect of beam power has been studied by calculations with three different beam currents, 0.1, 0.5 and 1 mA (1 mA, 0.6 MW). The flow patterns and temperature distributions are very similar for the three cases and "total circulation" is obtained. The maximum value for the stream function (which corresponds to the maximum volumetric flow rate) increases with the beam current.

The time behaviour of the maximum temperature is shown in fig. 5. The duration of the transient is not strongly influenced by the beam current. On the other hand, the maximum temperature rise increases with beam power, both during the initial transient and at the stationary state. Moreover, the amplitudes of the damped oscillation at the end of the initial transient are larger for higher beam currents. The maximum temperature rise in the stationary state is plotted as a function

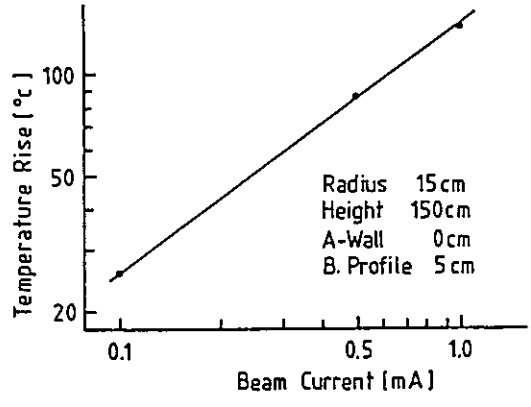


Fig. 6. Power law relationship for the temperature rise in the stationary state with input beam power.

of beam current in fig. 6, and shows a simple power law relationship. The estimate of the exponent is 0.73, which is slightly larger than the value of 2/3 given by a simple one-dimensional analysis [4].

### 3.4. Beam profile

Three calculations were performed for different half-widths of the beam, namely 2.5, 5.0 and 10.0 cm.

All the flow patterns in the stationary states show total circulation. The radial center of the initial circulation moves to larger radii with increased beam size (fig. 7). This implies that the broader beam generates a rising column with larger radius around the center line. However, in the stationary state, the centers are situated at the same radial position. Fig. 8 shows a variation of axial velocity at mid-center with beam radius for the same beam power. A fairly good power law relationship is evident. The estimate of its exponent is 0.6. Simply considering the convection component as a product of velocity $v$ and temperature $T$, it can be assumed to be proportional to the energy deposition density $q$, i.e. $vT \propto q$. Since $T \propto q^{2/3}$ (from the previous section), $v \propto q^{1/3}$, and as $q \propto R^{-2}$, the velocity should be $\propto R^{-2/3}$. This supports the power law relationship in fig. 8.

Fig. 9 shows the development of the temperature distribution for a 10 cm beam. The distribution in the core region has a complicated profile and shows a high temperature island. This high temperature island appears at (400), and it grows and stably exists, until thermal convergence is reached.

Fig. 10 shows the variation of the highest temperature in the target with time for the three cases. The position of the highest temperature is situated at the bottom center for the two narrow beam cases but for the 10 cm beam it is at the center of the high temperature island in the core region mentioned above. The transient time is shorter for narrower beams. This is to be expected, since the transient time is inversely proportional to the characteristic thermal velocity which is proportional to the characteristic temperature. For narrower beams the maximum temperature is higher and shows a larger damped oscillation. Also the end of the initial transient is more clearly marked. This suggests that although narrower beam systems show stronger transient phenomena they may have a higher stability.

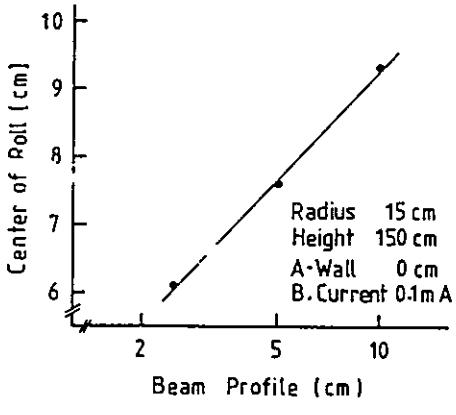


Fig. 7. Positions of the center of circulations at initial stages.

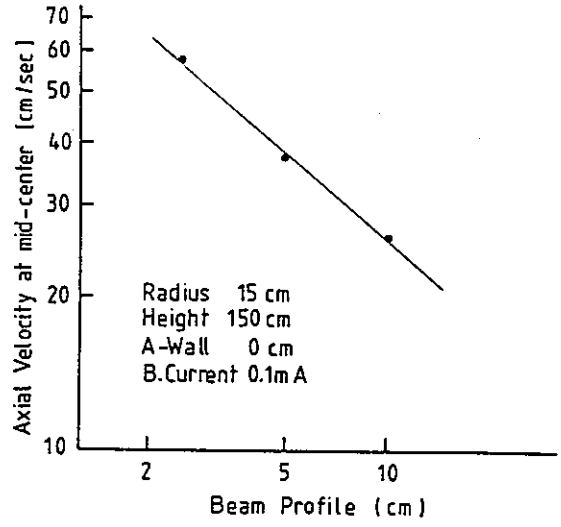


Fig. 8. Axial velocity ($V_z$) at mid-central position vs beam profile.

The maximum temperature rise for the stationary state as a function of beam profile is shown in fig. 11. It is lower for the cases with broader beam as expected due to the broad distribution of the energy deposition despite the weaker natural convection.

### 3.5. Adiabatic side walls

#### 3.5.1. Constant target height

Using a fixed target height of 150 cm, the effects of uncooled parts of the side wall have been studied by calculating systems of adiabatic wall height ($H_a$) of 50, 75 and 100 cm. The flow pattern for cases with an adiabatic part of the wall look very similar to the result with a totally conducting wall ($H_a = 0$ cm), showing a simple smooth circulation. However, the actual velocity distributions are slightly different: the average rising velocity is plotted as a function of height in fig. 12. With an adiabatic side wall the velocity is increased by about 10% in the region above the level of the adiabatic wall, but is only slightly increased elsewhere.

In the boundary layer near the side wall, there is, as may be expected, a steep temperature gradient only at the surface where the wall temperature is kept constant. For the case with the 100 cm adiabatic side wall, an island was seen in the upper core region. This is a low temperature island which appears and disappears periodically. It is caused by the enhancement of the flow and the poorer cooling of the target due to the smaller heat transfer area.

As for the time behaviour of the maximum tempera-

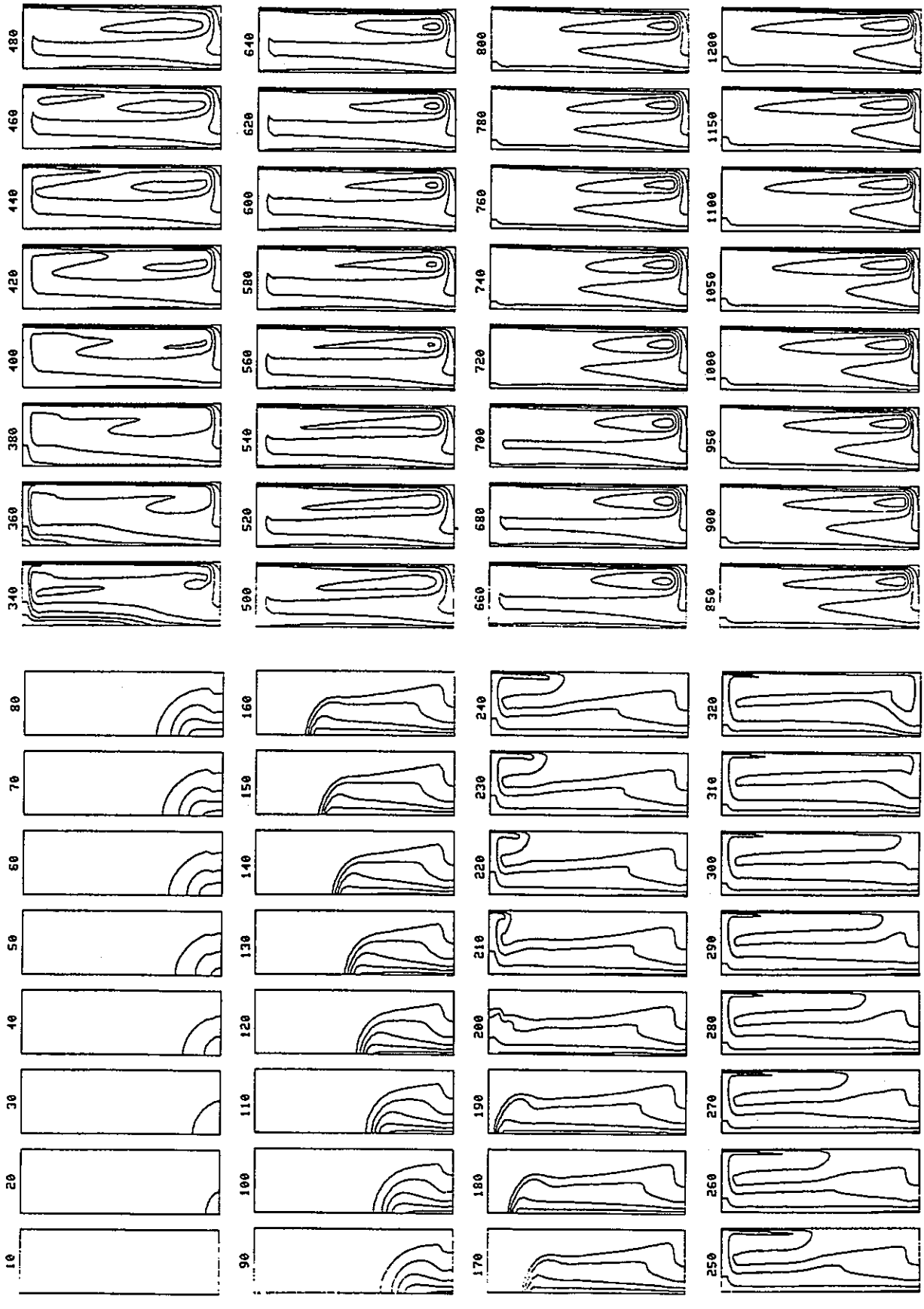


Fig. 9. Time change of the temperature distribution for 10 cm beam profile. The first drawing is at 1.3 s and the interval is 1.3 s. The last drawing is the converged distribution at 157.7 s. $dT = 0.05$ (6.25°C) up to 320 and 0.025 (3.13°C) for the rest.

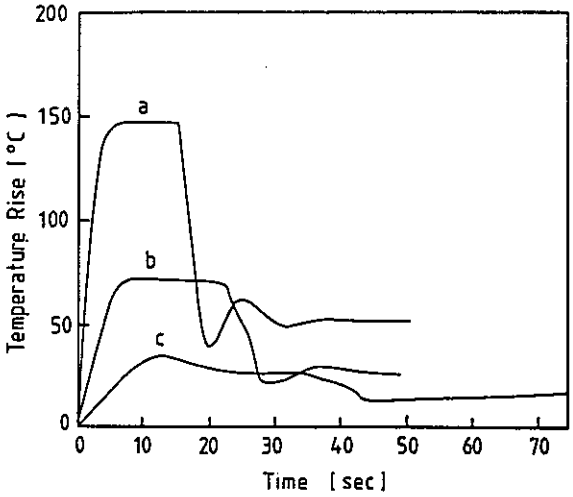


Fig. 10. Time behaviour of the maximum temperature for various beam profiles: (a) 2.5 cm, (b) 5 cm and (c) 10 cm.

ture, the initial transient is exactly the same for all three cases. This is due to the fact that the temperature of the central portion is not influenced by the conducting wall until the strong "total circulation" is established. Since the smaller area of heat transfer for the higher adiabatic walls results in a less effective cooling, the maximum temperature after the transient naturally becomes higher. For the case of the 100 cm wall it still increases with time.

*3.5.2. Constant height of adiabatic side wall*

Calculations were made for systems with a constant height adiabatic side wall (100 cm) and with five different target heights. The flow patterns are almost the same, showing "total circulation" for all cases. The temperature distributions become more complicated as the target height is reduced. This is due to the smaller heat transfer area, as discussed in sect. 3.5.1.

The time development of the maximum temperatures in the system are almost the same as for the cases of corresponding target height with a total conducting wall (cf. fig. 6). After the initial transient, the maximum temperatures are stabilized for all except the 150 cm case (as discussed in section 3.5.1).

The temperature for the stationary state is plotted in fig. 13 as a function of the target height for cases with

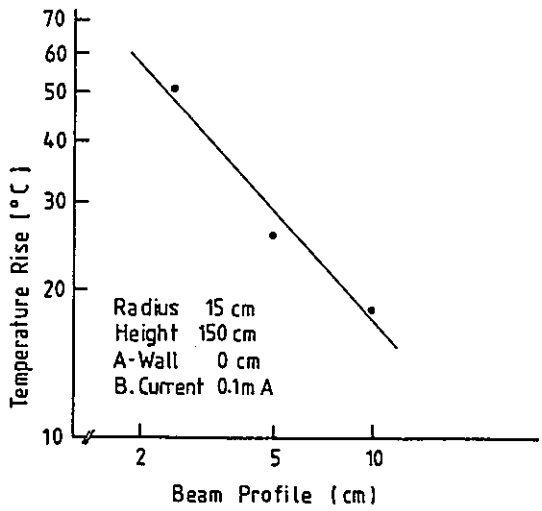


Fig. 11. Temperature rise in the stationary state vs beam profile.

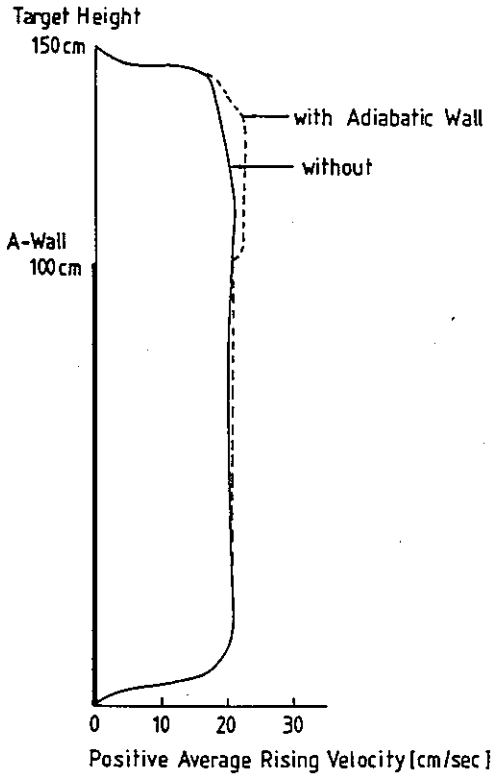


Fig. 12. Comparison of the average positive axial velocity as a function of height for the results with and without adiabatic wall at 51.0 s.

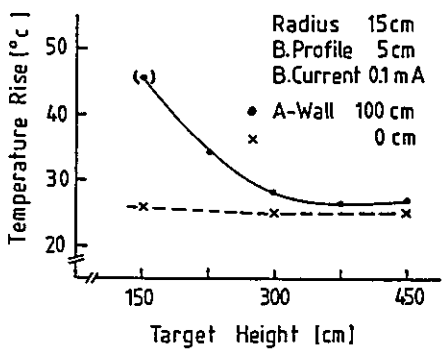


Fig. 13. Temperature rise in the stationary state vs target height with fixed height of adiabatic side wall of 100 cm. The values from the results with total-conducting wall are also plotted. As the value for the target height of 150 cm is not at a stationary state, it is plotted in brackets.

and without adiabatic side walls. For a target height larger than 300 cm, the difference between cases with and without adiabatic wall is only marginal.

## 4. Conclusions

In order to investigate the effect of target height, beam size, beam power and adiabatic side walls, a numerical survey has been mae for the natural convection in a liquid lead–bismuth target. The following conclusions can be drawn:

(1) During the establishment of natural convection, the flow and temperature distributions show a typical initial transient, during which the system reaches the maximum temperature in its history. The transient time depends linearly on the target height.

(2) In all cases studied, a simple total circulation of the liquid flow was obtained as stationary state.

(3) A power law relationship exists between the maximum temperature in the stationary state and the deposited energy. The exponent of this power law is 0.68 which agrees well with a one-dimensional model.

(4) A narrower beam leads to a stronger natural convection and to a simpler temperature distribution. However, the temperature of the stationary state will be higher. Some optimization study would be needed for the beam characteristics.

(5) An adiabatic side wall can be tolerated at the lower part of the target. A sufficiently large area should, however, be left for the heat transfer. To allow an adiabatic wall of 1 m length, the target height has to be around 3 m.

The author is grateful to Dr. W.E. Fischer, F. Atchison and Dr. C. Tschalär for their helpful discussions and encouragements.

## Appendix

*Nomenclature*

$H$ : target height.
$H_a$ : height of adiabatic wall.
$R$ : target radius.
$r$ : radial coordinate.
$t$ : time.
$T$ : temperature.
$V_r$ : radial velocity.
$V_z$ : axial velocity.
$z$ : axial coordinate.
$\gamma$ : aspect ratio ($= H/R$).
$\Omega$ : vorticity.
$\Psi$ : stream function.
$\Phi$ : internal heat generation.
Gr : Grashof number.
Pr : Prandtl number.

Physical variables (expressed with *) were normalized in the following way.

$$t = \alpha t^*/HR,\ r = r^*/R,\ z = z^*/H,$$

$$\Psi = \Psi^*/H,\ \Omega = HR\Omega^*/\alpha,\ T = (T^* - T_0)/T_0,$$

$$V_r = RV_r^*/\alpha,\ V_z = R^2 V_z^*/H\alpha,\ \Phi = HRq/(\alpha T_0 \rho C_p),$$

where $\alpha$ is the thermal diffusivity and $T_0$ the melting temperature, $\rho$ the density and $C_p$ the specific heat of LBE. Dimensionless numbers are defined as

$$\mathrm{Pr} = \nu/\alpha,\ \mathrm{Gr} = g\beta T_0 H^2 R/\nu^2,$$

where $\nu$ is the dynamic viscosity, $g$ the acceleration of gravity, and $\beta$ the thermal expansion coefficient of LBE respectively.

## References

[1] S. Ostrach, Proc. 7th Int. Heat Transfer Conf., München (1982) RK9.
[2] L. Buth and H. Werle, INR-996, Kernforschungzentrum, Karlsruhe (1980).
[3] K.E. Torrance, J. Fluid Mech. 36 (1969) 21 and 33.
[4] C. Tschalär, Proc. ICANS-V, Jülich.